

金屬氧化物薄膜與奈米微結構之多功能電漿
處理與光電應用

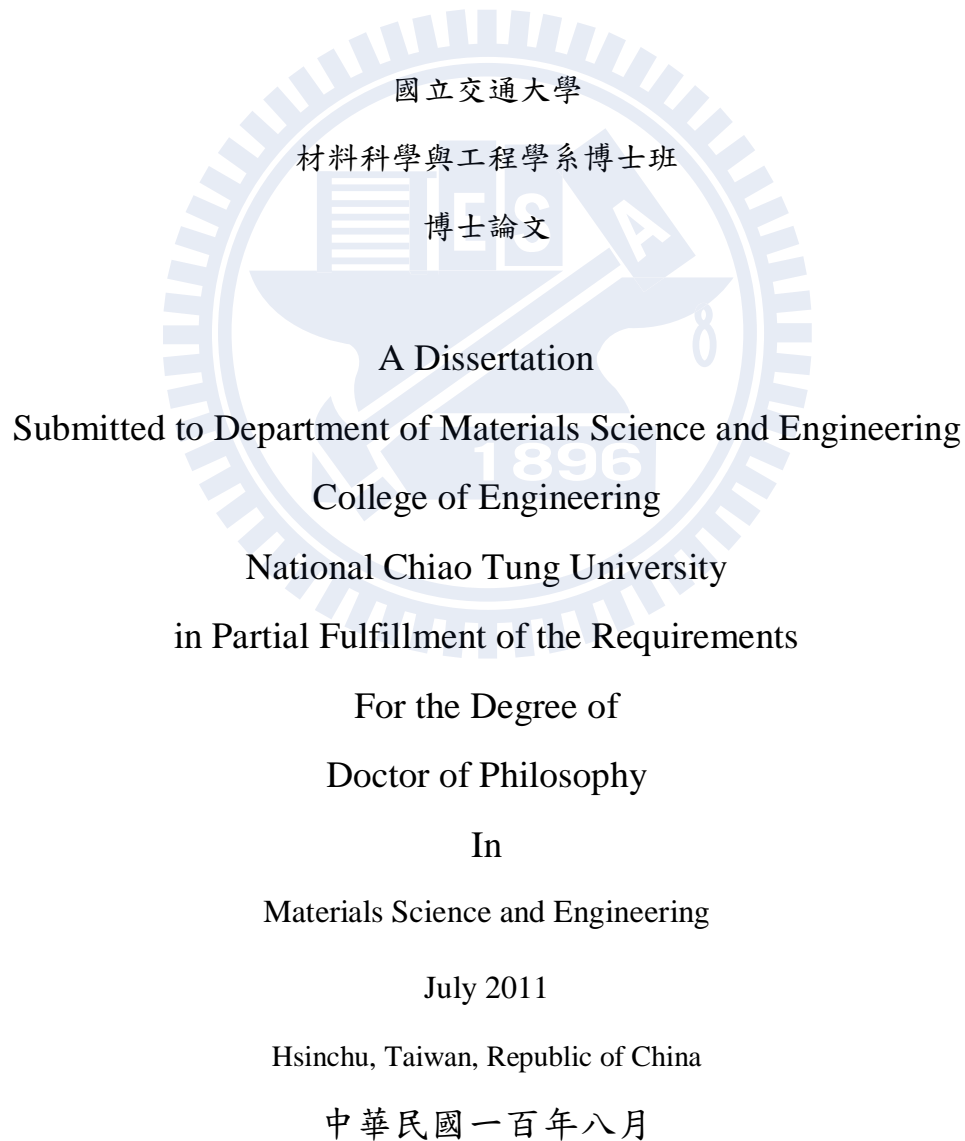
**Multifunctional Plasma Treatment on Metal Oxide Thin Films and
Nanostructures for Photovoltaic Device**

研究生：陳大方

Student: Naratip Chantararat

指導教授：陳三元

Advisor Professor: San-Yuan Chen



金屬氧化物薄膜與奈米微結構之多功能電漿 處理與光電應用

研究生：陳大方

指導教授：陳三元 教授

國立交通大學

材料科學與工程學系博士班

摘要

為了滿足全世界提升太陽能轉換效率的目標，對於發展與部署大規模、省錢、可重複利用的能源有相當的需求。近年來，在透明導電基板上，有機或是無機材料製成的太陽能電池，都具有良好的能量轉換效率。透明導電基板或是奈米微結構可讓光通過以被底下的活性材料層吸收，更可將電子從此光伏器裡傳導出。這些將是此論文探討的主題。

第一部份，噴霧沉積的方式用來探討載氣中氧成份對 FTO 薄膜造成的影響。此載體含有不同濃度的氧和氮 (0, 20, 50, 80 and 100%)，導致對薄膜厚度、晶格長成的大小和形狀有顯著不同。此種方式沉積而得的薄膜具有很低的電阻率約為 $10^{-4}\Omega\text{-cm}$ ，對 550nm 光波約有 76%-96% 的透光率。最後，此種光電效應製成的染料敏化太陽能電池以及高分子太陽能電池皆顯示特別的性質，例如電荷傳導，重組以及針對表面和介面效應而成的均化特性。

然而對於非晶質太陽能電池，作為透明基材的 FTO 薄膜，經氫化處理後會變質。因此，此研究係針對一種雙層結構的透明導電薄膜(AZO/FTO)，結果發現 AZO 的存在可保護

底下的 FTO 薄膜表面不受氫離子或是氫的自由基破壞，提供良好的磊晶介面。更進一步，在經過 400 度的再退火，藉由 Sn 和氧鍵結的再氧化，可復原已被氫離子破壞的 FTO 薄膜，此氫離子擴散和 Sn-O 氧化還原的過程皆，經由 XPS 和 SIMS 做詳盡分析。

第二部份主要著重在選擇性的電漿處理，針對表面的官能化，保護層的形成，以及蝕刻，來製備奈米柱、奈米線和奈米管。因此，我們製造 P 型 SnO₂ 的透明導電電極，是藉由氮氣電漿將 In 和 N 共同參雜到已參雜不同濃度 In 的 SnO₂ 薄膜。根據 In 參雜濃度，In 和 N 共同參雜的 SnO₂ 薄膜可製備成 p 型或是 n 型，其中氮原子藉由取代 SnO₂ 中氧的位置，可提升其導電性、霍爾遷移率、以及 In 參雜原子的溶解度。此特性也顯著的呈現在 pn 包覆核層的異質介面，顯示 IV 曲線的對稱性以及精準二極體特型。

同樣的方法也更進一步的用來比較室溫下經由氮氣電漿處理的 ZnO 的奈米線和奈米管。經過 900 秒處理，ZnO 的奈米管展現高穩定性的光學反應特性，優於奈米線約 20 倍，且結構維持完整。這代表奈米管其極高的表體比，對於表面修飾、藉由氮離子修補氧缺陷、及 ZnO 中的雜質，為指標性關鍵。

另一方面，我們提出一種選擇性的氧電漿蝕刻技術，藉由已合成的 ZnO 奈米柱為犧牲基材，再將 FTO 奈米粒子藉由簡單的噴霧熱解法沉積其在 ZnO 奈米柱表面，形成 ZnO-FTO 的異質結構奈米管。XPS 分析顯示氧電漿處理可降低 O^{2-/}OH⁻ 濃度比，而引起 Zn-O 鍵結的解離，以及 Zn 離子的向外擴散，形成內部中空的結構，其可由 FTO 表面羥基官能團的形成來解釋。藉由反覆 UV 光照射，隨時間變化的光電流測量，驗證此結構具有光感應性，且其暗電流三倍優於未經電漿處理的試片。

Multifunctional Plasma Treatment on Metal Oxide Thin Films and Nanostructures for Photovoltaic Devices

Student: Naratip Chantararat

Advisor: Professor San-Yuan Chen

Department of Materials Science and Engineering

National Chiao Tung University

Abstract

To satisfy the universal goal of improving solar-energy conversion efficiency, the need to develop and deploy large-scale, cost-effective, renewable energy is becoming increasingly important. In recent years, a solar cell consisting of organic or inorganic materials along with good transparent conducting oxide (TCO) films has achieved good power conversion efficiencies (PCE). Transparent conducting oxide (TCO) films or nanostructures serve as a window for light to pass through to the active material beneath and as an ohmic contact (electrode) for carrier transport out of photovoltaic. All detailed studies will become the focus in this thesis.

In the first part, a spray deposition process was used to investigate the effect of oxygen content in the carrier gas on FTO film morphology and properties. The carrier gas containing various O₂/N₂ concentrations (0, 20, 50, 80 and 100%) led to significant change in thickness, size and shape of grain growth. The deposited films reach a low resistivity of $\sim 10^{-4}\Omega\text{-cm}$ and a transmittance of 76%~96% at 550 nm. Finally, photovoltaic implement of dye-sensitized solar cells (DSSCs) and polymer-based solar cells reveals the particular behaviors such as charge

transport, recombination, and collection properties respected to the surface and interfacial effects.

However, in case of amorphous silicon solar cells (a-Si:H), it was found that a hydrogenated effect results in the deterioration of FTO film as TCO electrode. Therefore, a double-layered transparent conducting AZO/FTO thin film was investigated and the results suggest that the AZO film acts as a protecting layer for the beneath FTO film surface, providing an excellent epitaxial interface, from the direct bombardment of H ions and radicals. Moreover, following by a post-annealing treatment at 400°C, the degraded properties of FTO can be recovered via the reoxidization of Sn-O bounds, in which H-ions diffusion and Sn-O redox process was interpreted by XPS and SIMS analysis.

In the second part, the investigation is mainly focused on a selective plasma-treatment technique for introducing surface functionalization, passivation, and etching to form nanorods (NRs), nanowires (NWs) and nanotubes (NTs). Herein, we fabricate the p-type SnO₂-based transparent conducting electrode which was constructed by a novel approach of In and N co-doping by nitrogen plasma (5-40 min), to In-doped SnO₂ films with several In contents (0, 3, 7, 15 and 30%). Depending on In doping concentration, (N, In)-codoped SnO₂ can be modified to either p-type or n-type where N atoms primarily substitute in O sites in SnO₂ with enhanced conductivity, Hall mobility and solubility of the In dopant. Significantly, such behavior is also exhibited in term of pn core-shell heterojunction, showing the symmetrical I-V curve with rectified diode characteristics.

Furthermore, similar method was applied to investigate the key aspects in comparison between ZnO NWs and NTs under nitrogen plasma treatment at room temperature condition. Upon an extended treatment of 900 s, the ZnO NTs exhibit higher reliability of photoresponse,

20 times of NWs without deteriorated structure. This indicates that higher surface-to-volume ratio of NTs is critically important factor for inducing the surface modification, occupying the oxygen defects and impurities in the ZnO matrix by the presence of N ions.

On the other hand, we proposed a selective oxygen-plasma-etching technique for the formation of ZnO-FTO heterostructure nanotubes using presynthesized ZnO nanorods (NRs) as sacrificial templates, and FTO nanoparticles are deposited onto the ZnO nanorods by a simple spray pyrolysis method. XPS analysis demonstrated that the oxygen-plasma treatment decreased the O^{2-}/OH^- concentration ratio, resulting in dissociation of the Zn-O bonds and the outward diffusion of Zn cations to form an interior hollow, which is related to the formation of the hydroxyl functional group, Sn-OH, at the FTO surface. Time-dependent photocurrent (I-T) measurements under ON-OFF cycles of UV illumination confirms a rectified photoresponse characteristic and a dark current increased by about 3 orders of magnitude over that of the unetched sample.

Keywords: metal-oxide materials, plasma treatment, transparent conducting oxide

Acknowledgements

First and foremost I would like to express my deep and sincere gratitude to my supervisor Professor San-Yuan Chen. I appreciate all your contribution of time, ideas, and funding to my PhD experience productive and stimulating. You have taught me, both consciously and unconsciously, how a good scientist should act. Your joy and enthusiasm for research, conscientious attitude towards work, creativity and good organization was contagious for me. Importantly, you are also quite open-minded which gave me enough freedom to design my research orientation.

Another “Big Thank You” will go to Dr. Chin-Ching Lin, my co-advisor. Despite your busy schedule, you managed to have meetings with me regularly throughout my PhD. You have always been very encouraging to come up with some brilliant ideas when I was in the bottleneck of the projects. There are so many things I could learn from you as a successful scientist.

I am deeply grateful to Dr. Dean-Mo Liu, who gave me many suggestions, detail supervision and encouragement, especially during our group meeting. I have learnt so much from the way of your concepts, and there are so much effort that you put on to transform me into an independent researcher. I would honestly say that you are a person who every student can dream of. I truly appreciate that.

Beside my advisors, my research would not be completed without supporting staffs, Mei-Ching, Yu-wei, Po-Hsueh and other co-workers from NCTU and ITRI. I am free from the hustle of exhaustive experiments and technical works. Thank you for all kindness for sharing me Taiwanese’s culture and life. Although my poor Chinese becomes a huge barrier to communicate

fluently, I felt that everyone was so patient to talk and listen to me; I cannot thank you enough for that.

Dear all Thai friends, you all are like my brother and sister. We could always enjoy life (exercises, drinks, foods, etc.) together, because we know this is what life is about! Thank you for a lot of accompanies and I wish you all the best for life, studies and future careers. Although time passed too quickly, TSAX (Thai student association in Xin-Chu) must go on to facilitate all the members, especially new comers and confederates.

Dear mom, dad and elder brother, no words can express my gratitude to you for giving me life, educating me, and your conditional love. All I have achieved today would not be possible without the love from all of you. As an old Chinese saying “with elderly parents at home, filial son must not travel far”, I really appreciate your understanding and support when I studied abroad to pursue my interests.

Last but not least, this thesis is dedicated to my other-half, Shu Han. You have walked into my life six years ago, fulfilling my life with joy, satisfaction and happiness. We have been through every good and bad moment hand-in-hand. We have grown up strongly while seeking a better future together. Thank you for staying beside me (always) as best friend, critic and my lover.

Naratip Chantararat

Hsinchu, Taiwan

July, 2011

Contents

Chinese abstract	i
English abstract.....	iii
Acknowledgement	vi
Contents.....	viii
Figure captions.....	xi
Table and scheme captions	xvi

Chapter 1

Introduction.....	1
-------------------	---

Chapter 2

Literature Review and Theoretical Framework	5
---	---

2.1 Wide band-gap metal-oxide materials	5
2.1.1 Background of metal oxide nanostructures: ZnO and SnO ₂	5
2.2 The State-of-Art of Defect Chemistry in Metal Oxide Materials	7
2.2.1 Electronic and optical properties	7
2.2.2 Band-gap Engineering.....	11
2.3 Surface modification in nanoscience and nanotechnology.....	15
2.3.1 Surface passivation	15
2.3.2 Surface treatment by plasma	18
2.3.3 Surface etching by plasma.....	24
2.4 Solar cells-based Transparent Conducting Oxide (TCO) semiconductors	28
2.4.1 Perspectives and evolutions of solar cells	28
2.4.2 Hydrogenated amorphous silicon (a-Si-H) solar cells	28
2.4.3 Dye-sensitized solar cells (DSSCs)	30

Chapter 3

Experiment methods	37
--------------------------	----

3.1 Experiment overviews	37
3.2 Preparation of metal-oxide materials.....	38
3.2.1 Fabrication of F-doped SnO ₂ (FTO) and co-doped p-type (N, In):SnO ₂	38

3.2.2	Fabrication of Al-doped ZnO (AZO) film on FTO	39
3.2.3	Synthesis of ZnO nanorods (NRs), nanowire (NWs) and nanotubes (NTs)	39
3.2.4	Preparation of O ₂ plasma-etched ZnO/FTO heterostructure nanotubes	40
3.2.5	Preparation of n-type ZnO/p-type (N, In):SnO ₂ core/shell heterojunction diode..	40
3.3	Characteristics analysis	41
Chapter 4		
Effect of Oxygen Partial Pressure on the Microstructural Growth and Physical Properties of Transparent Conducting Fluorine-Doped Tin Oxide Thin Films Fabricated by Spray Pyrolysis Method.....		
43		
4.1	Introduction	43
4.2	Formation and microstructure of FTO texture films	44
4.3	Optical and electrical properties	49
4.4	Performance of photovoltaic devices.....	52
4.5	Summary	57
Chapter 5		
Mechanism of a AZO-coated FTO Film in Improving the Hydrogen Plasma Durability of Transparent Conducting Oxide Thin Film for Amorphous-Silicon Based Tandem Solar Cells		
58		
5.1	Introduction	58
5.2	Surface morphology and structural properties of single-layered FTO films and double-layered AZO/FTO films	60
5.3	Evolution of transparent conducting films under H-plasma treatment.....	63
5.4	Diffusion mechanism of hydrogen-incorporated atoms	69
5.5	Summary	75
Chapter 6		
Nitrogen Plasma-Assisted Co-doped P-type (In, N):SnO₂ Ultra-Fine Thin Films and N-ZnO/p-SnO₂ Core-Shell Heterojunction Diodes Fabricated by an Ultrasonic Spray Pyrolysis Method.....		
77		
6.1	Introduction	77
6.2	Fabrication and physical properties of In-doped SnO ₂ films	80
6.3	Effect of partial substitution of nitrogen on In-doped SnO ₂ film surface.....	83

6.4	N-ZnO/p-SnO ₂ Core-Shell Heterojunction Diodes	90
6.5	Summary	94
Chapter 7		
Enhanced UV Photoresponse in Nitrogen Plasma ZnO Nanotubes.....		95
7.1	Introduction	95
7.2	Chemical growth of ZnO nanorods (NRs) and nanowires (NWs)	96
7.3	Effect of N-plasma treatment on ZnO nanostructures	97
7.4	Photoresponse characteristics	100
7.5	Summary	102
Chapter 8		
Selective Oxygen-Plasma-Etching Technique for the Formation of ZnO-FTO		
Heterostructure Nanotubes and Their Rectified Photocatalytic Properties		104
8.1	Introduction	104
8.2	Microstructure of FTO-coated ZnO nanorod arrays.....	107
8.3	Oxygen-plasma-etching mechanism on ZnO nanorod templates.....	107
8.4	Photoresponse of ZnO-FTO composite nanotubes.....	117
8.5	Summary	119
Chapter 9		
Conclusion		120
9.1	Investigation of TCO thin film electrode for photovoltaic devices.....	120
9.2	Plasma treated metal oxide thin films and nanostructures.....	121
References.....		123
Cirriculum Vitae		134
Publication list.....		135

Figure captions

Figure 2.1	Structures of (a) wurtzite ZnO and (b) cassiterite SnO ₂ [26, 27].	6
Figure 2.2	Schematic diagrams of charge transport in the energy transitions from the valence band to the conduction band [35].	10
Figure 2.3	Illustration of band alignment and the Schottky barrier formed at the junction of conducting oxide (ITO) and semiconductor (TiO ₂) (a) before and (b) after H ₂ -gas reduction [49].	12
Figure 2.4	(a) Structure and (b) equilibrium energy band diagram of the CuYO ₂ :Ca/ZnO/ITO p-i-n heterojunction diode coated on glass substrate [52].	14
Figure 2.5	I _{DS} -V _{DS} curves (at different gate biases: 6, 8 and 10 V) and I _{DS} -V _G curves (at V _{DS} =0.1 V) of a ZnO nanowire FET under ambient air, dry O ₂ , and vacuum conditions as compared between (a, c) before and (b, d) after PMMA passivation, respectively [56].	16
Figure 2.6	SEM images of SnO ₂ -ZnO core-shell where the SnO ₂ nanofiber was synthesized by electrospinning and the ZnO outer layer was deposited with different ALD cycles of (a) 0, (b) 100, and (c) 400 [10].	17
Figure 2.7	(a) TEM image of a ZnO-SnO ₂ core-shell nanorod where the inset shows a magnified image of the crystal fringes in the SnO ₂ shell. (b) High-magnification TEM image reveals misfit dislocation in the SnO ₂ epitaxial layer. (c) Schematic model of the atomic arrangements of the SnO ₂ hexagonal nanoring on the (100) plane surrounding a ZnO nanorod on the (0001) plane [62].	18
Figure 2.8	Schematic drawing of ZnO nanowire shows (a) the influence of physisorbed water molecules in air, capturing free electron and inducing a low-conductivity depletion layer at the nanowire surface. The current is increased under a vacuum condition due to a desorption of the water molecules. (b) Upon illumination with UV in air, electron-hole pairs are generated, while the carriers are decreased with the replacement of the hydroxyl group by oxygen ions from the steady light [57].	20
Figure 2.9	XPS spectra of O 1s core level from untreated and oxygen plasma treated (5-30 min) ZnO films [74].	20
Figure 2.10	(a) Idealized energy band diagram for an Au/SnO ₂ interface. Band alignment of Au contact on (b) an as-deposited SnO ₂ film and (c) an oxygen-plasma treated SnO ₂ film. (d)	

Structures of the SnO ₂ films exposed under different oxygen plasma-treated time (30 and 180 s) [76].....	22
Figure 2.11 Illustration of the colloidal lithographic concept with some 2D geometrical structural units: (a) hexagonal double layer, (b) hexagonal triple layer (HCP), (c) hexagonal triple layer (FCC), (d) square double layer, and (e) square triple layer [91].....	25
Figure 2.12 SEM images of the resultant embossed TiO ₂ films coated on polystyrene bead templates (a) without O ₂ plasma etching, and O ₂ plasma etching for (b) 2 min and (c) 4 min. (d) Cross-sectional TEM image of a hollow TiO ₂ hemisphere with TiO ₂ film deposition at intervals as shown in the inset. (e) High-magnification TEM image from the TiO ₂ shell showing polycrystalline layer with thickness (~150 nm) and grain sizes (10-30 nm) [60].	26
Figure 2.13 Flowchart for ordered silica nanotube arrays, fabricated by using vertical silicon nanowire templates [59].	27
Figure 2.14 Schematic representation of the principle of the dye-sensitized photovoltaic cell operating under illumination [97].	31
Figure 2.15 Schematic drawing of the DSSC. An array of Zn microtips, grown vertically from conductive glass electrode and decorated with ZnO nanotip hierarchy, serves as the photoanode [101].	34
Figure 2.16 Interfacial electron transfer via dye, TiO ₂ particle, and TCO electrode, involving a trapping/detrapping process [104].	35
Figure 2.17 Directing the flow of photogenerated electrons across the nanostructured semiconductor ZnO NW/ZnO NP composite and the possible electron transport mechanism regarding to the annealing treatment process [105].	36
Figure 4.1 (a-e) AFM topographic 5×5μm scans and (f-j) cross-sectional TEM images for oxygen-incorporated FTO films deposited at various oxygen concentrations: 0, 20, 50, 80 and 100%.....	46
Figure 4.2 FE-SEM images of the deposited FTO films on glass substrate as a function of oxygen content: (a) 0%, (b) 20% and (c) 100%.	47
Figure 4.3 X-ray diffraction (XRD) patterns of FTO films deposited on glass substrate with O-incorporated various concentrations.	49
Figure 4.4 Transmission (T%) spectra of FTO films of varying oxygen concentration, deposited on Corning glass.....	50

Figure 4.5	FTO film electronic-transport properties: carrier concentration (n), resistivity (ρ), and Hall mobility (μ) as a function of the oxygen concentration (0-100%)..	51
Figure 4.6	J-V characteristics of FTO film-based DSSCs. The illumination intensity of 100 mW cm ⁻² with AM 1.5 and active area of 0.25 cm ² were applied..	53
Figure 4.7	Representative Nyquist plot of the electrical impedance spectra of the FTO films measured in the frequency range of 0.1Hz – 1MHz under AM 1.5.....	54
Figure 4.8	Trace of current density against voltage (J-V) for three cells with 0%, 20% and 100% O ₂ /N ₂ concentrations..	56
Figure 5.1	Plain-view SEM images of the textured FTO films and the AZO/FTO films (a and d) without H ₂ plasma treatment, or with H ₂ plasma treatment for (b and e) 5 min , and (c and f) 30 min.....	61
Figure 5.2	X-ray diffraction pattern of the FTO, AZO, and AZO/FTO samples before and after H ₂ plasma treatment for 30 min as identified at each spectrum..	62
Figure 5.3	(a) Cross-sectional TEM image of a double AZO/FTO film coated by a thin Pt conductive layer. (b) High-magnification TEM image taken from the region, marked by a square in (a)..	63
Figure 5.4	Dependence of (a) carrier concentration, (b) Hall mobility, and (c) sheet resistance on H ₂ plasma treated time for the deposited FTO, AZO, and AZO/FTO films..	64
Figure 5.5	The effect of (a and b) H ₂ plasma treatment at 0, 5, 10, 20 and 30 min, and (c and d) post annealing treatment at 400°C on the optical transmission for the FTO and AZO/FTO films.....	67
Figure 5.6	SIMS depth profiles of (a and b) FTO and (c and d) AZO/FTO films for secondary ion count of Sn, F, O, and H normalized relative to FTO. The plasma-treated samples and the post-annealed samples are represented by S2 and S3, respectively.....	70
Figure 5.7	X-ray photoelectron spectra of the F 1s peak observed for (a) FTO and (b) AZO/FTO samples with as-deposited condition (S1), 30-min plasma treatment (S2), and post annealing process, subsequently. The deconvoluted peaks F1 and F2 indicate a major component (Sn-F bond) and a minor component (C-F bond), respectively.....	72

Figure 5.8	The variation of [Sn]/[O] atomic intensity ratios for the FTO and AZO/FTO films corresponding to the surface of as-deposited films (S1), the surface of H-plasma exposed films (S2), and the surface of subsequently annealed films (S3). The insets show the relative Sn (3d _{3/2}) and Sn (3d _{5/2}) core level spectra..	74
Figure 6.1	XRD peaks of In-doped SnO ₂ films prepared by ultrasonic spray pyrolysis method with In concentrations: 0, 3, 7, 15 and 30 at%..	81
Figure 6.2	UV-vis absorption spectra of the In-doped SnO ₂ film deposited on corning glass substrate with various doping concentrations. The optical transmission demonstrates the spectral continuity in range of 300-700 nm.....	82
Figure 6.3	The In doping concentrations (0, 3, 7, 15 and 30 at%) during the film fabrication are shown in (a), (b), (c), (d) and (e), respectively, and the annealing temperature is constant at 600°C. Comparing dark current of as-deposited and annealed SnO ₂ films undergoing the post plasma treatment (0-40 min).....	84
Figure 6.4	(a) XPS spectra of the N 1s peak observed for (N,In) co-doped SnO ₂ samples treated in N plasma for 0, 10 and 40 min. (b) AES depth profiles of the sample in (a) at 40 min, and the etching rate of Ar ⁺ for 1 sec is equal to 3 Å in penetration depth.....	89
Figure 6.5	(a) Top view and (b) cross section SEM images of In:SnO ₂ -coated ZnO nanorod arrays. The inset shows a high magnification of top view image. (c) TEM images illustrate a pn heterojunction core-shell consisted of p-layer In:SnO ₂ and n-layer ZnO with their lattice images and FFT patterns as identified by yellow.....	91
Figure 6.6	(a) I-V characteristics of the pn heterojunction diode in dark using an applied voltage in range of +/-1eV . The inset gives the I-V characteristics of individual p-type In:SnO ₂ and n-type ZnO films. (b) The energy band diagram at equilibrium.....	93
Figure 7.1	FESEM images: of (a) ZnO NWs and (b) NTs; HRTEM images (c) NWs and (d) NTs on glass substrates subjected to post annealing at 300°C and nitrogen plasma treatment.....	97
Figure 7.2	Photoluminescence spectra measured at room temperature for a nitrogen plasma treatment of 0, 60 and 720 s for (a) ZnO NWs and (b) NTs.....	98
Figure 7.3	(a) Current as a function of applied voltage for both ZnO NWs and NTs, with and without a 900 s nitrogen treatment. (b) Dark current dependence versus N ₂ -exposure time.....	99

Figure 7.4 (a) Time traces of the current with the chopped light for samples measured after a 900 s N₂ plasma exposure under an applied voltage of +1 eV (electron conduction). The inset shows the schematic diagram of the corresponding measurement method. (b) Energy-band diagram for 300 °C annealed and N₂ plasma-treated ZnO under UV illumination.. 101

Figure 8.1 Field-emission SEM images of (a) as-deposited ZnO NRs grown on a Corning glass substrate using a hydrothermal method and (b) FTO coating on ZnO NRs obtained by spray pyrolysis deposition. The FTO deposition time was 2 min at 380°C.. 107

Figure 8.2 HRTEM images of core-shell ZnO-FTO heterostructures (a) before and (b) after exposure to oxygen plasma for 20 min at room temperature. The insets of parts a and b show the magnified interface, indicated by the red rectangle.. 108

Figure 8.3 Cross-sectional HRTEM and EDS line scans of an ZnO-FTO nanotube fabricated by dry oxygen-plasma etching at 20 min: (a and b) side view; (c and d) top view.. 109

Figure 8.4 Formation of voids in the FTO-coated ZnO obtained before and after etching of ZnO NRs as a function of time: (a) 0min; (b) 2min; (c) 20min. The inset of part b is a high-resolution image of the void.. 110

Figure 8.5 XRD patterns of as-grown ZnO and ZnO-FTO heterostructures on glass treated for the times noted under oxygen plasma. The patterns are vertically offset for clarity.. 111

Figure 8.6 PL of (a) as-grown ZnO and (b) FTO-coated ZnO samples showing variation of the spectrum intensity corresponding with the plasma exposure time. The insets of parts a and b demonstrate the morphology of the ZnO NRs after 20 min of etching and the relative intensity (R) of part b, respectively.. 112

Figure 8.7 XPS spectra of the O 1s peak in FTO-coating ZnO samples: (a and b) before and (c and d) after plasma etching (350-W RF power for 20 min), preparing the samples with and without preheat annealing at 500°C, as indicated in each figure.. 114

Figure 8.8 Under UV illumination ($\lambda=365\text{nm}$), with an applied voltage of +5 eV (electron conduction), τ_{g1} and τ_{g2} are shown indicating the response times of time-dependent photocurrent with (20 min) and without oxygen-plasma treatment, respectively..... 118

Table and scheme captions

Table 2.1	Formation energy (eV) of N-doped SnO ₂ atom supercells in O-rich condition and Sn-rich condition [38]..	9
Table 4.1	Summary of FTO film properties used in DSSCs.	53
Table 4.2	Summary of photoelectric conversion efficiencies for a selection of polymer solar cells..	57
Table 6.1	The results of Hall effect measurements of the annealed In:SnO ₂ samples corresponding to 0-30% In doping concentration with a selective N-plasma treatment at 40 min..	87
Scheme 4.1	Schematic cross section of polymer solar cells deposited on an FTO-coated glass substrate, using an oblique electron-beam evaporation method..	55
Scheme 5.1	Illustration showing the cross-sectional structure of FTO and AZO/FTO films and the possible H-ion diffusion mechanism under different conditions.	75
Scheme 6.1	Illustration of the corresponding current-voltage (I-V) measurement set-up. The deposition and post plasma process applied to fabricate the p-In:SnO ₂ /n-ZnO core-shell heterojunction using ZnO nanorods as a template.	92
Scheme 8.1	Top-View Cross-Sectional Schematic Diagram of an FTO-Coated ZnO Core-Shell Nanostructure, Illustrating the Oxygen-Plasma Enhanced Etching Evolution of the ZnO-FTO Nanotube ^a (^a The direction of outward diffusion is indicated by the arrow in stage 3).	117

Chapter 1

Introduction

During the past decade, it is increasingly clear that the global reliance on exhaustible natural resources (e.g. oil, ethanol, natural gas and coal) must shift in favor of using sustainable strategies and renewable energy sources in order to provide more environmentally production route. One renewable resource that has the capability to meet the increasing energy demand comes in the form of solar radiation. The direct conversion of solar energy to electricity attributed to photovoltaic effect has a significant impact allowing clean, unlimited-source, reliable, and cost-efficient methods. However, one of major components in photovoltaic cells relies on semiconductor materials that involve the use of sophisticated technologies with high production cost. Thus, significant cost reductions using novel strategies must be considerably necessary to compete with other traditionally generated power.

Transparent conducting oxides (TCOs) that provide thermal stability, high transparency, and oxidation resistance have yet to be widely used in electronic, optoelectronic and photovoltaic applications [1-4]. The components of TCOs are mainly composed of the wide band gap metal oxides with unintentional n-type conductivity generated by intrinsic defects and the inadvertent incorporation of other impurities. For example, the role of oxygen vacancies (V_o) is predominant for the electronic properties. Consequently, the large oxidizing power of charge transport in metal oxide coupled with low-cost production renders it the semiconductor materials of choice for many applications that exploit solar energy conversion efficiency.

Among the metal oxide materials, there are a large number of options for improving solar cell performance by the use of nanomaterials as building blocks for devices. This can help downscale conventional technologies by developing a miniaturization of functional units with its unique physical and chemical properties. In particular, low-dimensional, nanostructured materials have attracted much attention because of their large surface-volume characteristics, which promote some advantages such as superior sensitivity to light, electrical transport, and lower charge carrier recombination. Moreover, the effect of defects on the physical properties can significantly increase with decreasing in dimension of material. In this thesis, of particular interest is also the use of plasma technology to deliver high throughput, conformal coverage, and reproducibility of gaseous treatment at low substrate temperature, for high surface reactive nanostructures. Especially, a high aspect ratio of 1D nanostructures such as nanorod [5, 6], nanowire [7, 8], core-shell nanowire [9, 10], nanotube [11, 12], etc. could be more effective with plasma than other alternative nanostructures or textured films when quantum confinement, charge-carrier collection and transport are determined by low trapping/detrapping.

For the purpose to develop new technique for the metal oxide surface modification, particularly using in solar cell applications, Chapter 4 firstly demonstrated the fundamental investigation of the effect of oxygen content on FTO film morphology and properties. The various ratios of O₂/N₂ carrier gas led to significant change in thickness, size and shape of grain growth of FTO films, which is indicative of variable conditions to study the role of correlation between optical and electrical properties. As the result, high film quality was obtained at a low resistivity of $\sim 10^{-4} \Omega\text{-cm}$ and a transmittance of 65%~92% ($\lambda=550$ nm). Moreover, photovoltaic implement of dye-sensitized solar cells (DSSCs) also revealed the particular behaviors such as conversion efficiency, charge transport, recombination, and collection properties. With this

investigation, the model will examine the concept in understanding the mechanism of ion-incorporated film and the defect state behavior, which is fundamentally important to the rest of following studies.

In Chapter 5, we proposed the development of double-layer TCO electrode that involves an additional AZO barrier layer coating on the FTO layer. The deterioration of FTO film properties might be reduced when the products were exposed to hydrogen plasma atmosphere during the fabrication process of hydrogenated amorphous silicon (a-Si:H) solar cells. This configuration was confirmed by the structural (SEM, TEM, XRD, XPS and SIMS), optical (UV-Vis), and electrical (Hall measurement) characterizations that the AZO layer is able to protect the FTO film from the bombardment of H-ions and radicals. Finally, a systematic study of the post annealing treatment reveals a recovery of the deteriorated properties of FTO films through the diffusion mechanism of incorporated hydrogen in the films.

Chapter 6 demonstrates a novel methodology for developing co-doped p-type SnO₂ films using dual acceptors (In and N elements). The deposited films were delivered by ultrasonic spray pyrolysis containing mixed solution of In and Sn precursors in combination with thermal annealing at 600°C and post nitrogen-plasma treatment. In this chapter, not only the film characteristics with different conditions will be presented, but also this technique can be adapted to use in 1D-nanoscale, e.g., core-shell nanowire. Because the ultrafine p-SnO₂ thin film with controllable size (~10 nm in thickness) and texture suites with such selective plasma treatment method (reactive ion etching; RIE), this nano-heterojunction seems to behave the same way as a conventional thin film diode. Therefore, we produced n-ZnO/p-SnO₂ core-shell diode using ZnO

nanorods as a template, which represents another technological challenge for a variety of applications in nanoscience.

Similar to Chapter 6, the investigation in Chapter 7 is involved with the influence of nitrogen plasma on chemically grown ZnO nanowire (NWs) and nanotubes (NTs). This section discusses, for the first time, the photoluminescence (PL), dark current (I-V measurement), and photoresponse (I-T measurement) behavior due to a change of the surface defect; indicating that the oxygen defects and impurities are occupied by the presence of N ions in the ZnO matrix.

Finally, Chapter 8 demonstrates the use of a selective oxygen-plasma etching technique to fabricate ZnO-FTO composite nanotubes. In this approach, presynthesized ZnO nanorod arrays act as templates, and FTO nanoparticles are deposited onto the ZnO nanorods by a simple spray pyrolysis method. Upon high power of oxygen plasma treatment, various ions and radicals (O^+ , O^{2+} , and O^*) generated by the oxygen plasma, readily diffuse into oxygen vacancies and create negative charges on the ZnO NR surface. Then, with prolonging the treatment time, the accelerated etching rate might occur to produce a large number of voids in the ZnO surface and form a hollow ZnO-FTO heterostructure, respectively. In addition, an etching mechanism via oxygen plasma will be tentatively discussed along with examining a rectified photoresponse and dark current characteristics compared with the as-synthesized sample.

Chapter 2

Literature Review and Theoretical Framework

2.1 Wide band-gap metal-oxide materials

During the past decades, metal oxide semiconductors have attracted much research attentions in a wide range of advanced applications such as electronics, optoelectronics, sensors, photocatalysts, field emissions, solar cells, etc. [13-17]. It is known as one of the material compounds containing transition elements and oxygen. So, for example, the oxide materials can provide various utilizations from additional doping incorporation due to its variable bandgaps across the infrared to ultraviolet regions. Moreover, the excellent chemical and thermal stabilities have commonly been observed based on the recognition that metal-oxide bound exhibits durable from dissolution in acidic and basic solutions and very high decomposed temperatures (more than 1000°C), respectively.

2.1.1 Background of metal oxide nanostructures: ZnO and SnO₂

Among the metal oxide proposed as wide band gap materials, Zinc oxide (ZnO) is one of the most extensively studied, owing to unique multiple properties such as high electron mobility, piezoelectric, pyroelectric, and strong room-temperature luminescence. Crystalline ZnO has a wurtzite type of crystal structure under ambient conditions. The wurtzite structure has a hexagonal unit cell with two lattice parameters (a and c), in which either Zn or O atom displaces with respect to each other along the threefold c -axis. Figure 2.1a shows tetrahedrally coordinated Zn²⁺ and O²⁻ ions with alternating planes stacked layer by layer along the c -axis direction. The

bonds between cation (Zn) and anion (O) possess a strong ionic interaction that the opposite charges result in a spontaneous polarization and piezoelectricity with normal dipole moment. For an electrostatic point of view, this polarity is an important factor in crystal growth, defect generation, plasticity, etching, etc. In addition to polar surfaces, it also introduces the four most common faces of wurzite ZnO including the polar Zn-terminated (0001), O-terminated (000 $\bar{1}$) faces (c-axis) and the nonpolar (2 $\bar{1}\bar{1}$ 0) and (01 $\bar{1}$ 0) faces [18]. Therefore, various shapes of the ZnO crystal are originated due to the configurations; differences in the growth rates of different crystal planes, which can also be facilitated for the fabrication of novel nanostructures. Due to its diverse and rich structures and properties with low-cost strategies, recently, many types of nanostructured ZnO including nanowires [19], nanoneedles [20, 21], and tubular whiskers [22] have already been synthesized mainly by hydrothermal growth, atmospheric spray pyrolysis, and vapor-liquid-solid (VLS) depositions [23-25].

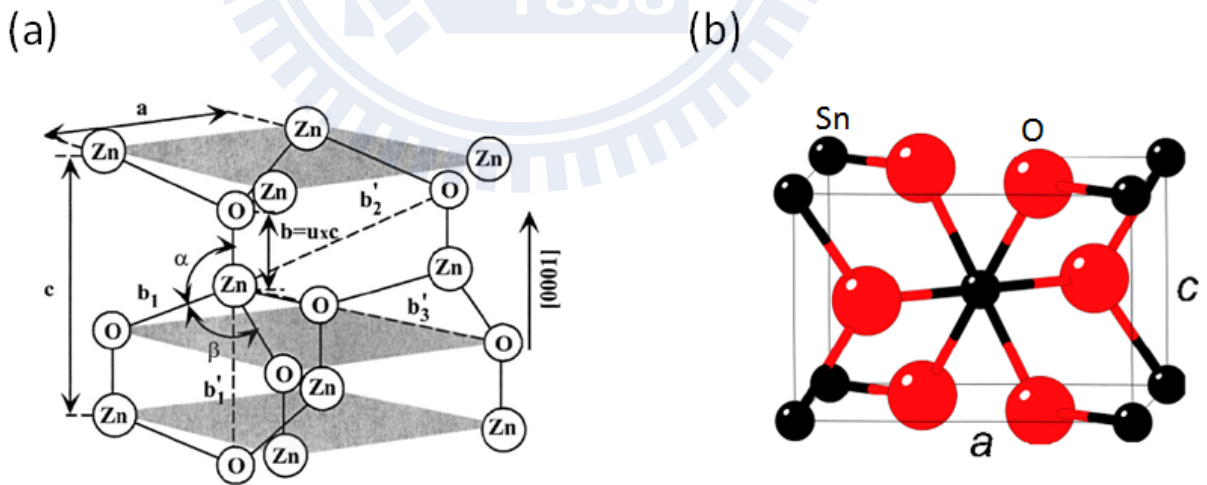


Figure 2.1 Structures of (a) wurzite ZnO and (b) cassiterite SnO_2 [26, 27].

Tin oxide (SnO_2) is another important n-type semiconductor regarded as an oxygen-deficient material. Its large bandgap ($E_g = 3.6 \text{ eV}$ at 300 K) makes it ideally working as a transparent conducting electrode for a wide range of industrial applications [28-31]. Structurally, SnO_2 can be formed by two natural oxidation states, Sn(II) and Sn(IV). The dominant crystal structure of the products is commonly described as cassiterite or rutile-structured SnO_2 , which is composed of the tetragonal unit. In a tetragonal unit cell, three-fold coordinated oxygen atoms surround the octahedral coordinated tin atoms as shown in Figure 2.1b. To activate the surface stability of such cassiterite structure, some energy (temperature in the range of 350-600°C) is required to keep balance between the number of the dangling cation bonds and the dangling anion bonds. Furthermore, the unique properties were arisen when nanosized dimensions occur in crystal structure through fabrication processes. The synthesis and growth of a certain morphology can be selectively controlled by the assembly of the building blocks [32-34]. Therefore, by exploiting the special electrical and optical properties of nanomaterials, there is a great potential as well as fundamental prerequisite for the development of nanoscience and nanotechnology, which will be a major discussion in the following sections.

2.2 The State-of-Art of Defect Chemistry in Metal Oxide Materials

2.2.1 Electronic and optical properties

The structural imperfections in crystals can be commonly defined as “point defects”, when either atoms in the host crystal (intrinsic) or additive chemical impurities (extrinsic) is not in regular lattice position. The presence of point defects or impurities plays a major role in determining the electrical and optical properties of the host crystal.

The most dominative intrinsic point defect is a lattice vacancy, which is a missing atom or crystalline site. Given the importance of some binary oxide based semiconductors (e.g. CdO, In₂O₃, SnO₂, ZnO) [35], it has been postulated that a native point defect, such as oxygen vacancies, clearly establishes its prevailing n-type character according to: $O_o^x \leftrightarrow 1/2O_2(g) + V_o^{\cdot\cdot} + 2e'$. In principle, a generation of an oxygen defect releases two electrons, which is mainly contributed to the shallow electron states. Another vacancy defect is an extra atom in a non-crystalline site, which is transferred from a lattice site to the interstitial position. Interstitial atoms are considered to require a large amount of energy to immigrate into a close-pack crystal. If the energy of such defect-related states happens to be much deviated from that of states of the perfect crystal, the mechanism of electrical conductivity will be significantly affected by the motion of diffused atoms or ions. However, it becomes an important consequence that all types of metal oxide materials may not occur in the same configuration because their corresponding interstitial formation reactions yield noticeably different oxygen partial pressure (pO_2) dependence of conductivity [36].

The addition of a foreign atom in the fraction of a host crystal atom is known as “extrinsic point defect”. When the proper proportion of doping impurities was applied, the substitutions will take the place of a normal atom at the lattice site at equilibrium state, hence improving the operation of physical properties. Based on atomic size and formation energy considerations, substitutional impurities introduces relevant charge states differently within the band gap: (1) “deep level” is referred to the energy of the impurity-related states near the middle of band gap, while (2) it provides “shallow level” when the states lie close to the valence band (VB) or conduction band (CB). One example of such SnO₂ doping of Group-V elements (N, P, As, and Sb cations) was demonstrated by Varley et al. [37], to understand the effect of doping

mechanism in metal oxide semiconductor. Generally, it has been established that undoped SnO₂ crystal typically exhibit n-type conductivity due to the presence of its native point defects; tin interstitials (Sn_i) and oxygen vacancies (V_o). The electronic-structure calculations revealed that P, As and Sb strongly prefer to occupy the Sn sites to enhance “n-type conductivity” of as-grown SnO₂, in which the extra electrons in states below the CB freely move in the host matrix. In contrast, N is preferentially incorporated to the anion O sites (N_o), which has the lowest formation energy among other possible N defects under both O- and Sn-rich conditions (Table 2.1) [38], and act as a deep acceptor (p-type conductor). This is because the empty states known as “hole” was left right on the top of VB after N atom-occupied O site stimulates an electron to be excited out of the filled valence band to higher level states. Upon incorporation of donor or acceptor doping atoms, similar electronic-transition effects have also been reported in other metal oxide semiconductors such as binary oxides: Ga₂O₃ [39], Fe₂O₃ [40], TiO₂ [41], MgO [42], ternary oxides: CuAlO₂ [43], SrCu₂O₂ [44] and even co-doped metal oxides: (H, Al)-codoped ZnO [45], (N, F)-codoped TiO₂ [46], etc.

N-doped SnO ₂	O-rich condition	Sn-rich condition
N _{Sn}	3.7	12.9
N _O	0.68	2.0
N _{in-3}	4.4	8.3
N _{in-4}	6.3	10.2

Table 2.1 Formation energy (eV) of N-doped SnO₂ atom supercells in O-rich condition and Sn-rich condition [38].

Not only doping techniques have been broadly used to enhance the conductivity and the stability of various metal oxide thin films by modifying the energy band structure, but also optical transitions between impurity levels or other occupied conduction states could be a critical role to achieve optical property enhancement through absorption or emission characteristic of photons. Taking n-type TCOs (Sn-doped In_2O_3 ; ITO) as a prototype [36, 47], a high optical transparency is mainly determined by the factor: the fundamental band gap (E_g) becomes larger in fact up to $\sim 1\text{eV}$, with increasing carrier concentration from electron doping impurities. Figure 2.2 shows the magnitude of the shift (Δ_{BM}), indicated as dark area, due to the Burstein-Moss effect, which is attributed to allowed transition between the fundamental conduction band edge and the second conduction band (SCB). However, the band-gap shrinkage or renormalization (Δ_{RN}) occurs inversely due to an increase in the energy of the valence-band maximum (VBM) and decrease in the energy of the conduction-band minimum (CBM), when the excess of charge carriers was applied in the conduction band. Finally, the optical transparency in the visible wavelength range is maintained, defined as a difference of the two contributions, $\Delta E_g = \Delta_{\text{BM}} - \Delta_{\text{RN}}$. Somehow, the findings could be also adapted for understanding charge transport in optoelectronic devices based on other wide-band gap metal-oxides.

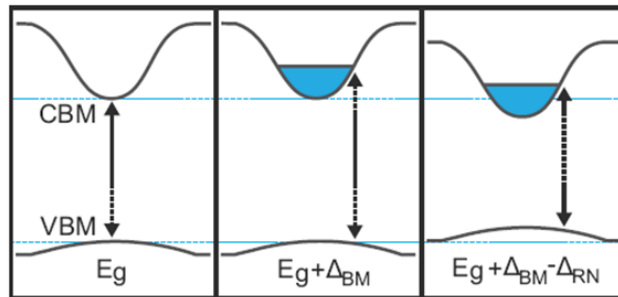


Figure 2.2 Schematic diagrams of charge transport in the energy transitions from the valence band to the conduction band [35].

2.2.2 Band-gap Engineering

In doping semiconductors, band-gap engineering in term of analytical model demonstrates how the presence of charge carrier concentrations based on external dopants is so crucial for the operation of electronic devices. The model basically interprets several effects such as excitation/recombination of charge behavior within the space-charge region, interface states at a thin oxide (depleting layer), the creation of the Schottky barrier (band bending) at the interface, and tunneling effect due to highly doped concentration. The operating mechanism begins when (1) the external electric field excited electrons from the donor-related state, instead of the VBM, to the CBM. (2) Or, similarly, electrons can be also excited from the VBM to the acceptor-related state and leave a delocalized hole at the original state, if the impurity state locates much closer to the VB than the CB. Consequently, any occurrence of these two cases results in generation of electron and hole (current), flowing in the direction of the applied electric field depending on their signs (+/-).

For two parts in the contact between metal-semiconductor or semiconductor-semiconductor, so-called “spatial inhomogeneities” were normally introduced by effective Schottky barrier (ϕ_B) at the interface, which also correlate with noise properties of Schottky diodes and grain boundaries [48]. The combination of the metal (or conductive oxide) electrode and the semiconductor affects the energy of electronic state on the semiconductor side. The different work functions (ϕ) between these two layers create a charge depletion region and band bending on the semiconductor, which hinder the electron transfer across the interface. However, corresponding to the relative position of Fermi levels (E_F), electrons (negatively charge carriers) move from the semiconductor (lower work function) to the metal (or conductive oxide) electrode (higher work function) until the Fermi levels align at the thermal equilibrium state. Like an

example as shown in Figure 2.3, when ITO transparent electrode and TiO₂ are brought into the contact [49], band alignment in a ITO-TiO₂ junction induces electrons moving from one side (TiO₂) to the other (ITO), responsible for overcoming the potential (Schottky) barrier (V_s). It indicates that the built-in barrier; $qV_s = q(\phi_m - \phi_s)$ and the shift in work function; $q\Delta\phi = q(\phi_m - \chi)$, where χ , ϕ_m and ϕ_s are the electron affinity, the work functions of ITO and TiO₂, respectively. To achieve higher efficiency and yield, this work investigated a simple way to conserve the electrical conductivity of ITO films under post annealing process by applying a reducing H₂ gas. As a result, this method could prevent annihilation of oxygen vacancies (free carriers generating the electrical conductivity) from oxygen in the atmosphere. In principle, the increased optical band gap of ITO may occur because the additional donor electrons occupy the energy states above the CB, which could higher the Fermi energy level, i.e., reducing the Schottky barrier at the interface. Therefore, the H₂-annealed ITO electrode was assumed to employ significantly improved interfacial charge transport due to decreased internal resistance of the cell.

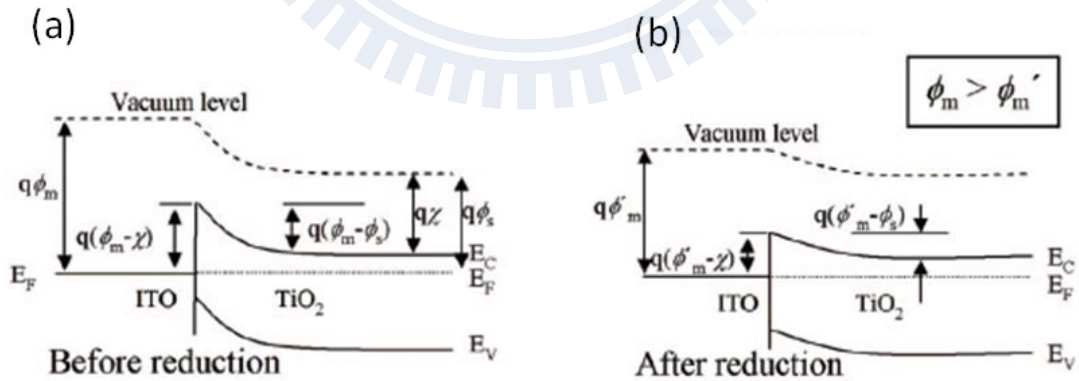


Figure 2.3 Illustration of band alignment and the Schottky barrier formed at the junction of conducting oxide (ITO) and semiconductor (TiO₂) (a) before and (b) after H₂-gas reduction [49].

Furthermore, improvement of interfacial adhesion has been a matter of intensive study. The advantages and disadvantages of various common techniques depend on a variety of factors, such as contact area, charge-transport dimensionality, structural similarity, and charge recombination. For instance, poor interfacial contact (TiO₂/FTO), encountered in nanoparticulate film-based devices, can be tailored by a UV laser welding [50]. One obvious evidence as electrochemical impedance analysis (Z) proved that the contact resistance decreased proportional to an increase in the power of laser beam upto 0.5 W. It was claimed to be a simple, fast, and adaptable for any other efficiency improvement schemes. However, since a thin region of the interface was locally involved in this technique, the experiment must be very tricky to handle. The exceeded irradiation might readily damage the TiO₂ particles or even degrade the conductivity of the ITO film.

Similarly, in the case of p-n junction, two parts in contact are basically composed of one semiconductor doped with donor impurities (n-type) and the other one doped with acceptor impurities (p-type). Due to high mobility of the carriers (electron and hole), they diffuse toward the opposite directions; electrons move to p-doped side and holes move to n-doped side. At the p-n junction, the energy bands of the semiconductors must bend, also forming a depletion region corresponding to the alignment of Fermi energy level in both p and n-doped layers. This consequence leads to a rectifying behavior in oxide materials, which has been reported in term of “homojunction” or “heterojunction” diode. Toru et al. [51] have fabricated a ZnO-homojunction diode by using laser phosphorus (P) doping to form a p-type ZnO layer on a typically n-type ZnO substrate. Band-edge emission ($\lambda = 370\text{-}380\text{ nm}$) and broad peak ($\lambda = 400\text{-}500\text{ nm}$) of the ZnO diode was revealed via the electroluminescence spectrum under forward current injection at

110 K. The light emission of white-violet color was observed, which is evidently caused by a band-edge component of defect states.

In addition, p-i-n (p-type/intrinsic/n-type) heterojunction diodes [52] commonly offer another approach for improving the rectifying configurations of abrupt junction in ordinary p-n diode [53]. Figure 2.4a displays the structure of transparent p-CuYO₂:Ca/i-ZnO/n-ITO diode. It concluded that using the selective materials with their proper band-gap mismatch could lead to a smooth transition as shown in Figure 2.4b. This can develop the injection of electrons from n-ITO to p-CuYO₂, while the flow of space-charge-limited current is attributed to the single-carrier injection in the i-ZnO layer. The possible applications of p-i-n diode have been widely used in many branches such as fast switches, photodetectors, and high voltage power electronics [54, 55].

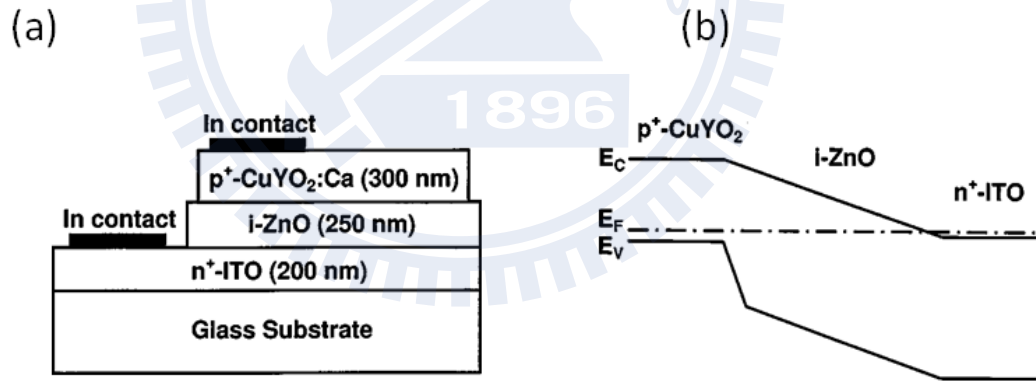


Figure 2.4 (a) Structure and (b) equilibrium energy band diagram of the CuYO₂:Ca/ZnO/ITO p-i-n heterojunction diode coated on glass substrate [52].

2.3 Surface modification in nanoscience and nanotechnology

2.3.1 Surface passivation

A wealth of the techniques with controllable temperature and doping concentration has been widely reported by various research groups, with notable purposes including surface passivation [56], functionalization [57, 58] and etching [59, 60]. Song et al. [56] demonstrated the passivation effects of a polymethyl methacrylate (PMMA) on the electrical characteristics of ZnO nanowires, under various oxygen environments. They found that the surface passivation can prevent oxygen ions (O^- , O^{2-} , or O_2^-) from being absorbed onto the defect site (V_o^{2+}) of ZnO nanowires, where such intrinsic defects (V_o^{2+} and Zn_i^{2+}) attribute to the n-type conductivity in ZnO. Then, the electrical characteristics of the single ZnO nanowire with and without coating PMMA passivation surface were compared via the field effect transistors (FETs) devices under ambient air (20% O_2), dry O_2 , and vacuum ($\sim 10^{-3}$ Torr) environment. In Figure 2.5, the output $I_{DS}-V_{DS}$ and $I_{DS}-V_G$ curves indicates that carrier concentration, mobility, and threshold voltage of the as-grown ZnO nanowires were significantly influenced proportional to increasing in the contents of oxygen environment, while the passivated samples remained unchanged due to no electrons trapping to the oxygen molecules at the surface.

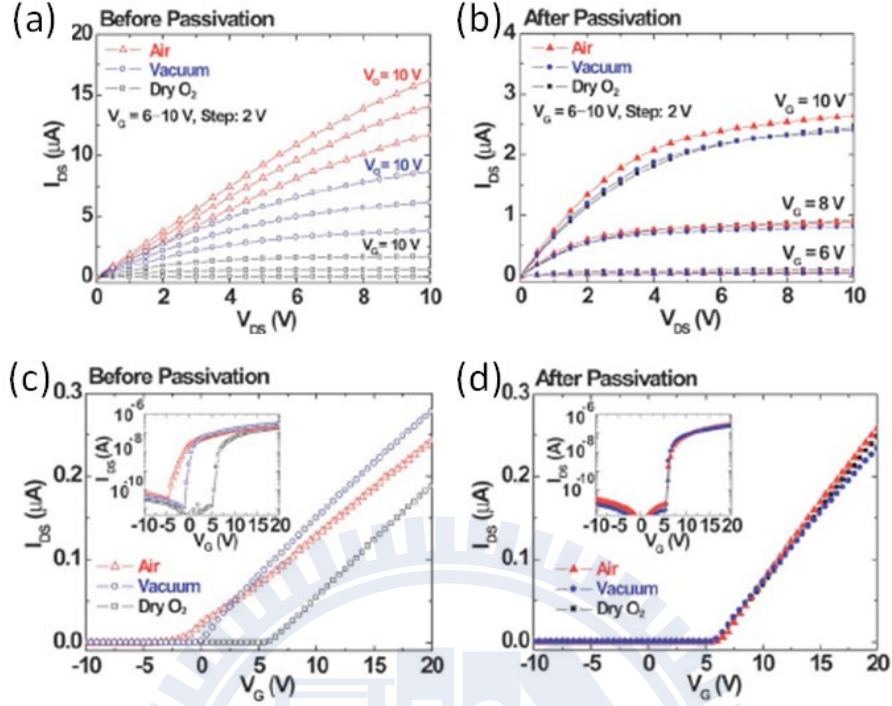


Figure 2.5 I_{DS} - V_{DS} curves (at different gate biases: 6, 8 and 10 V) and I_{DS} - V_G curves (at $V_{DS}=0.1$ V) of a ZnO nanowire FET under ambient air, dry O₂, and vacuum conditions as compared between (a, c) before and (b, d) after PMMA passivation, respectively [56].

As mentioned above, it also suggests that the performance characteristics of heterostructure nanodevice primarily rely on the quality of growth interface. Combining two materials with the same crystal structure is assumed to offer well-defined and clean interface of the epitaxial growth films associated with passivation of surface defect density. However, this concept was also adapted for using in the epitaxial growth of other couple materials with different crystal systems. Such SnO₂/ZnO heterojunction nanocatalyst core-shell was successfully synthesized by which it exhibits the possibility of using in various types of application [10, 61, 62]. Architecturally, the 3D epitaxial heterostructure for superlattice

structures [63, 64], coaxial [65-68], and biaxial [69-71] nanowires or nanocables were developed and applied to the DSSCs, in order to enhance the overall device efficiencies with a consideration of high aspect (surface-to-volume) ratio and catalytic activity. Herein, to understand detailed information about the microstructure and morphology of core-shell nanowires, SEM images and their insets can be seen in Figure 2.6 that the uniform-size distribution can be readily obtained, while the shell thickness was varied with the number of the atomic layer deposition (ALD) cycles [10].

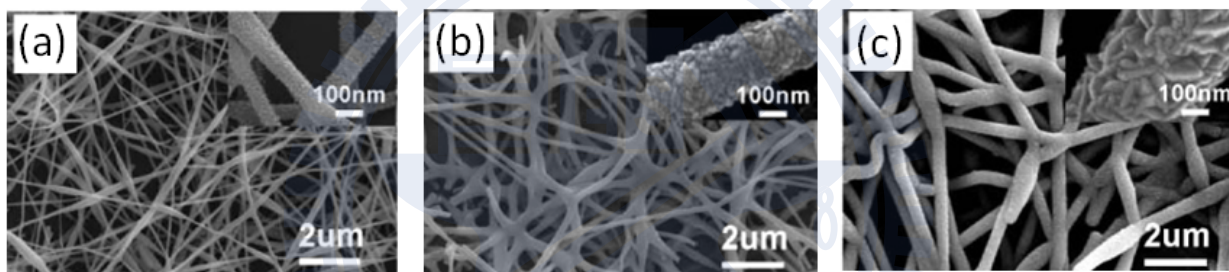


Figure 2.6 SEM images of $\text{SnO}_2\text{-ZnO}$ core-shell where the SnO_2 nanofiber was synthesized by electrospinning and the ZnO outer layer was deposited with different ALD cycles of (a) 0, (b) 100, and (c) 400[10].

However, Kuang et al. demonstrated that HRTEM images (Figure 2.7) evidently revealed more understandings about layer-to-layer interaction. As a result, although the ZnO nanorod was completely coated with a well-crystalline SnO_2 layer, the lattice mismatch (misfit dislocation) between the SnO_2 shell and ZnO core might be induced due to the injection of structure defects and stress through the epitaxial layers [62]. Accordingly, it becomes very important to further

develop this strategy by selecting correlated hybrid materials in responsible with using suitable fabrication methods.

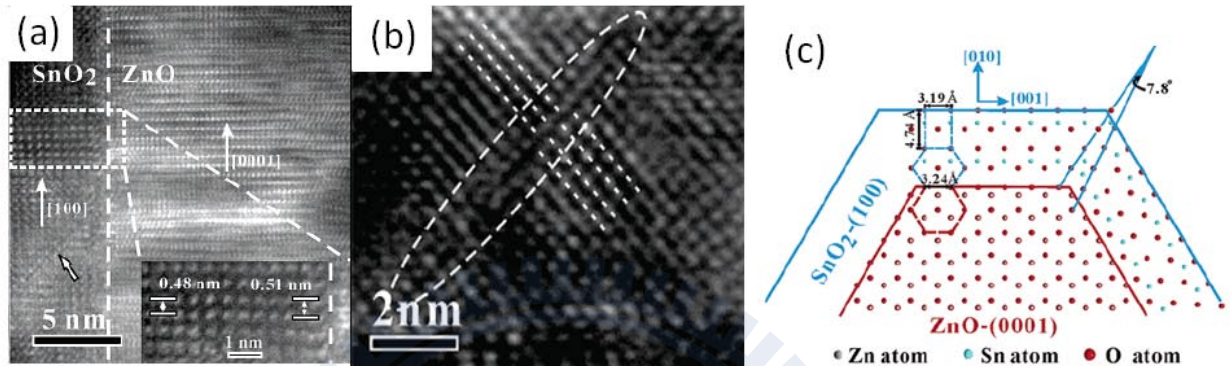


Figure 2.7 (a) TEM image of a ZnO-SnO₂ core-shell nanorod where the inset shows a magnified image of the crystal fringes in the SnO₂ shell. (b) High-magnification TEM image reveals misfit dislocation in the SnO₂ epitaxial layer. (c) Schematic model of the atomic arrangements of the SnO₂ hexagonal nanoring on the (100) plane surrounding a ZnO nanorod on the (0001) plane [62].

2.3.2 Surface treatment by plasma

Several semiconducting metal oxides such as ZnO, SiO₂, In₂O₃, and SnO₂ serving as direct wide band gap materials are strongly affected by the chemical adsorption of ambient gases. In this approach, the surface modification methods using a dry plasma treatment represents straightforward route to change the structural, optical and electrical properties via surface energy band bending due to the generation or degeneration of additional or removal molecules in defect sites.

In atmosphere, water molecules normally physisorb with the hydrogen sides to the metal oxide surface in order to introduce the lower free energy and the overall stability of the system. For example, the hydroxyl groups (OH⁻) of water molecules were weakly bound to ZnO surface at the positively charged active sites (Zn²⁺-OH⁻), which will subsequently capture the electrons as illustrated in Figure 2.8 [57, 58, 72]. According to the reason, this topic deserves further investigation regarding to the incorporation of surface treatment on the physical properties of metal oxide materials. Recently, the study of oxygen plasma assisted epitaxial ZnO thin film growth [73] revealed the creation of the rectifying behavior, therefore improving the UV detector characteristics as compared with the ohmic behavior in the untreated samples. The XPS (O 1s core level) spectra in Figure 2.9 exhibit the removal of conductive OH layer accumulated at the surface; the deconvoluted peaks show an increase in the relative intensity of the O-Zn peak to the O-OH peak when the plasma treatment time was increased. This indicates the abundance of atomic oxygen radicals filling into the oxygen vacancies of the host lattice, which is able to lower the Fermi level (E_F) in the band gap and create band bending upward. The oxygen plasma treatment not only eliminates all detectable hydroxide and hydrocarbon contaminations leading to an increase in surface conductivity, but also the formation of Schottky barrier are much suitable to gold , platinum contact, etc., due to its low oxygen affinity [74].

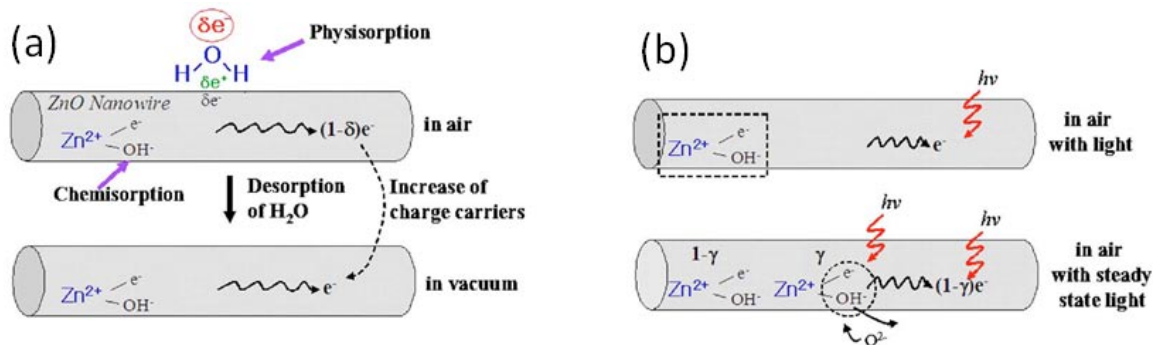


Figure 2.8 Schematic drawing of ZnO nanowire shows (a) the influence of physisorbed water molecules in air, capturing free electron and inducing a low-conductivity depletion layer at the nanowire surface. The current is increased under a vacuum condition due to a desorption of the water molecules. (b) Upon illumination with UV in air, electron-hole pairs are generated, while the carriers are decreased with the replacement of the hydroxyl group by oxygen ions from the steady light [57].

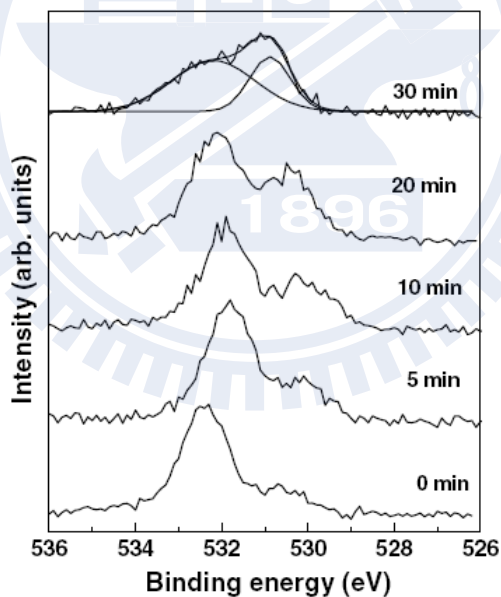


Figure 2.9 XPS spectra of O 1s core level from untreated and oxygen plasma treated (5-30 min) ZnO films [73].

In case of SnO₂, the surface electronic states are also affected by oxygen plasma [75, 76]; the absorbed oxygen species from oxygen plasma were expected to induce the reduced SnO_x surface, where the Sn²⁺-O bonds existed, by forming the damaged (depleting) layer on the surface. In a detail, this phenomenon was demonstrated by the energy level diagram in Figure 2.10. The energy bands at the surface bent upward (denoted by “ ϕ_B ”) after oxygen plasma treatment, resulting in a surface accumulation layer and additional electron trap states. When a depleting layer was produced, the electron affinity (χ) is reduced, hence making contribution to the formation of a Schottky contact with Au electrode, used in various applications. On the other hand, to treat the samples under N₂ gas annealing, the incorporation of nitrogen atoms in the SnO₂ host matrix [38, 77] introduced possible mechanisms in the opposite way. The interstitial and substitutional N atoms preferentially located in anion sites due to low defect formation energies in the O-rich conditions. In principle, density function theory calculations revealed a major possibility that the N atoms are energetically favorable to occupy the O site within a limitation of diffusion depth. In this process, the introduction of such defects or impurities can change the surface chemistry by surface oxidation, thereby recovering the Sn⁴⁺-O bonds (SnO₂ phase). This can enhance the field emission characteristics of SnO₂ due to decreasing in the emission barrier and the work function (ϕ) at the depleting layer.

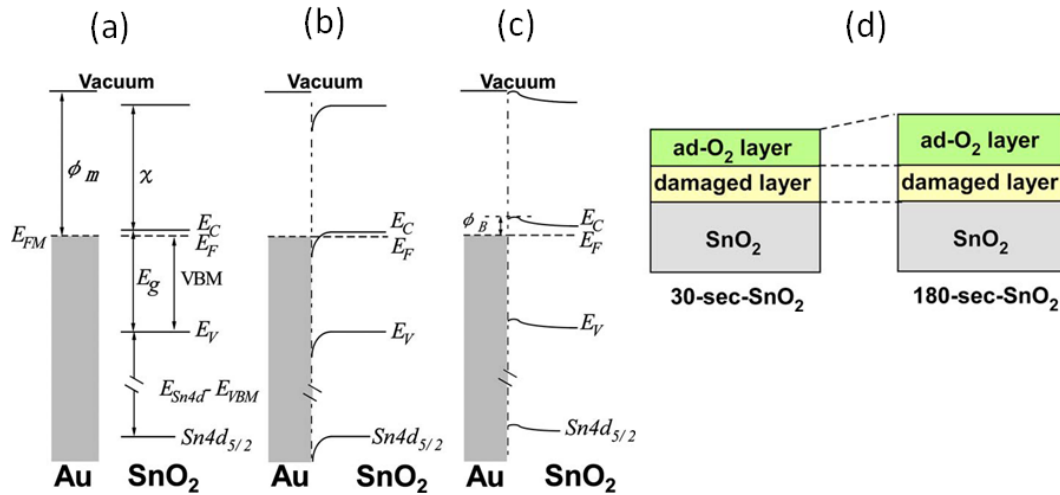


Figure 2.10 (a) Idealized energy band diagram for an Au/SnO₂ interface. Band alignment of Au contact on (b) an as-deposited SnO₂ film and (c) an oxygen-plasma treated SnO₂ film. (d) Structures of the SnO₂ films exposed under different oxygen plasma-treated time (30 and 180 s) [75].

As scaling down of complementary metal-oxide-semiconductor, the effect of defects on the physical properties increases with decreasing in dimension of material. The improvement of quantum physics limitation might require the ability of such plasma technology to deliver high throughput, conformal coverage, and reproducibility at low substrate temperature. For these advantages, different plasma-involved methods have recently been extended to use in the numerous applications of metal oxide nanostructure including transparent conductors [78], electrochromics [54], Li-ion batteries [79], photovoltaic cells [80], gas sensors [81], and complex oxides [43]. Typically, plasma system is used as a passivation technique by different gaseous carriers, which can effectively reduce the surface or interface trap states. Recently, a reversible process to control the characteristics of SnO₂ nanowire transistors (NWTs) has been proven by reducing the V_o under the N₂ plasma exposure and recovering after ultraviolet-ozone

(UVO) treatment, alternatively [82]. The lower concentration of V_o , which acts as a donor type defect to produce electrons in NW, might decrease the conductivity when nitrogen ions were filled into the V_o sites. Under a subsequential treatment of UVO radiation, the O atom could react with N ion-substituted V_o to form NO_x , which is likely to detach from the surface. Finally, the reproduced V_o was obtained leading to an increase in conductivity at its initial state. However, this study has been found in contradictory with the other previous reports [37, 38, 83], which are related to the mechanism of N-incorporated SnO_2 ; Pan et al. [83] examined that atomic N could actually prefer to substitute at O sites in SnO_2 , due to the lowest formation energy among the other defects. Hall probe measurement shows the enhancement of p-type conductivity with increasing N doping concentration, in which the generation of dominative acceptors is highly possible to compensate n-type conductivity of the intrinsic defects.

Recently, semiconductor nanocrystals (quantum dots-QDs) have been used to combine with low-dimensional metal oxides to enhance the efficiency of solar cell devices because the tunable size of QDs can basically provide the ability to match their absorption wavelength with the solar spectrum. Instead of using capping or linking agent [84-87], plasma treatment becomes another suitable technique for developing interfacial properties in such hybrid materials. For example, oxygen plasma could modify ZnO NWs surface in order to improve CdSe QDs absorption [88]; O ion bombardment was assumed not only to remove the surface-bound contaminants in ZnO surface such as hydroxyl (OH) and hydrocarbon (C-H) groups, but also to create the dangling bonds of carboxyl (COOH) group on the species to increase the colloidal QDs attaching on the ZnO NW surface. A consistent result was also obtained with I-V characteristics of dye-sensitized solar device where the higher QD coverage may cause an enhancement of light absorption, electron injection, and generated photocurrent, respectively.

2.3.3 Surface etching by plasma

In terms of nano-architectural device, conventional lithography techniques widely offer one possibility for the fabrication of requisite structures, spanning the size in the range of 10-100 nm. There is a number of different techniques such as soft lithography [89], colloidal lithography [90], and electron lithography [33], which were used for 2D or 3D patterned surface combined with template-directed synthesis. Among several nanomaterials including hollow-core, tubular, porous, and nano-array structures [59, 60] have promoted unique chemical and physical properties because of their ultralarge surface areas and inherent catalytic activities. One important methodology in the lithographic process is associated with “plasma etching technology”, which allows high throughput and simple control of the operating parameters (plasma source, etching gas, flow rate, etc.). Thus, a higher scalability of selective-plasma etching has been successfully applied to remove metal oxide [59] or organic templates [60] with remaining original crystalline structures of unetched portions, as compared with thermal decomposition (the Kirkendall effect) [91] or wet chemical etching [92].

For metal oxide nanostructure, a primary technique that determines dry etching mechanism in this interest is reactive ion etching (RIE) method. It is one of most well-known methodologies in terms of top-down etching techniques, large operating area, and high density at relatively low pressure (10^{-1} - 10^{-4} Torr). RIE consists of a glow-discharge-generated plasma where chemically reactive gases are added to gain higher etching rates via selective bombardment of reactive species: radicals (chemical selectivity) and ions (physical removal of substrate species). In a detail, RIE introduces a negative charge (electron produced in the plasma) at the substrate, while the positive ions are simultaneously accelerated toward the surface plane resulting in a creation of more reactive surface. In this case, an anisotropic etching might be

achieved and able to produce high aspect ratio features, if low plasma potentials (<100 V) and high rf biases (>500V) are applied. An example of the fabrication of binary and ternary particle arrays with nonspherical building blocks was done by RIE under O₂ plasma [90]. This approach used different structures of colloidal arrays as nanolithography masks, being self-organized, onto the PS bead-coated substrates. As illustrated in Figure 2.11, 2D patterned structures possess for organizing some common geometries, which depend mainly on two basic concepts regarding to: (1) different colloidal arrangements will give different final structures, i.e. fcc and hcp crystal structures in the stacking of the hexagonally close-packed (111) layers. (2) The use of either pure O₂ or O₂-CF₂ mixture plasma could introduce an anisotropic RIE, which is sufficiently severe for etching the voids of interstices between the colloidal particles, without disturbing their ordered structure.

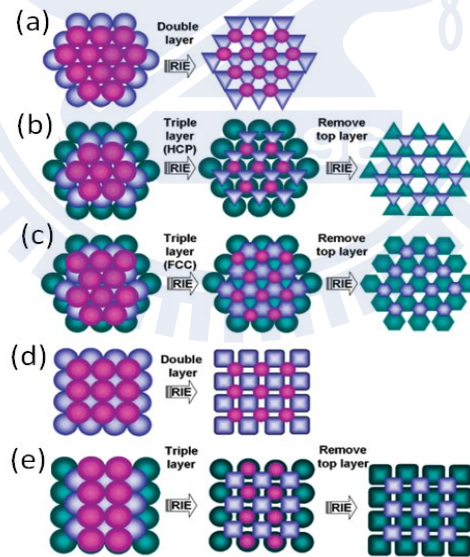


Figure 2.11 Illustration of the colloidal lithographic concept with some 2D geometrical structural units: (a) hexagonal double layer, (b) hexagonal triple layer (HCP), (c) hexagonal triple layer (FCC), (d) square double layer, and (e) square triple layer [90].

To be more specifically, plasma etching mechanism for a fabrication of metal oxide materials can be mainly divided into two types: positive etching and negative etching. Positive etching is attributed to removing soft template that is coated by oxide materials on the outer surface. Like in core-shell structure reported by Moon et al. [60], TiO₂ hollow hemispheres were fabricated by using polystyrene (PS) beads as a template (Figure 2.12). The size of PS core-template tended to shrink when it is initially impacted by oxygen ions from O₂-treated plasma, for which low operating pressure improves diffusion of ions and reactive species through inter-grain of the TiO₂ shell layer. Finally, a TiO₂ hollow structure with the monolayer-film thickness of 150 nm was produced. Noted that this type of core-template film is much suitable for using dry plasma etching method due to ultra-small etching technique, by which high surface area and small interface area between the film and the substrate significantly enhanced gas sensitivity compared to conventional (flat) thin film.

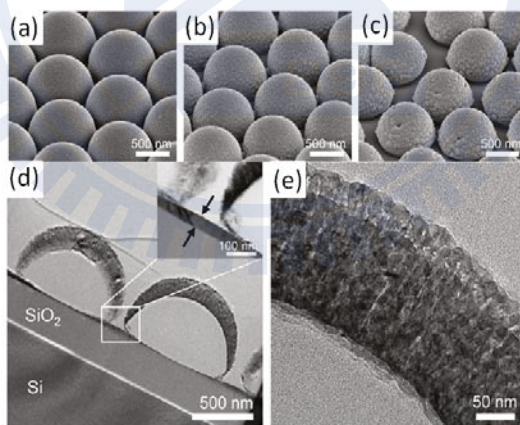


Figure 2.12 SEM images of the resultant embossed TiO₂ films coated on polystyrene bead templates (a) without O₂ plasma etching, and O₂ plasma etching for (b) 2 min and (c) 4 min. (d) Cross-sectional TEM image of a hollow TiO₂ hemisphere with TiO₂ film deposition at intervals as shown in the inset. (e) High-

magnification TEM image from the TiO_2 shell showing polycrystalline layer with thickness (~ 150 nm) and grain sizes (10-30 nm) [60].

On the other hand, negative etching can be often seen in terms of porous membrane used as anodic aluminum oxide (AAO). The nanoporous membrane is the most widely used sacrificial template for the construction of 1D metal, metal oxide, and polymer nanostructures. AAO template can be dissolved to liberate free-standing nanorod or nanotube arrays, offering excellent size uniformity in diameter and length. Unlike the positive etching, it permits the synthesis of aligned, electrically connected arrays of nanocomposites without the need to self-assemble the template. However, interestingly, deposition methods used in positive templates can be applied to the secondary templates for the negative etching methods. In particular, Fan et al. [59] proposed fabrication of silica nanotube arrays from vertical silicon nanowire. As shown in the flowchart in Figure 2.13, oxygen plasma was employed to etch the top-surface (step 3) and the entire matrix (step 5) of parylene template membrane. It indicates that this oxygen plasma etching in the multistep approach play a main role for making silica nanotube arrays with its well-controlled and accurate process depending on the applied power and duration.

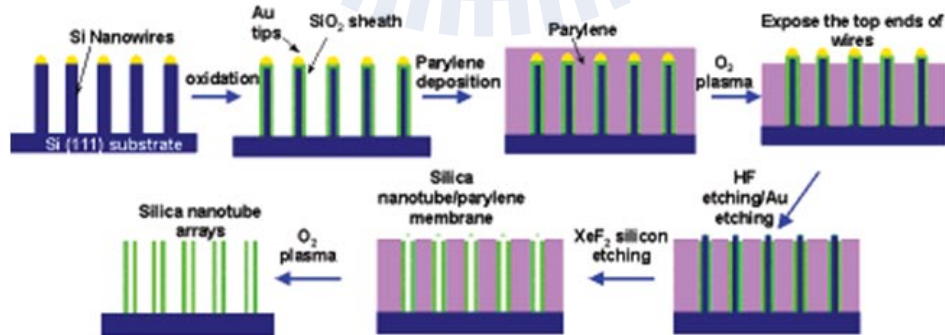


Figure 2.13 Flowchart for ordered silica nanotube arrays, fabricated by using vertical silicon nanowire templates [59].

2.4 Solar cells-based Transparent Conducting Oxide (TCO) semiconductors

2.4.1 Perspectives and evolutions of solar cells

The large abundant of solar energy promises to be a vital source of clean and renewable energy being developed to minimize future climate changes. Effective utilization of solar energy relies on the development of efficient photovoltaic devices. However, the large-scale implementation of conventional silicon-based solar cells still remains more expensive in term of the produced electricity cost, compared with traditional fossil fuel-based sources of power. In a consideration, the most extensively studied solar cells are based on the improvement of energy conversion efficiency being comprised of inexpensive materials, low environmental contamination, and optimum band gap-maximized solar absorption. Herein, we focus two important types of photovoltaic cell; hydrogenated amorphous silicon (a-Si:H) and dye-sensitized solar cells. Therefore, we can gain more understanding about how to enable the novel conversion mechanism by using small-scale and low-cost processes.

2.4.2 Hydrogenated amorphous silicon (a-Si-H) solar cells

The a-Si:H films have been used to fabricate solar cells as a choice to provide the advantage of lower costs and less material required than crystalline silicon solar cells (c-Si). This material is easy to deposit on a wide range of substrates (flexible, curved, and roll-away types), suitable for large area applications with high overall efficiency around 10%. However, the amorphous Si contains many defects, which results in a small minority carrier diffusion length. Therefore, a film of active material is required a sufficient thickness equal to the diffusion length

to absorb light, effectively. Moreover, the increase in defect density may degrade the amorphous film due to illumination, which breaks the dangling bond of hydrogen from the fourth silicon bond. The higher defect density will capture more electrons created by photon. Lately, researchers have found ways to compensate the effect by using hydrogen as the carrier gas during film deposition. Two main methods for depositing a-Si:H film were proposed including: (1) Silane-based (SiH_4 gas) glow discharge induced by plasma enhanced chemical vapor deposition (PE-CVD) and (2) hot-wire catalytic deposition [93]. Unfortunately, although the hydrogen diffusion in this stage is expected to result in the formation of dangling bond, a large impact of generated hydrogen ions and radicals prefers to segregate at the interfaces between epitaxial layers and grain boundaries and then causes the degradation of properties of metal oxide semiconductors (TCO electrode). Regarding to the density of hydrogen incorporated in the film, the use of various manufacturing techniques may be possible to overcome this problem. Hayashi et al. [94] reported that chemical reactions and hydrogen-related effect contribute to the properties of a-Si_{1-x}C_x:H (p-layer; x=0.28)/SnO₂ interface in the cell where the reduction of SnO₂ was occurred by activated plasma decomposition of B₂H₅. To prevent Sn diffusion and its incorporation in the p-layer, an a-Si₃N₄:H barrier layer was inserted between those two layers by the plasma CVD nitridation of ultra-thin a-Si:H. The XPS spectra showed that the formation of Sn-N bond in the barrier layer plays a key role to reduce the Sn-doped a-Si_{1-x}C_x:H and increase the density of states in the valence band tail near the Fermi level.

2.4.3 Dye-sensitized solar cells (DSSCs)

The DSSCs-based photovoltaic devices that rely on the conversion of photons of sunlight into electricity have become an intensively rectified alternative as the most efficient solar cells technology available. To date, the advantage of this device is to provide more feasible energy-conversion efficiencies, up to 11%, with requiring cheap and large-scale manufacturing process than the conventional silicon-based photovoltaic [95, 96]. In particular, the schematic drawing in Figure 2.14 illustrates the operating system of the cell which is composed of conductive glass electrode (anode), TiO_2 (semiconductor layer), dye (photosensitizer), electrolyte (electron transfer mediator), and counter electrode (cathode and catalyst of electron transfer). These features basically associate with the optical absorption and the charge separation in a photo-electrochemical cell, so that this configuration can prevent the contacting-phase effect of solid-solid junction. In the reaction, the excited state of photo-absorbed dye principally generates photoelectron, which induces injection of the electron transport to the conduction band (CB) of TiO_2 and the conducting glass electrode (collecting anode). At the end, the electricity is produced, however; the oxidized dyes are reduced by redox species according to one electron has jumped to TiO_2 . Therefore, the dye molecules are compensated by capturing another one from the iodide electrolyte. Concurrently, the iodide (I_3^-) can regain its lost electron to equilibrium state in turn by reduction of triiodide (3I^-) at the counter electrode, where the electrons are resupplied through the external circuit.

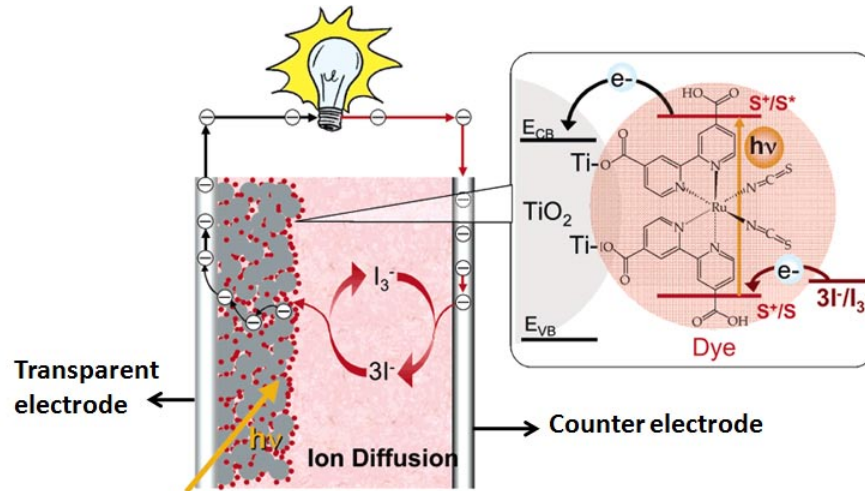


Figure 2.14 Schematic representation of the principle of the dye-sensitized photovoltaic cell operating under illumination [96].

The monochromatic current yield defined in term of incident photon to current conversion efficiency (IPCE) can be expressed as the equation below, mainly corresponding to the photon flux that strikes the cell, the photoexcited electron that injects into the semiconduction layer and conductive electrode, and the dark reactions that occur during the light-to-electricity conversion.

$$\text{IPCE}(\lambda) = \text{LHE}(\lambda) \times \phi_{inj} \times \eta_{coll}$$

where $\text{LHE}(\lambda)$ (light harvesting efficiency) is the fraction of the incident photons of wavelength λ that are absorbed by the dye, ϕ_{inj} is the quantum yield for the subsequent charge injection into the crystallites that renders the TiO_2 conductive and η_{coll} is the electron collection efficiency at the back electrode (anode).

To go further, experimentally, another equation that refers to the overall conversion efficiency (η) of DSSCs consists in assuming the relations among the photocurrent density measured at short circuit (I_{sc}), the open-circuit photovoltage (V_{oc}), the fill factor (FF), and the intensity of the incident light (I_s):

$$\eta = \frac{I_{sc} \times V_{oc} \times FF}{I_s}$$

Supposing that the measurement is done under solar radiation through AM (airmass) of 1.5 and intensity I_s of 1000 W/m^2 . It is known that the FF can be affected by the values of the cell's series and shunt resistance, while the V_{oc} generated under illumination corresponds to the difference (ΔV) between the Fermi level in the semiconductor and the redox potential of the electrolyte.

However, one of the major limitations in DSSCs is the relatively low charge collecting efficiency of a TCO layer; the leakage of electron transport occurred at the interface between the conducting glass and the semiconductor layer, which may increase the recombination rate of photoinduced electron-hole pairs. Therefore, to further improve the efficiency of DSSCs, considerable attempts have been involved on novel development of nanostructure building blocks.

Some success in approaching this concept has been achieved by several methods to maximize the surface area, using nano-scale architecture semiconductors instead of bulk (flat) materials. Sander et al. [97] demonstrated a template-directed approach for producing TiO_2 nanotube arrays on silicon substrates by using atomic layer deposition (ALD). The method enables to precisely control the tube-wall thicknesses in the regime where the tunable size

(diameter, spacing, ordering, and wall thickness) affects efficiency in photovoltaic devices. Kang et al. [98] showed that nanorod-based DSSCs lead to the enhancement of energy conversion efficiency (6.2%), compared with nanoparticle-based DSSCs (4.3%). Their investigations was focused on a reduction of intercrystalline contacts between grain boundaries, and 1D stretched grown structure could slightly facilitate the electron transport in the specific directionality contributing to the increase of enhanced electron life time and diffusion length. Wang et al. [99] proposed the advanced nano-encapsulated structure, which was formed in term of so-called “3D electrode”; TiO₂-embedded ITO nanowire arrays. Photoelectric conversion efficiency as high as 4.3% was achieved rather than that of pristine film type. Recently, Yang et al. [100] minimized the deterioration of device performances in the use of typical 1D nanostructured electrode due to introducing the series resistance and roughness factor. A novel architectural design was composed of grown ZnO nanotips as semiconductor component on host Zn microtip arrays as an electro-collecting anode (Figure 2.15). Obviously, to enable the scalable size effect, the rough portions were allocated to the collecting anode instead of imparting them onto the semiconductor layer attached to the anode. Their results suggested that increases in fill factor, compared with the ZnO nanowired-based DSSCs, were related to extension of the recombination time for the excited charge carriers. This is because the short length of the ZnO nanotips plays an important role in faster process of the electron collection, which can suppress electron trapping by electrolyte. As a consequence, the open-circuit voltage is also enhanced due to the enlarged potential barrier between the quasi-Fermi level and the redox species under illumination, which leads to the electron accumulation at the Zn/ZnO interface and hence improves the overall efficiency of DSSCs device.

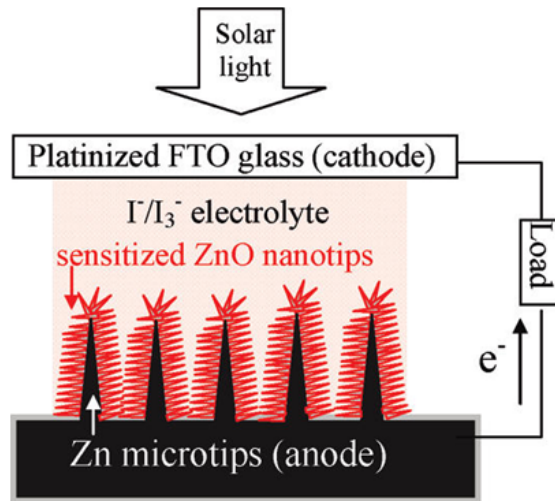


Figure 2.15 Schematic drawing of the DSSC. An array of Zn microtips, grown vertically from conductive glass electrode and decorated with ZnO nanotip hierarchy, serves as the photoanode [100].

In other words, another approach is the use of hetero-structures for a conducting electrode, which has made available new material platforms and alternative device-fabrication techniques. These emerging technologies will improve the sensitivity, reliability, and electron transport properties of next-generation solar cells due to the epitaxial interface effects. Such the applications of multilayered TCOs; for example, Nb-doped TiO₂ (NTO) layer [101] and F-doped SnO₂ (FTO) [102] coated on Sn-doped In₂O₃ (ITO) conducting layer could enhance the thermal stability, hence prevent deterioration of the electrical properties of the ITO films, after the thermal annealing process that is essential for a phase formation of components. The investigators found that multilayered TCOs exhibited dramatic improvement in the overall energy conversion efficiency as much as 17% compared to that of bare ITO-based DSSCs [101]. This behavior was explained through compensating the defect complexes in which the overlayer can suppress the formation of interstitial-oxygen-related defect (O_i) during air annealing.

Generally, by the reason that conducting TCOs film/semiconductor (TiO_2) NPs interface contains a large internal spacing among numerous grain boundaries. Consequently, electron trapping and detrapping process may give a rise to the charge recombination due to a loss of photogenerated electrons during the redox reaction in electrolyte (Figure 2.16) [103].

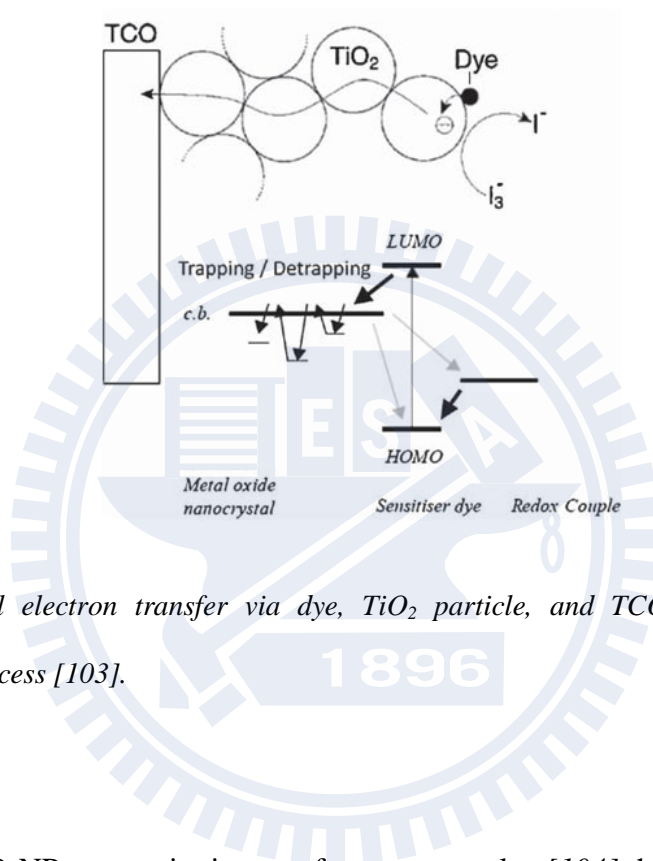


Figure 2.16 Interfacial electron transfer via dye, TiO_2 particle, and TCO electrode, involving a trapping/detrapping process [103].

The ZnO NW-ZnO NP composite is one of many examples [104] that introduced the use of hybrid nanostructures to overcome the charge recombination in photoelectrode, as FTO conducting layer of DSSCs. As shown in Figure 2.17, the unique configuration was contributed to increasing the contact area between photoelectrode and sensitizer dye, while the nanowire acts as one-directional pathway to boost the electron transport toward the conducting layer. The investigation showed that the performance of the NW-NP composite is mainly influenced by the ZnO NW well-adhered on the single-crystalline ZnO at the 6.2 μm thick composite film.

Nevertheless, it can be pointed out that, without annealing treatment, layered basic zinc acetate (LBZA) might be remained as the large fraction of as-deposited NP, which can form the insulating overlays (electron blocking barrier) in TiO₂-NP DSSCs. Therefore, different annealing procedures were carried out to improve the phase crystallinity and interfacial adhesion, hence provide faster electron transport. By optimizing the process, the superior efficiency (η) of 3.2% was finally obtained.

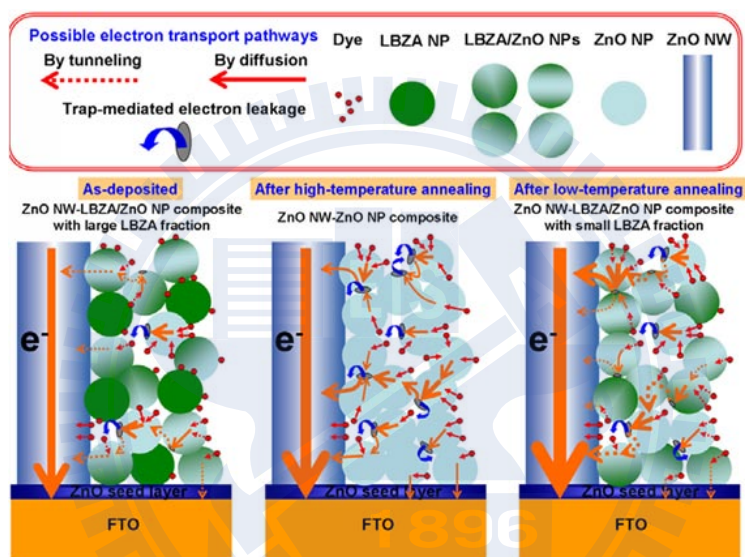
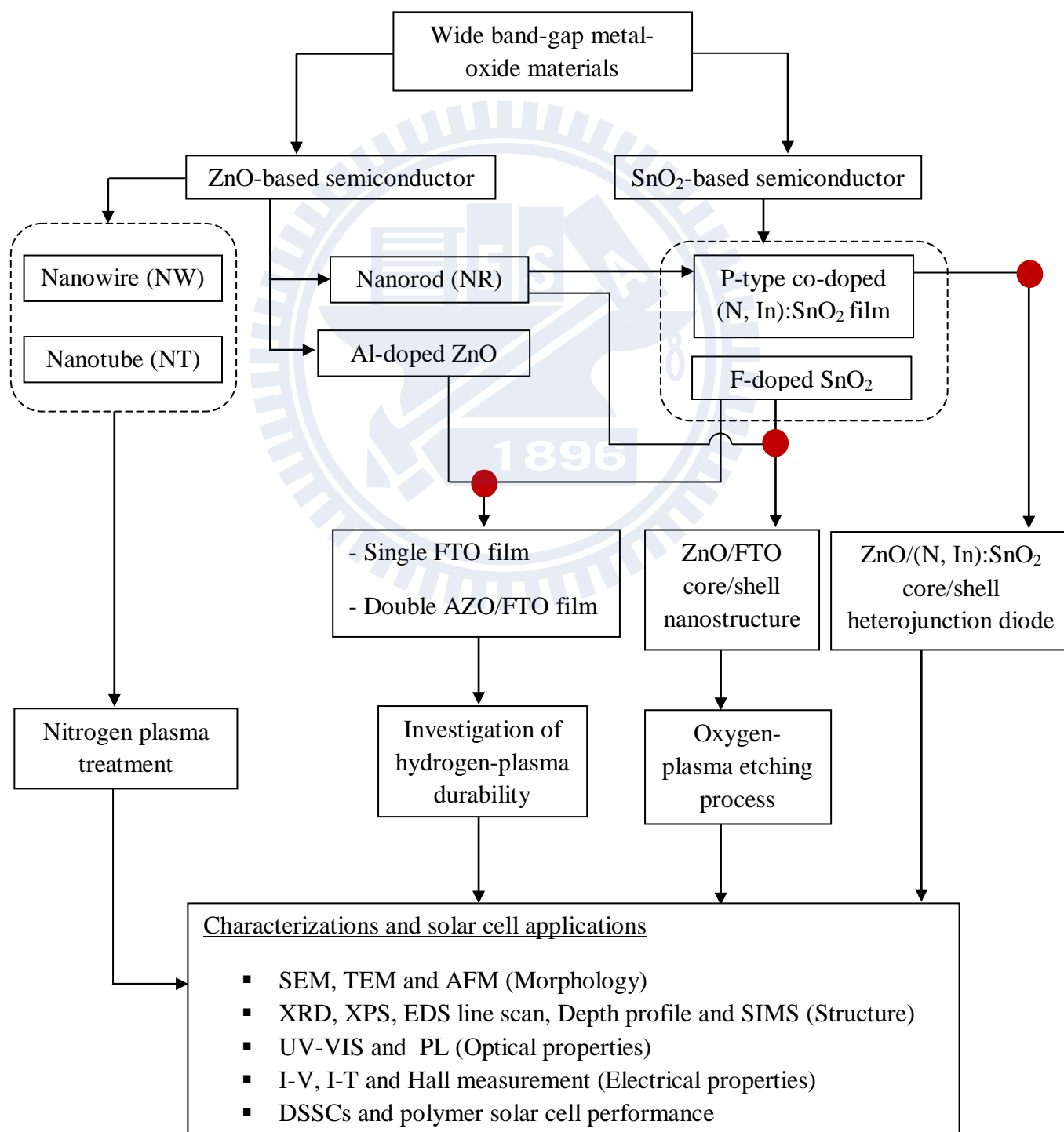


Figure 2.17 Directing the flow of photogenerated electrons across the nanostructured semiconductor ZnO NW/ZnO NP composite and the possible electron transport mechanism regarding to the annealing treatment process [104].

Chapter 3

Experiment methods

3.1 Experiment overviews



3.2 Preparation of metal-oxide materials

3.2.1 Fabrication of F-doped SnO₂ (FTO) and co-doped p-type (N, In):SnO₂

Fluorine doped tin oxide films (SnO₂: F) were deposited over coining glass substrates by ultrasonic spray pyrolysis. The precursor solution containing a mixture of SnCl₂·4H₂O (1 mM) and NH₄F (0.5 mM) was dissolved in 500 ml of DI water. To improve solubility of the solution, a 10 ml of HCl was added into the solution and keep stirring vigorously (~30 min) until the solution turns transparent. The product solution was placed to ultrasonic nebulizer reactor, which can produce the aerosol with a controlled-droplet size. The experimental apparatuses consist of specific homemade ultrasonic atomizer, spray gun and graphite hotplate. The deposition parameters such as substrate temperature, spray rate and distance from the spray gun to the substrate were kept constant at the optimized value: 400°C, 20 ml/min and 30 cm, respectively. In addition, different morphologies of textured FTO films can be obtained by applying the carrier gas containing O₂ and N₂ during deposition process at several contents (O₂: 0%, 20%, 50%, 80%, 100%).

For preparation of co-doped p-type (N, In):SnO₂, precursors of In-doped SnO₂ at 0%, 3%, 7%, 15% and 30% were synthesized from SnCl₂·4H₂O and InCl₂·4H₂O dissolved in a mixture of DI water and absolute ethanol (with a volume ratio of 4:1). The mixture was stirred vigorously for 2 hours at 70°C. In order to obtain good solubility, a small amount of HCl was added to the precursor solution. Upon stirring, the solution immediately became transparent, indicating its solubility. Depositions were carried out in an ultrasonic nebulizer reactor at a constant temperature of 400°C to spontaneously form the small grains of the In:SnO₂ film on a Corning glass substrate. After the deposition of the In:SnO₂ layer, the color of the samples changed from white to yellowish, due to the high substrate temperature. Following thermal

annealing at 600°C, the samples were then exposed to nitrogen plasma for 0, 5, 10, 20 and 40 min at 100 mTorr in an inductively coupled plasma (ICP) environment. The ICP power was fixed at 100 W, and the nitrogen gas flow was fixed at 30 sccm.

3.2.2 Fabrication of Al-doped ZnO (AZO) film on FTO

AZO film was deposited on FTO substrate via radio frequency magnetron sputtering system using a commercial AZO target. An unthrottled base pressure of 2×10^{-3} Pa was controlled by a combined vacuum system of mechanical and turbo-molecular pumps under supplying high-purity Ar gas into the main chamber. The deposition temperature was done at 80°C, with annealing process up to 300°C. The sample preparations involve a constant thickness (~ 200 nm) of films depending on the deposition duration (15 min). For the investigation of hydrogen plasma durability, the films were prepared in different geometries for comparison: single layer FTO, AZO and double layer AZO/FTO films, then exposed under hydrogen plasma. Hydrogen plasma was generated by HDP-CVD from H₂ gas with a gas flow of 20 sccm and a pressure of 100 mTorr. Bias voltage was held constantly at 10 V and rf power was 200 W. All of the samples were employed to investigate hydrogen-radical durability of films by varying the plasma duration at 0, 5, 10, 20 and 30 min at 250°C of substrate temperature. In addition, to achieve a reversibility of film properties, the plasma-treated samples were finally post-annealed at 400°C.

3.2.3 Synthesis of ZnO nanorods (NRs), nanowire (NWs) and nanotubes (NTs)

For the hydrothermal reaction, ZnO NRs, NWs or NTs was grown on a ZnO-film-coated glass substrate by immersing in an aqueous mixture of zinc nitrate hexahydrate

[Zn(NO₃)₂·6H₂O] and hexamethylenetetramine (HMT) in deionized water with equimolar (5 mM) ratios of 1:1, 2:1 or 1:1, respectively. Prior to the actual concentration, the incubation of wet-chemical growth was subsequently kept in an electric oven at 75°C (10 hr) for NRs, and 95°C (24 hr) for NWs and NTs. After removal from the aqueous solution, the ZnO products were rinsed several times with deionized water, dried in air, and post-annealed at 300°C. Finally, both ZnO samples were exposed to nitrogen plasma for 60, 180, 300, 480, 600, 720 and 900 s at 100 mTorr in RIE with the RF power fixed at 100 W.

3.2.4 Preparation of O₂ plasma-etched ZnO/FTO heterostructure nanotubes

To explore the potency of our new strategy, we synthesized the highly ordered template-based 1D core/shell structure. The depositing method of FTO film as described earlier was carried out in an ultrasonic nebulizer reactor, of which the temperature was constantly kept at 400°C to spontaneously deposit the small nanoparticles (NPs) on the ZnO NR arrays to form ZnO/FTO composite core-shell heterostructures. After that, the samples were treated by oxygen plasma [P=350 mTorr and radio-frequency (RF) power=350 W] for 0, 2, 10, and 20 min. Consequently, the formation of hollow structure was observed along the [0001] plane in the ZnO inner core through etching mechanism from O-ion bombardment.

3.2.5 Preparation of n-type ZnO/p-type (N, In):SnO₂ core/shell heterojunction diode

Firstly, we manipulated the ultrafine thickness (~10 nm) of the p-type In:SnO₂ shells deposited on n-type ZnO nanorods (~ 200 nm in length) by optimizing the coating time at 3 min and deposition temperature at 400°C. Consequently, the products were composed of crystalline

In:SnO₂ NPs to be well-distributed as a continuous film on the ZnO NR surface with an excellent crystallographic adhesion between two layers. Then, the layer portion of the In:SnO₂-coated ZnO NR arrays was only exposed to nitrogen plasma for 40 min regarding to a diffusion depth of N atoms with the treated In:SnO₂ layer thickness, thereby creating n-type ZnO/p-type (N, In):SnO₂ core/shell heterojunction diodes.

3.3 Characteristics analysis

All studies in this thesis were mainly characterized by means of the structural, electrical and optical techniques. Morphology analysis (i.e. roughness, grain size, and other cross-sectional observations) of the samples was basically done by field emission scanning electron microscope (SEM, JEOL JSM-6700F), high resolution transmission electron microscope (TEM, JEOL 2100), operated at 200 keV, and atomic force microscope (AFM). The crystal structures were determined using XRD diffractometer equipped with a Cu K α radiation source ($\lambda=0.154$ nm) and the diffraction data were collected from $2\theta= 10\sim 70^\circ$. X-ray photoelectron spectroscopy (XPS) was performed using Ar⁺ sputtering at 2 keV with calibration of Pt 1s peak at 70.9 and 74.3 eV, in which survey scans and detail scans of photoelectron emissions were recorded to determine the chemical compositions for each sample. Moreover, depth profiles were obtained using Auger electron spectroscopy (AES) with an etching rate of 2 Å/sec. Secondary ion mass spectroscopy (SIMS) depth profiles revealed the diffusive behavior of hydrogen ions into the films.

For the optical analysis, a UV-VIS double beam spectrophotometer (Model: Evolution 300 BB) was employed to record the optical transmission spectra of the deposited films over the wavelength range of 300-700 nm. To investigate the emission and defect properties of ZnO

nanostructures, photoluminescence (PL) measurements were carried out with a He-Cd laser (365 nm) as the excitation source at room temperature, taken over a wavelength range of 350–800 nm. Photon absorbance was measured by I-T measurement of the UV light source ($\lambda=365$ nm) vertically positioned at 15 cm from the samples, using a model 600C series electrochemical analyzer with an applied direct-current voltage of +5 eV. ON-OFF cycles were consistently repeated upto a 1600-s time trace.

The current-voltage (I-T) characteristics were measured by an electrochemical analyzer (Model 600C series) with an applied DC voltage in the range of ± 1 eV. Furthermore, Hall effect measurement was carried out at room temperature with a Van der Pauw sample configuration (magnetic field: 4000 Gauss, electric current: 0.1 mA), using indium balls as Ohmic electrode, to demonstrate the electrical properties such as carrier concentration (n), resistivity (ρ) and mobility (μ). For device performance, dye-sensitized solar cells (DSSCs) were fabricated using N3 dye, TiO_2 sol, liquid electrolyte, and a Pt counter electrode. Moreover, polymer solar cells were also fabricated in the following manner. A hole-transport layer of poly(3,4-ethylenedioxythiophene)-polystyrene sulfonate (PEDOT:PSS) was spin-cast onto the FTO glass substrate. Above that, the active layer of a mixture of regioregular poly(3-hexylthiophene) (P3HT) and [6, 6]-phenyl-C60-butyric acid methyl ester (PCBM) was prepared with a weight ratio of 1:1. For both types of solar cells, the photovoltaic properties including short-circuit current density (J_{sc}), open-circuit voltage (V_{oc}), and conversion efficiency (η) were measured under AM 1.5 sunlight illumination (Model YSS-80, Yamashita Denso, Japan; intensity: 100 mW/cm^2) from an illuminated area of $0.5 \text{ cm} \times 0.5 \text{ cm}$. Electrochemical impedances of the cells were also measured using the photocurrent-potential-impedance analyzer by applying open circuit voltage as bias in the frequency range of 0.1Hz - 1MHz.

Chapter 4

Effect of Oxygen on the Microstructural Growth and Physical Properties of Transparent Conducting Fluorine-Doped Tin Oxide Thin Films Fabricated by Spray Pyrolysis Method

4.1 Introduction

Transparent conductive oxides (TCOs) have a large market in modern electronics. Due to highly optical transparency and likely metallic conductivity, they were widely used for electrode applications in devices such as thin-film solar cells [105], optoelectronic devices [106], gas sensors [107], frost-resistant surfaces [108], e-windows [109], etc. Recently, fluorine-doped tin oxide (FTO) has been found to be one of most comparable materials with tin-doped indium oxide (ITO). FTO has been attracted much attention as promising alternatives because of its wide energy gap ($E_g = 3.67$ eV), low cost of production, thermal stability, chemical inert, and high transparency, although lower conductivities as compared with ITO obtained hinder its commercial applications.

Up to now, FTO thin film have been extensively prepared by various methods, such as chemical vapour deposition (CVD), metalorganic deposition, rf sputtering, sol-gel, and spray pyrolysis deposition (SPD) [110-113], but considerable efforts have been investigated how to develop a texture surface of FTO conducting electrode, in order to improve performance of solar cell devices by reducing light reflection or making light scattering more efficient. Anisotropic post-etching method using lithographic patterning and etching steps was typically involved to

achieve the desired morphology [89, 90]. However, this might be deleterious to the film properties, difficult to control and increase processing costs. Therefore, this becomes an important issue for developing high surface roughness with self-textured films. Among the various techniques, spray pyrolysis deposition (SPD) is a low-cost process and has been economically conducted to produce FTO films with simply scalable deposition and easy doping process but no systematical investigations are proposed to develop the self-textured FTO film through the SPD process on the basis of the manipulation of substrate temperature, calcinations, gas pressure, and flow rate.

In the present work, we report the effect of oxygen content in the carrier gas on FTO film morphology and optoelectronic properties during the spray pyrolysis deposition. The variation in the growth and nucleation of FTO deposited films is strongly determined by oxygen-incorporated concentration, which causes different surface mobility and oxidation rate of chemical precursors. The significant change in thickness, size and shape of deposited films on glass substrate is reflected in the particular behaviors such as charge transport, recombination, and collection properties due to the surface and interfacial effects, which present variable correlation between optical and electrical properties used for dye-sensitized solar cells (DSSCs) and polymer solar cells.

4.2 Formation and microstructure of FTO texture films

Based on our spray pyrolysis method, different O_2/N_2 concentrations (0%-100%) serve as the carrier gas for depositing the FTO films with different surface morphologies. The grain size, estimated from the top AFM images (Figure 4.1(a)-4.1(e)), is apparently smaller for higher O_2 -

content films. The optimized deposition temperature (constant at 400 °C) and duration (varied by 5-10 min) were used for all film types, in order to form the similar thickness in range of 400-450 nm as indicated in the cross-sectional TEM images (Figure 4.1(f)-4.1(j)). As a result, the surface roughness (RMS) varies in a small range of 22-27 and the thickness was slightly increased being pronounced with higher O₂ concentration. However, two types of growth for FTO films can be classified in two cases: islands-like structure at low O₂ content (0%-20%) and pyramid-like structure at high O₂ content (50%-100%). The side view of TEM images reveals the grain growth mechanism as indicated in the figures. The first type of films may exhibit a strong lateral grain development rather than the grain boundary scattering, therefore the dense and thick films were grown in geometrical directions with round-shaped coverage. On the other hand, in the second type, it is possible that higher oxygen concentration will suppress the lateral growth and individually form cone seeds with apexes. The nucleation site density becomes much higher than the first type due to the effect of low surface energy at higher oxygen concentration. Moreover, the low magnification SEM images in Figure 4.2 (a)-4.2 (b) illustrate the top views of a portion of the large-area FTO films (O₂: 0, 20 and 100%, respectively). An examination of the surface morphology shows how the high-density microstructural grains are homogeneously fabricated in an array over a large area with certain size. The films are very compact but the textural boundaries are clearly visible, in which the result shows a correlation with the AFM and TEM images.

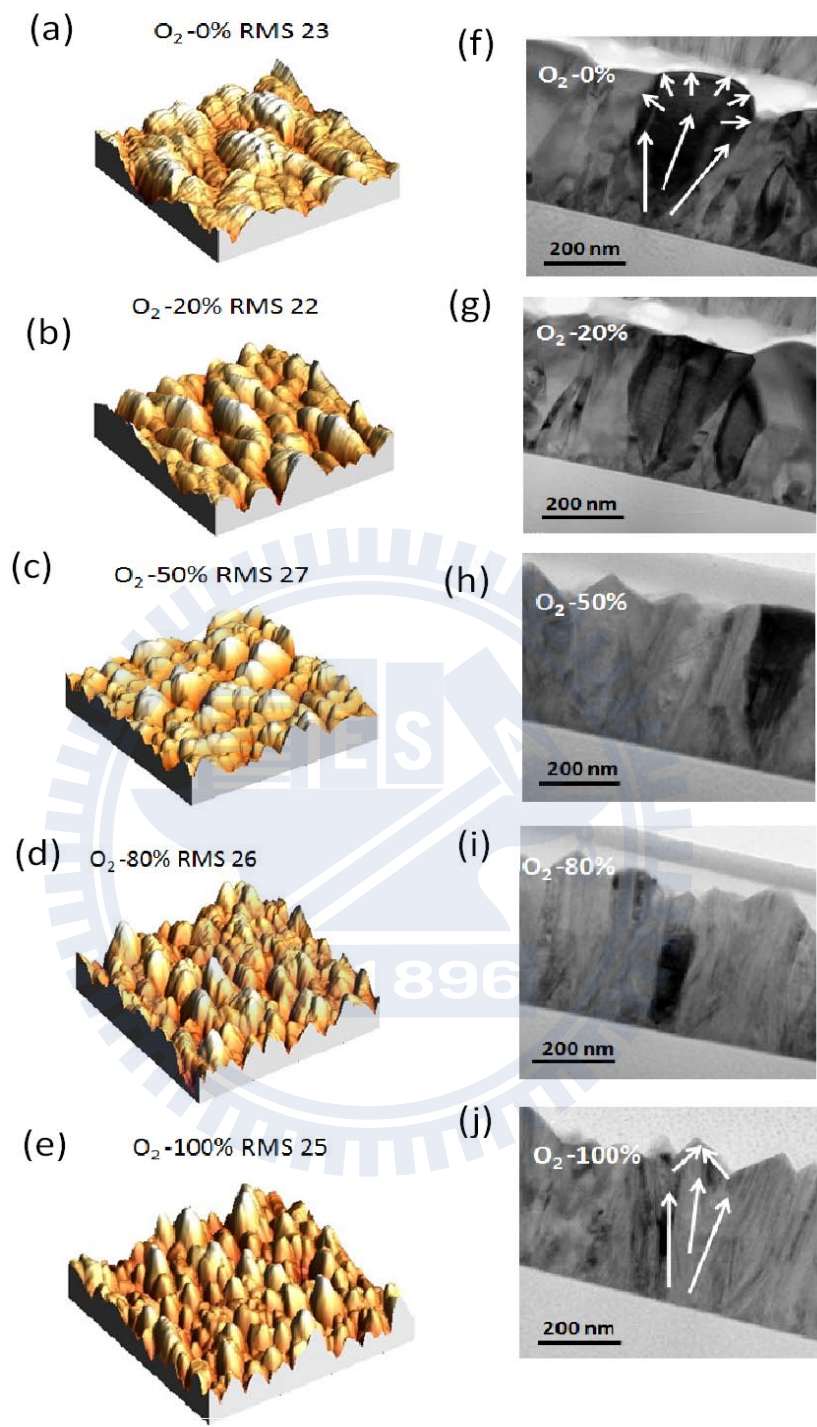


Figure 4.1 (a-e) AFM topographic $5 \times 5 \mu\text{m}$ scans and (f-j) cross-sectional TEM images for oxygen-incorporated FTO films deposited at various oxygen concentrations: 0, 20, 50, 80 and 100%.

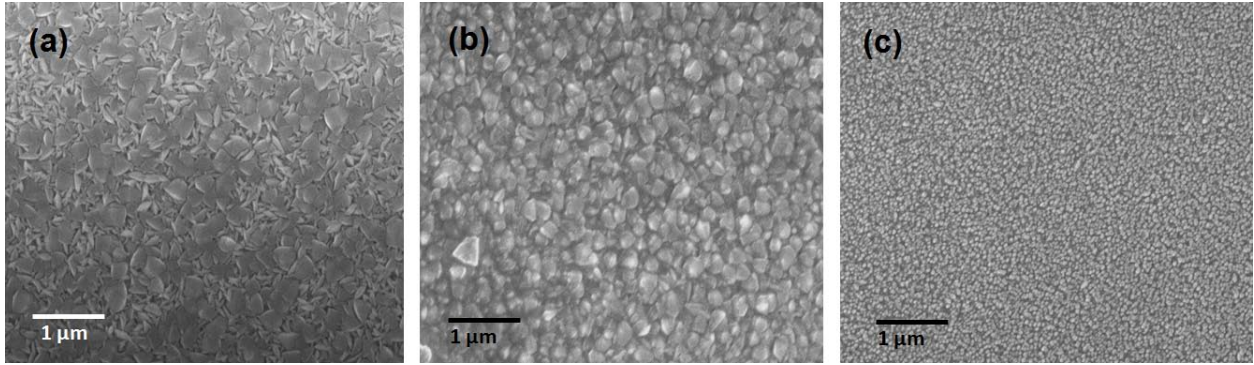


Figure 4.2 FE-SEM images of the deposited FTO films on glass substrate as a function of oxygen content: (a) 0%, (b) 20% and (c) 100%.

According to nucleation theory, the nucleation density (N) can be expressed by the following equation:

$$N = A \exp\left(\frac{-\Delta G}{RT}\right)$$

where ΔG is the activation energy of nucleation, composing of the volume free energy (ΔG_V) and the surface free energy (ΔG_S). R, T, and A are the gas constant, growth temperature, and a constant, respectively. Earlier research explained that the change of the volume free energy decreases as the content of O_2 increases in ambient atmosphere of deposition process. Thus, the activation energy of nucleation becomes lower at O-rich condition, which enhances the surface mobility for the formation of initial layer of FTO film resulting in smoother films and smaller grains [114].

The XRD pattern in Figure 4.3 reveals the evolution of FTO thin films with varied contents of O₂/N₂ carrier gas. All the FTO films are polycrystalline, indicating SnO₂ rutile (tetragonal) structure without additional peaks for SnO or Sn phases. As-deposited FTO film (O₂: 0%) shows the preferential orientation of (110), (200), and (211) at 26.5, 38, and 51.5 degree, respectively. When the oxygen content was added up to higher content, i.e. 80% and 100%, the (200) peak monotonically dominated the patterns, together with decreasing (110) peak. The intensity ratio between (110) and (200) decreases from 1.3 to 0.7 corresponding to a change in the carrier gas from pure nitrogen (O₂: 0%) to pure oxygen (O₂: 100%). In principle, this particular orientation can be influenced by the grain evolutionary selection that follows the concept of periodic bond chain theory [105, 108]: the thermodynamic equilibrium form of SnO₂ structure typically shows a dominant (110) plane of polar faces composing of both tin and oxygen atoms. However, Korotkov et al. reported that the addition of oxygen at high content may enhance the presence of the polar halogen-rich region due to byproduct HCl from the spray pyrolysis process [109], hence; leading to quenching of the [110] growth direction and growth rate saturation. On the other hand, low surface energy at high oxygen content was found that predominate (200) deposition could be induced by the formation of seed layer, which allowed the enhanced nucleation density to change the orientation of above layer with high texture surface, being useful for TCO applications.

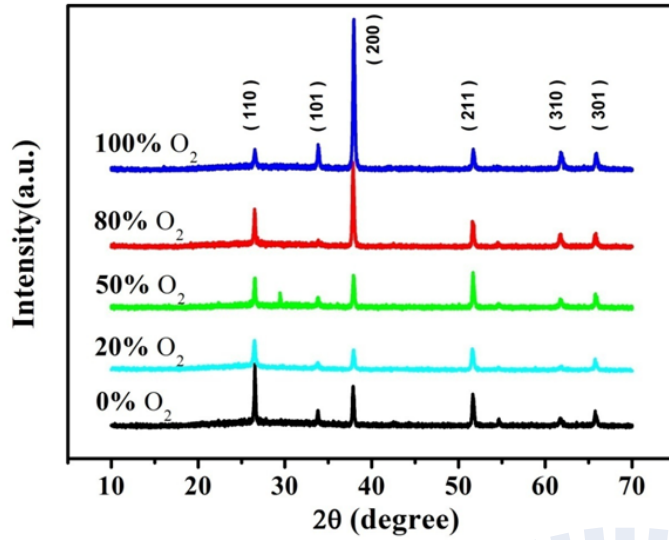


Figure 4.3 X-ray diffraction (XRD) patterns of FTO films deposited on glass substrate with O-incorporated various concentrations.

4.3 Optical and electrical properties

In Figure 4.4, the overall transmission of the films was characterized by UV-Vis measurement. The 100% O₂ sample shows the highest percentage in transmission (96% at the wavelength of 550 nm). Furthermore, the samples with the lower O₂ content at 0%, 20%, 50%, and 80% indicate the lower transmission at 76%, 82%, 86%, and 89%, respectively. The evaluation results can be explained by a correlation of light scattering and reflection depending on size and shape of the grain structures. As shown above, the first result is attributed to an enhanced scattering at the surface and internal layer, and diffraction at structures with sizes close to the wavelength of photon (Figure 4.1). This is due to a smaller and denser grain growth compared with that of lower O₂ content. Note that the theoretical consideration of this behavior is also referred to an increase in waveguide sensitivity. At 80% and 100%, the fluctuation of frequent waves can be clearly observed due to high surface texture, e.g., pyramid-like nanostructure together with large refractive index (*n*). In contrast, a dome-like structure with the flat surface on grains may give rise to a possibility of light reflection, which results in loss of

surface-normal incidence based on Fresnel effect [115, 116]. The desired waveguiding sideways is reduced relatively because the dome with large incident angles seems to act as individual converging lens only redirecting the light into the forward and backward direction, but less internal diffusion.

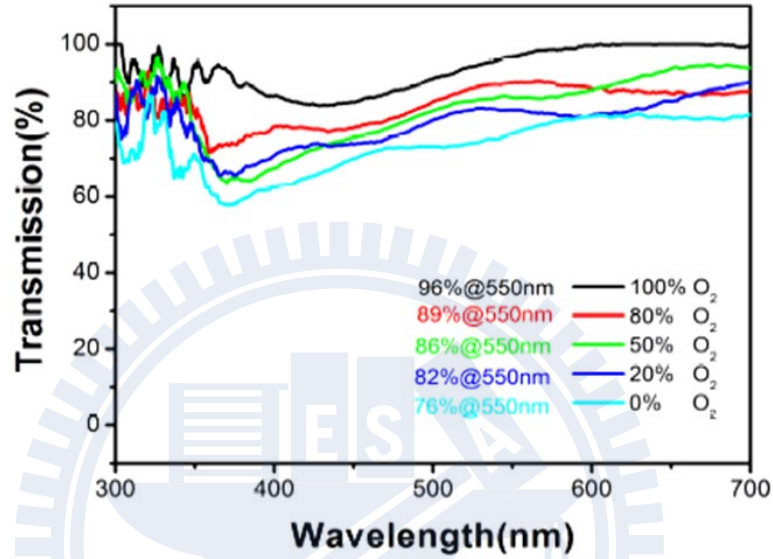


Figure 4.4 Transmission ($T\%$) spectra of FTO films of varying oxygen concentration, deposited on Corning glass.

Figure 4.5 shows the electrical properties of FTO film at room temperature as a function of oxygen contents in carrier gas (0%, 20%, 50%, 80% and 100%) including carrier concentration (n), resistivity (ρ) and Hall mobility (μ). The carrier concentration became higher up to $16.12 \times 10^{20} \text{ cm}^{-3}$ at 50%, and then leveled off for a further increase in oxygen content. In a consistent manner, the values of resistivity rise up to 18 and 70 $\Omega\text{-cm}$ at 80 and 100%, respectively. As the above results, increasing in oxygen content up to 50% is expected to improve the internal oxidization of metallic Sn, which forms a well dispersion of SnO_2 . Instead, at oxygen concentrations above 50%, the excessive oxygen ions (O^{2-}) generated from O_2

molecules at high working temperature ($> 300\text{ }^{\circ}\text{C}$) might predominantly disrupt the stoichiometric FTO film by reducing the amount of intrinsic donor defects (V_{O} and $\text{Sn}_{\text{i}}^{4+}$). Thus, the O^{2-} ion will serve as a compensating acceptor defect to trap free electron and raise the height of potential barrier along grain boundaries, resulting in lower carrier concentration and higher resistivity in the matrix. Additionally, the mobilities were as high as $14.45\text{ cm}^2/\text{V-s}$ at 0% and $16.25\text{ cm}^2/\text{V-s}$ at 20% because the formation of large grain is allowed to develop in denser and smoother surface than others with higher oxygen contents. Thus, the mobility significantly decreased down to $1.17\text{ cm}^2/\text{V-s}$ at 100% where the small-grain size with numerous boundaries between the grains could hinder the intergrain carrier mobility. Due to the increased grain boundary and ionized impurity scattering of the carriers, the electrical properties tend to degrade in a proportion of oxygen concentration.

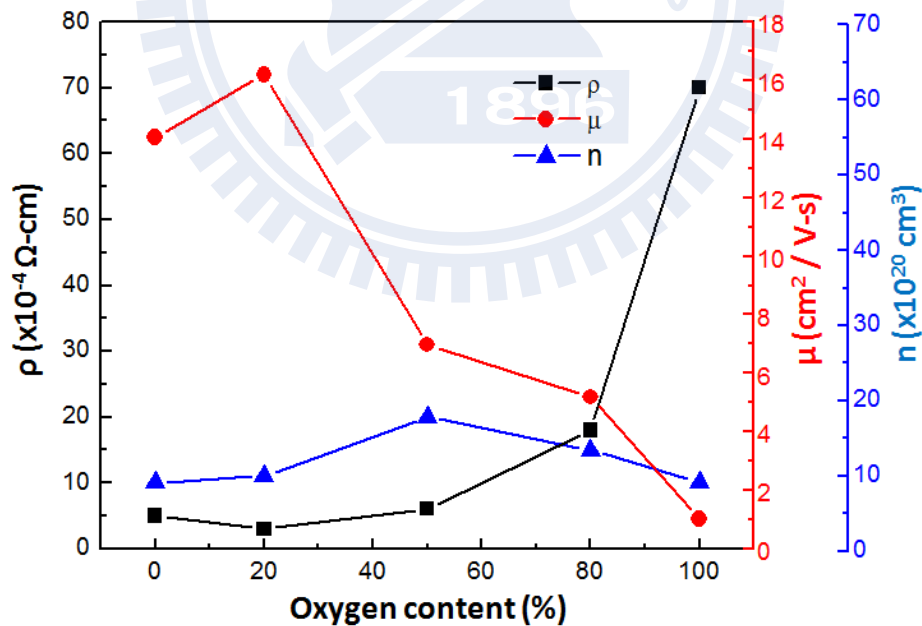


Figure 4.5 FTO film electronic-transport properties: carrier concentration (n), resistivity (ρ), and Hall mobility (μ) as a function of the oxygen concentration (0-100%).

4.4 Performance of photovoltaic devices

Photovoltaic properties of the textured FTO films-based DSSCs with different incorporated O₂ content (0%, 20% and 100%) in the films are summarized in Figure 4.6 and Table 4.1. At 100%, the conversion efficiency (η) is obtained as low as 3.22%, and then it was increased to 3.93% and 4.12% at O₂:20% and O₂:0%, respectively. This is mainly due to the increased short-circuit current density (J_{sc}) from 6.20 to 7.62 and 7.88 mA/cm², respectively, although the open-circuit voltage (V_{oc}) was not changed much (only varied in the range of 0.750-0.761 V). Because V_{oc} strongly depends on the recombination or back-electron transport, the high values within a small variation could be associated with suppressing those effects, resulting in high electron throughput. On the other hand, a large change in J_{sc} is indicated by differences of grain boundaries (spacings) in each case, which can affect electron transport on the FTO film surface (as described by Hall measurement) and the interfacial pathway (contact area) between TiO₂ layer and FTO film. Moreover, the low electrical characteristics (ρ and μ) of 100% O₂ sample, due to an abundant O₂ incorporation, were assumed to dominate the performance of DSSCs, although the film showed a highest transmission in UV-Vis (Figure 4.4).

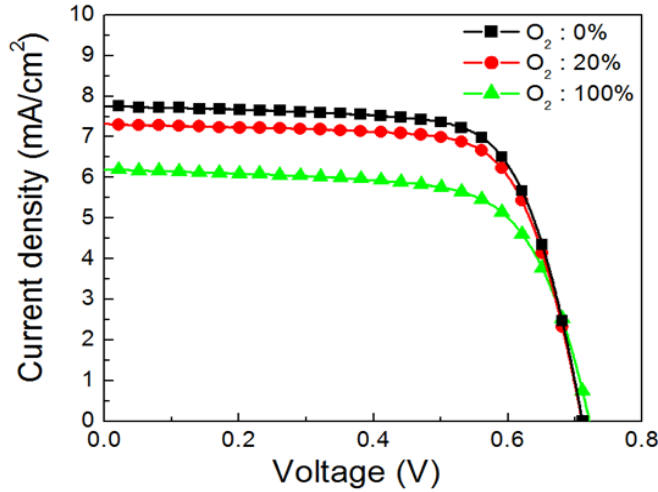


Table 4.1 Summary of FTO film properties used in DSSCs.

O ₂ -content	V _{oc} (V)	J _{sc} (mA/cm ²)	FF	η (%)
0%	0.756	7.88	0.692	4.12
20%	0.750	7.62	0.688	3.93
100%	0.761	6.20	0.682	3.22

Figure 4.6 J-V characteristics of FTO film-based DSSCs. The illumination intensity of 100 mW cm⁻² with AM 1.5 and active area of 0.25 cm² were applied.

Due to the grain boundary effect as mentioned above, we further examined the correlation between the cell performance and the internal resistance of the DSSCs via electrochemical impedance spectroscopy (EIS) measured at V_{oc} under 1.5 AM (Figure 4.7). Regarding to a significant difference in surface morphology (grain growth), the 0%, 20% and 100% O₂ samples were used to elucidate the behavior of the electron interception and the electron diffusion to the collecting anode. The Nyquist plots of the samples exhibited four impedance components of a DSSC including: the resistance element (R_h) of the FTO layer in the high frequency region (> 10⁶ Hz) and the other three impedance element Z₁ (ω₁: 10³-10⁵ Hz), Z₂ (ω₂: 1-10³ Hz), and Z₃ (ω₂: 0.1-1 Hz) associated with charge transfer processes at the counter electrode, the interface among the FTO/TiO₂/dye/electrolyte, and the Nernstian diffusion within the electrolyte, respectively. A specific feature in the arc of Z₂ of 100% O₂ sample increases by 11.5 Ω in width compared to those of 0% and 20%, which is attributed to the electrochemical

interfacial resistance between the FTO and the TiO₂ working electrode. Simultaneously, the R_h of 100% O₂ sample also increases by 6 Ω, showing a good agreement with the electrical properties of Hall measurement in Figure 4.4, while the other values (Z₁ and Z₃) remain almost identical.

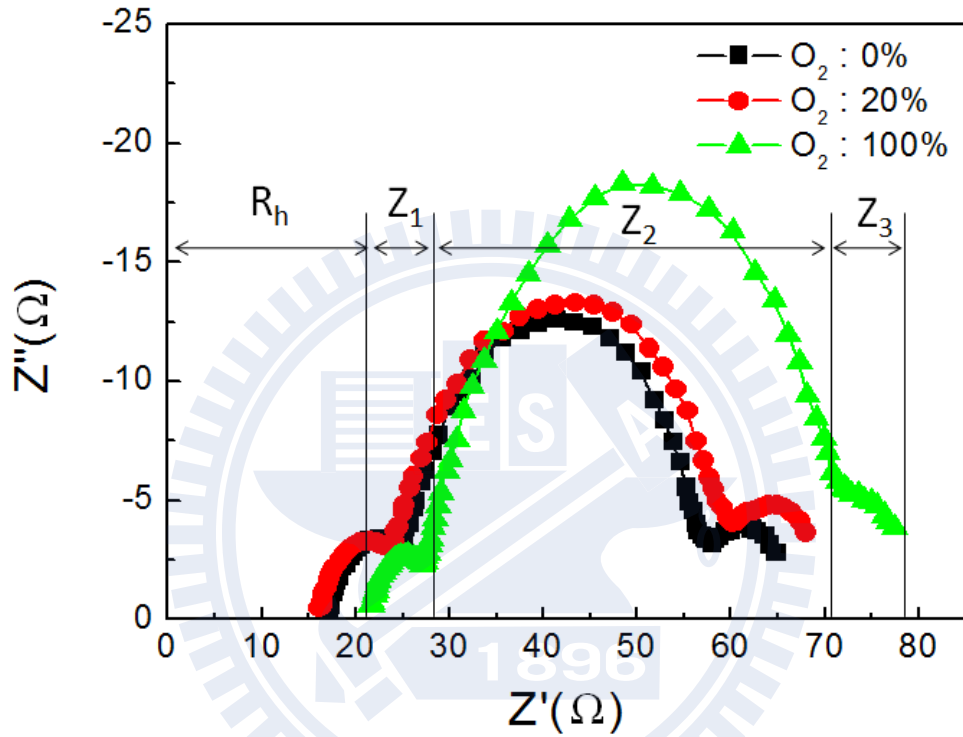
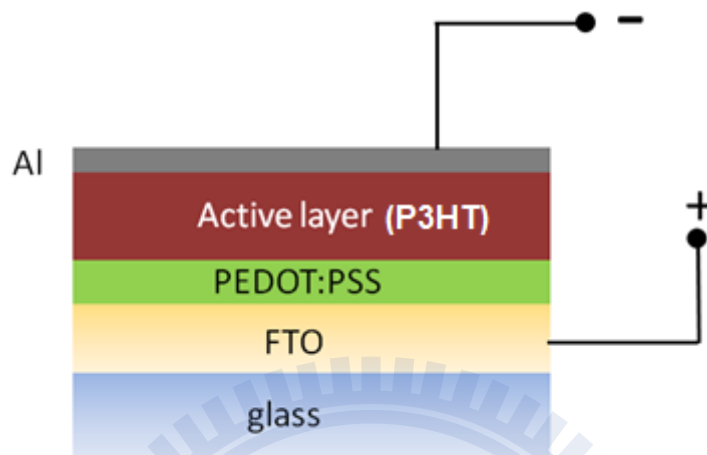


Figure 4.7 Representative Nyquist plot of the electrical impedance spectra of the FTO films measured in the frequency range of 0.1Hz – 1MHz under AM 1.5.

Furthermore, we also applied the deposited FTO films (O₂: 0%, 20% and 100%) to integrate the polymer solar devices (Scheme 4.1) which can be comparable to the DSSCs in the previous section. Nevertheless, by spin-casting a hole transport layer of poly(3, 4-ethylenedioxythiophene)-polystyrene sulfonate (PEDOT:PSS) onto the FTO electrodes,

following by annealing treatment (120 °C), a thin continuous contact is expected to be formed at the interface as a result of the low melting point of PEDOT:PSS film.



Scheme 4.1 Schematic cross section of polymer solar cells deposited on an FTO-coated glass substrate, using an oblique electron-beam evaporation method.

In Figure 4.8, the conversion efficiency of 100% O₂ sample (3.13%) is apparently larger than those of 0% and 20% O₂ samples (1.85% and 1.89%, respectively). Indeed, the results show the opposite way from the DSSC devices, especially; the performance of 100% O₂ sample is significantly improved from DSSCs. Table 4.2 shows an abrupt increasing in the current density (J_{sc}) and the open-circuit voltage (V_{oc}) of 100% O₂ samples from the other two, which is due to the polymer highly suppressing the abundant channels between the grains. The width of depletion region and Schottky barrier becomes narrower. Thus, holes are more efficiently collected by the embedded nanoelectrodes (pyramid-like structure) than the flat-grain type; meanwhile, the electrons can be easily generated and injected from the active layer to FTO, giving rise to higher conversion efficiency by ~40%. Overall, the improved photovoltaic

performance of 100% O₂ FTO-based polymer solar cells can be explained that successfully originates from (1) their superior interface modification between highly textured FTO and polymer layer, leading to a decrease in charge recombination and (2) high transmittance with improved light absorption compared to the planar surface of large grain samples.

Somehow, due to the reason that high oxygen gas flow or even surrounding atmosphere applied at high deposition temperature serves as an oxidation annealing process, it may result in oxygen-annihilated oxygen vacancies, thereby deteriorating the electrical conductivity of FTO film. Therefore, this could be the way to further improve the cells performance as comparable with the standard DSSCs or polymer solar cells; fabrication of surface roughness architectures will develop an optimization between electrical (more efficient charge transport) and optical (enhanced light harvesting) properties to increase the conversion efficiency of textured FTO-based DCCSs.

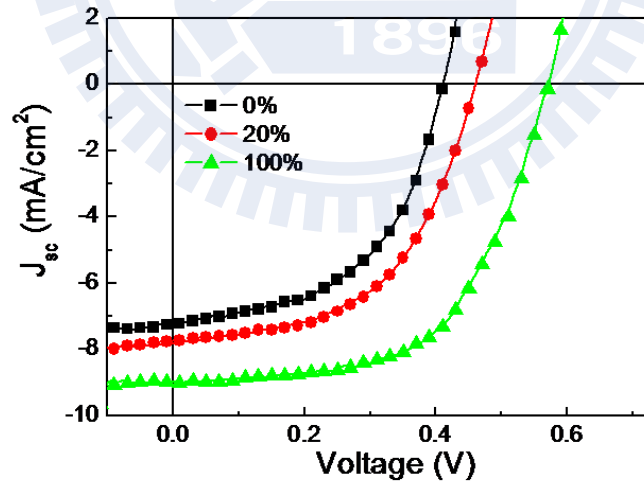


Figure 4.8 Trace of current density against voltage (J - V) for three cells with 0%, 20% and 100% O₂/N₂ concentrations.

Table 4.2 Summary of photoelectric conversion efficiencies for a selection of polymer solar cells.

O₂-content	V_{oc} (V)	J_{sc} (mA/cm²)	FF	Efficiency (%)
0%	0.41	7.38	0.61	1.85
20%	0.46	7.9	0.52	1.89
100%	0.57	9.03	0.61	3.13

4.5 Summary

In summary, fluorine-doped tin oxide (FTO) electrodes have been investigated as an alternative anode to indium tin oxide (ITO) in dye-sensitized (DSSCs) and polymer photovoltaic devices. FTO films were grown by ultrasonic spray pyrolysis deposition on Corning glass substrate at 400°C, using O₂/N₂ deposition concentrations at 0, 20, 50, 80 and 100%. The structural, electrical and optical properties of the FTO texture films were studied as an effect of surface morphology. A significant reduction in grain size was found to depend strongly on the increased oxygen concentration, in which the films showed higher resistivity (ρ) and transmittance (T%). For the photovoltaic performance, the FTO film-based DSSCs with 0% O₂ showed higher conversion efficiency (4.22%) compared with 100% O₂ (3.12%), which the numerous grain boundaries and pyramid-grown structure made a large contribution to the degradation of electron transport (diffusion length). In contrast, the polymer solar cells, based on PEDOT:PSS layer spin-casted on the FTO electrode, improved the interfacial contacts between grain boundaries. The results showed the opposite trend that the efficiency of 100% O₂ sample was much more enhanced (3.13%) than that of 0% O₂ (1.85%) because of the necking of grain boundaries, higher transmission (T=96%), and the possibly reduced charge recombination by larger surface area.

Chapter 5

Mechanism of a AZO-coated FTO Film in Improving the Hydrogen Plasma Durability of Transparent Conducting Oxide Thin Film for Amorphous-Silicon Based Tandem Solar Cells

5.1 Introduction

Hydrogenated amorphous silicon (a-Si:H) solar cells have generated intense interest as an alternative to crystalline silicon cells because of the low cost of the preparation procedure. They provide the function of light absorption and charge-carrier transport that takes place in the transition of a multijunction p-i-n diode [94, 117] (interface region) sandwiched between the transparent conductive oxide (TCO) layer and the back contact layer. In general, amorphous silicon thin films can be grown by plasma-enhanced chemical vapor deposition (PECVD), by exposing the sample to silane plasma containing hydrogen radicals and ions. Therefore, one of the key problems is an enhanced reduction of tin oxide (FTO or ITO) in the TCO layer due to the generation of H atoms on interstitial (H_i) and substitutional (H_o) defect sites. Once a certain incorporation of defects is achieved, a significant degradation in the electrical, optical and even structural properties is observed in a number of studies [93, 118, 119].

In addition, another class of transparent-conducting materials including Al-doped ZnO, has also received much attention not only for its excellent electronic and optical properties comparable with FTO or ITO but also for its high durability under exposure to thermal annealing

and H-plasma treatment [45, 120-123]. However, AZO films deposited by sputter deposition tend to display a flattened surface, which causes lower haze values. Therefore, from an architectural point of view, the textured FTO film is generally fabricated by high temperature deposition with various methods in which a controllable morphology of film growth is employed to enhance the light scattering and haze ratio for the TCO electrode [124-126].

A number of fabrication strategies have been successfully utilized to generate a double-layer TCO electrode [101, 102]. However, these reports mainly examined the effect of the successive preservation of the FTO film by an alternative protection layer. For example, coating the a-Si₃N₄:H barrier layer on top of the SnO₂ layers was proposed to reduce the diffusion of decomposed Sn atoms into p-type a-Si_{1-x}C_x:H (x=0.28), and an XPS spectra revealed the formation of chemical bonds between Sn and other elements such as Si, C and N according to the diffusion mechanism of Sn [117]. Recently, to overcome disadvantages such as low conductivity, transparency and durability of coated films, a double-layer TCO film composed of binary compound oxides (In-doped ZnO/F-doped SnO₂) has been utilized as a transparent electrode for a-Si:H solar cells [121]. Unfortunately, the production of In-doped ZnO films requires high temperatures (>375 °C) in order to deposit a rough and thick layer on FTO glass, which degrades the original FTO properties. Accordingly, the interfacial effect of epitaxially grown films should be another important factor that controls the atomic diffusion behavior. Also, attempts to further understand and examine the properties of this structure under H-plasma treatment and thermal annealing effect have not yet been undertaken.

Therefore, we propose a double-layer TCO electrode that involves an additional barrier layer of AZO above the FTO layer. In this configuration, the original morphology of FTO remains, while the deterioration of FTO film properties might be reduced even in the presence of

a plasma atmosphere containing hydrogen radicals and ions. Moreover, we also investigated the diffusion of incorporated hydrogen in the double layer AZO/FTO films via a change in the chemical composition and a reversal of deterioration, by performing a post annealing treatment (at a higher temperature than observed during the plasma treatment) following the plasma process. A comparison between the results of as-deposited, plasma-treated and post-annealed samples for a variety of single and double layer films provides an improved understanding of the surface and bulk characterization, as determined by the analysis of the structural, electrical and optical properties. Presumably, the investigation of this reproducible double TCO films could lead to a significant development in the generation of efficient a-Si:H solar cell devices.

5.2 Surface morphology and structural properties of single-layered FTO films and double-layered AZO/FTO films

Figure 5.1 shows the SEM images of a single-layered FTO film and a double-layered AZO-coated FTO film under H-plasma treatment of various durations (0-30 min). As shown in Figure 5.1(a-c), the FTO film has a grain size in the range of 50-150 nm. After H-plasma treatment for 5 min, the surface morphology begins to produce little white particles because of the disintegration of original FTO. With increasing H-treated time up to 30 min, the white area becomes more apparent and forms larger stacks (approximately 300 nm in grain size) that are assumed to be integrated from ultrafine Sn nanoparticles up from the surface of the film. In Figure 5.1(d-f), the morphology of deposited AZO layers has a granular surface coverage on top of the FTO surface. The size of fine AZO particles, formed on the crystalline FTO surface due to secondary nucleation, was measured to be approximately 10-20 nm. Along with increasing

plasma duration, the AZO/FTO is able to retain its original morphology because of the protection of a barrier AZO layer.

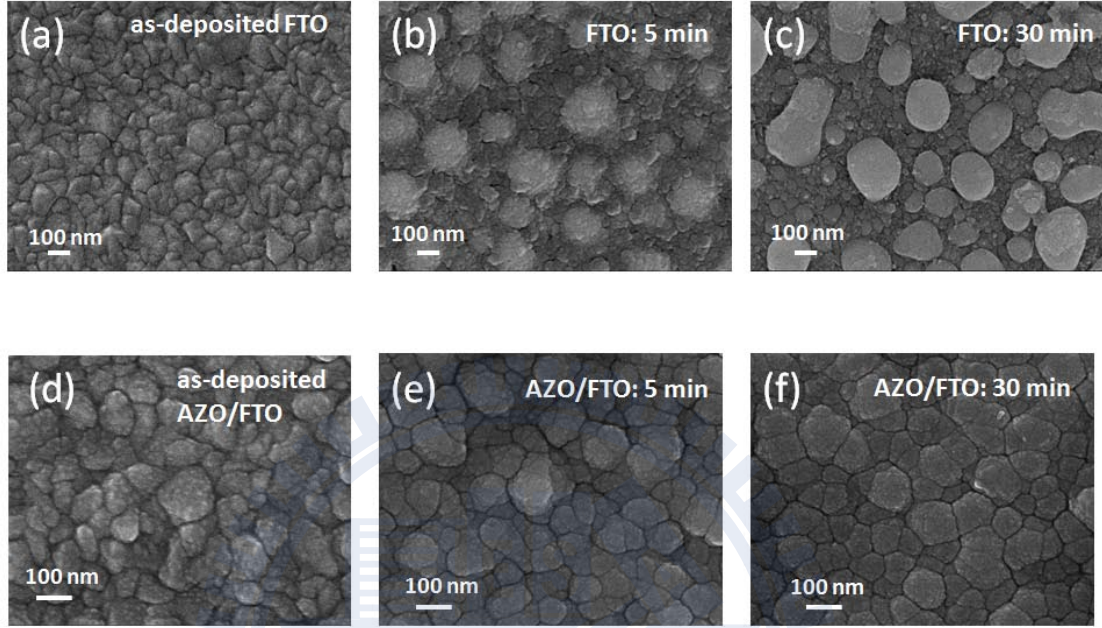


Figure 5.1 Plain-view SEM images of the textured FTO films and the AZO/FTO films (a and d) without H_2 plasma treatment, or with H_2 plasma treatment for (b and e) 5 min , and (c and f) 30 min.

Figure 5.2 shows the XRD pattern for FTO, AZO and AZO/FTO films before and after the plasma process. The spectrum of the FTO film contains the existence of (110), (101), (200), (211), (310) and (301) transitions, corresponding primarily to SnO_2 polycrystalline planes, whereas the AZO film has a single peak dominated by the (002) orientation of crystalline ZnO. Moreover, the combination AZO/FTO double layer film also shows the crystallites of the two metal-oxide compounds. Following the post H-plasma heat treatment at $250^\circ C$, there are no additional diffraction peaks that belong to other nonrelative compositions in the treated films as compared with the as-deposited films; this result indicates that H^+ ion bombardment and thermal

effect seem not to distort the crystallinity of the lattice structure. In addition, the XRD results are also consistent with the cross-sectional TEM analysis of AZO/FTO samples under plasma treatment as shown in Figure 5.3(a). The result reveals that the FTO film has a columnar growth of pyramidal shapes with a thickness of 245 nm, which is covered by the AZO layer with a thickness of 120 nm. Note that the AZO/FTO sample was also coated with Pt to facilitate the preparation of cross-sectional TEM samples using the Focused ion beam (FIB) method.

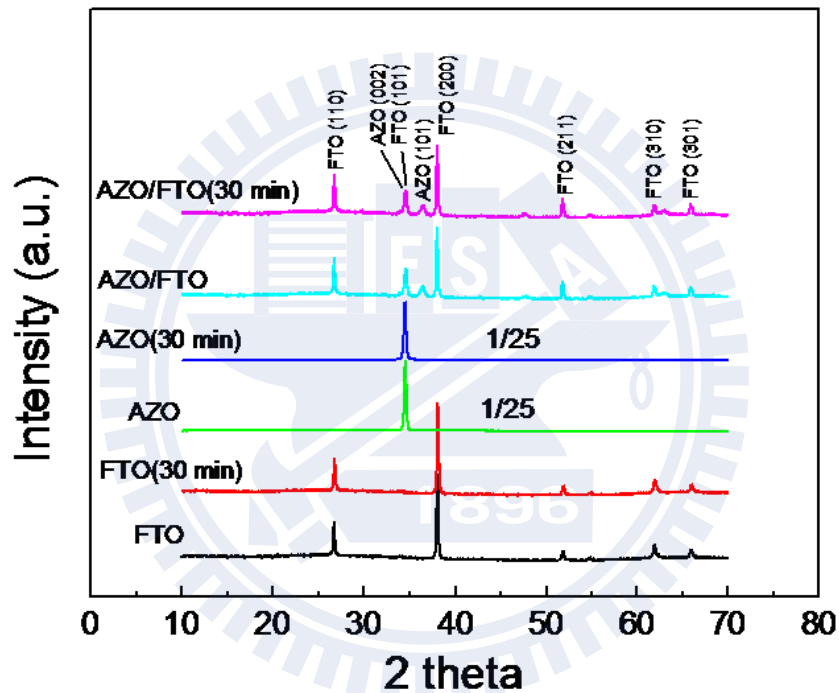


Figure 5.2 X-ray diffraction pattern of the FTO, AZO, and AZO/FTO samples before and after H_2 plasma treatment for 30 min as identified at each spectrum.

A thin continuous AZO layer was formed as a result of the low surface energy of FTO, and could completely bridge the gap at the interface. Both FTO and AZO layers exhibit clear lattice fringes that separate each other from the atomically sharp interface, indicating the

epitaxial growth of the AZO layer. Therefore, even though the samples were exposed by plasma for 30 min, Figure 5.3(b) clearly demonstrates that the lattice fringes of individual pyramids in each FTO grain could remain crystallographically aligned along the same direction [200] with respect to the preferential orientation. The spacing between two adjacent lattice planes remains constant at 0.267 nm, which is consistent with the (100) plane of rutile SnO₂.

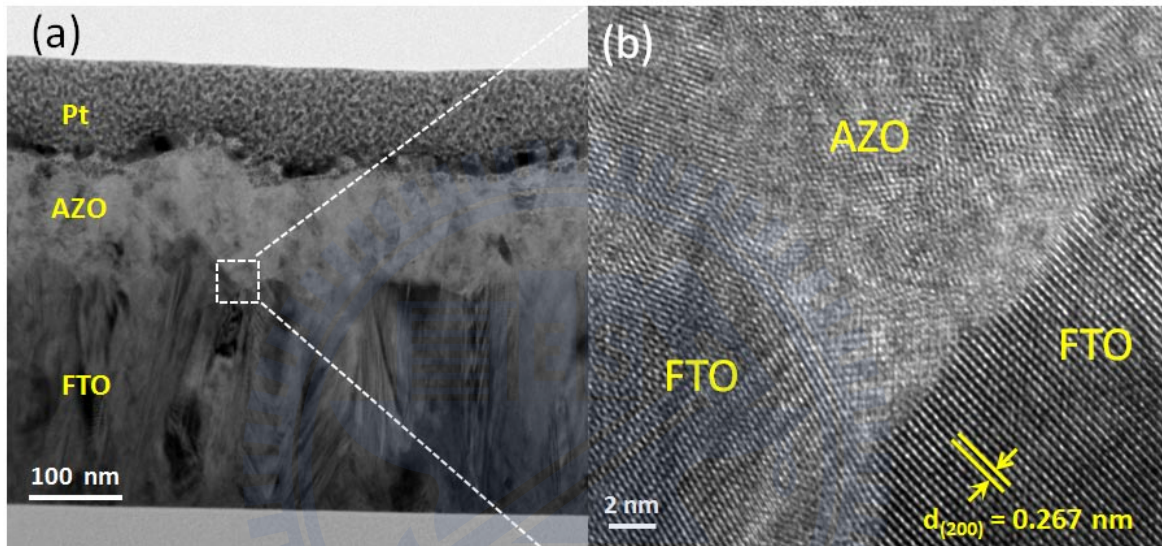


Figure 5.3 (a) Cross-sectional TEM image of a double AZO/FTO film coated by a thin Pt conductive layer. (b) High-magnification TEM image taken from the region, marked by a square in (a).

5.3 Evolution of transparent conducting films under H-plasma treatment

The dependence of the Hall measurements, that is, the carrier concentration (n), Hall mobility (μ) and sheet resistance (R_s), on the length of H-plasma treatment are illustrated in Figures 5.4(a), 5.4(b) and 5.4(c), respectively. For FTO samples, the carrier concentration

decreased from a maximum of 6.61×10^{20} to $5.36 \times 10^{20} \text{ cm}^{-3}$ after 30 min, which can be explained because H radicals eliminate oxygen vacancies ($V_o^{\bullet\bullet}$) during plasma treatment. In other words, the mobility gradually increased from 12.83 to $16.52 \text{ cm}^2/\text{V}\cdot\text{s}$ after plasma treatment of up to 20 min. The trend is inversely proportional to the lower carrier concentration as a consequence of a decrease in the electron scattering centers. However, the mobility decreased to $12.35 \text{ cm}^2/\text{V}\cdot\text{s}$ when the treated time was increased to 30 min. As a result, surface scattering may occur from the grain boundary effect because a large number of H radicals is likely to be dispersed at grain boundaries or around the FTO particles. Thus, the formation of accumulated stacks on the surface, as shown earlier in the SEM image (Figure 5.1(c)), can hinder the charge transport across boundaries. In principle, this implies that the characteristics of the mean free path of the carriers must be changed by an increase in the potential-well barrier at the depleted region. A decrease in carrier concentration induced by H atom filling a portion of the $V_o^{\bullet\bullet}$ can elucidate a weak durability of FTO film and is also in good agreement with the 2-fold increase in sheet resistance after the plasma treatment, as shown in Figure 5.4(c).

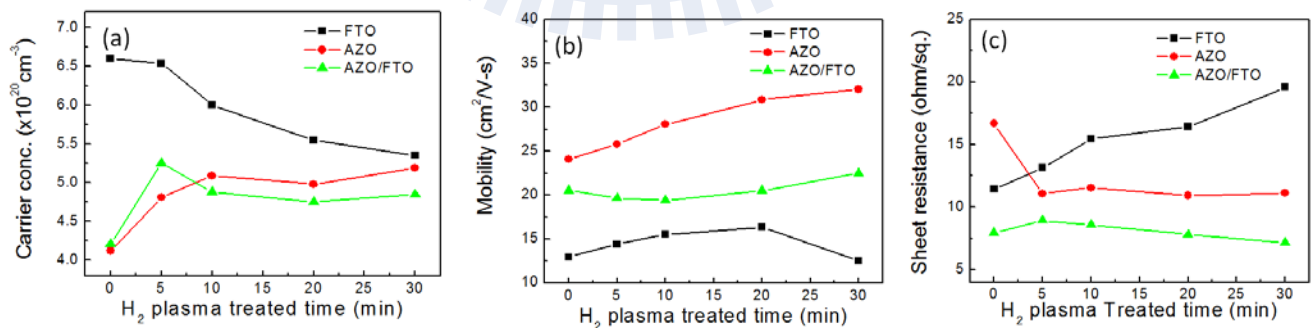


Figure 5.4 Dependence of (a) carrier concentration, (b) Hall mobility, and (c) sheet resistance on H₂ plasma treated time for the deposited FTO, AZO, and AZO/FTO films.

However, both the carrier concentration and mobility of the AZO film increase with increasing plasma duration, although they remain constant after a certain amount of treatment time, due to an H-absorbed saturation. Interestingly, a dramatic reduction in the sheet resistance was observed after 5 min (from 16.78 to 11.05 ohm/sq.), which was dependent on the variation in the carrier concentration, as shown in Figure 5.4(a). Indeed, this result indicates that the plasma-enhanced conductivity is due to surface-related electron transport rather than a bulk effect. Hydrogen plasma allows for the chemisorption of H ion impurities on the surface so that interstitial H atoms with small migration energy can subsequently form the hydroxyl OH groups with the nearest-neighbor O atom, which acts as a shallow donor in ZnO [120, 123]. Furthermore, after longer plasma treatments, the H atoms are expected to diffuse toward deeper levels through the hopping process associated with the rebinding of the second-neighbor O atom and so on. Indeed, the donor concentration, as well as the generation of free electrons, becomes enhanced, leading to improved conductivity of H-incorporated AZO film relative to the untreated one.

In the double layer AZO/FTO film, the mobility was slightly varied as a function of the plasma treatment time, while the other electrical characteristics (n and R_s) are improved after a 5 min treatment. The results can be explained in the following manner: (1) Because the Hall Effect is considered a surface-related measurement, the enhanced electrical properties of the entire AZO/FTO film are mainly due to the high conductivity of the AZO film layer. (2) Meanwhile, some degradation may also occur when the H-plasma treatment exceeds a given amount of time (10-30 min), which induces the diffusion of hydrogen toward a deeper level and its accumulation at the interfacial layer between AZO and FTO films. The partial H^+ ions presumably disintegrate SnO_2 of the uppermost crystalline FTO film, resulting in a surface desorption of the metallic Sn.

Subsequently, a depletion of an ultrafine-thin layer occurs from the migration of structure defects (misfit dislocations) to a region of a lower diffusion coefficient at the bottom of the AZO layer [94]. Nevertheless, the examination of the AZO layer has been proven to mostly prevent the H atoms from annihilating a portion of the FTO layer, which can preserve the contact properties by limiting the metallic interdiffusion and the accumulation of impurities. On the basis of the above statements, it is implied that the slight variation in properties could be attributed to the compensation between phenomena (1) and (2) in the equilibrium state.

In the presence of H-plasma, the FTO samples in Figure 5.5(a) exhibit a change in the UV-Vis spectra, wherein the optical transmission is gradually diminished from 99.6 to 31.6% at the wavelength of 550 nm, as the duration of plasma treatment increases to 30 min. The combination of the structural and optical data shows that the FTO films were deteriorated by H-incorporated radicals because of the reduction of SnO₂ to metallic Sn and sub-oxide of Sn (SnO). Because both excess Sn and SnO may create crystal disorder and trap electron carriers, the reduction of the optical band gap is expected by moving the valence band (VB) up and conduction band (CB) down. The dominating intrinsic defects (Sn_i and V_o) in SnO₂ are compensated by the presence of metallic Sn and SnO, which lowers carrier density and which results in a decrease in the refractive index (n) [124]. Moreover, the absorption edge shifts toward a longer wavelength (or lower energy) for all H-treated samples in Figure 5.5(a), corresponding to the quantum size effect; hence, this behavior indicates an enlargement in the grain size due to surface roughness, as shown in Figure 5.1(c). According to above reasons, the formation of the SnO texture has a remarkable effect of inducing higher light scattering and optical trapping in the film.

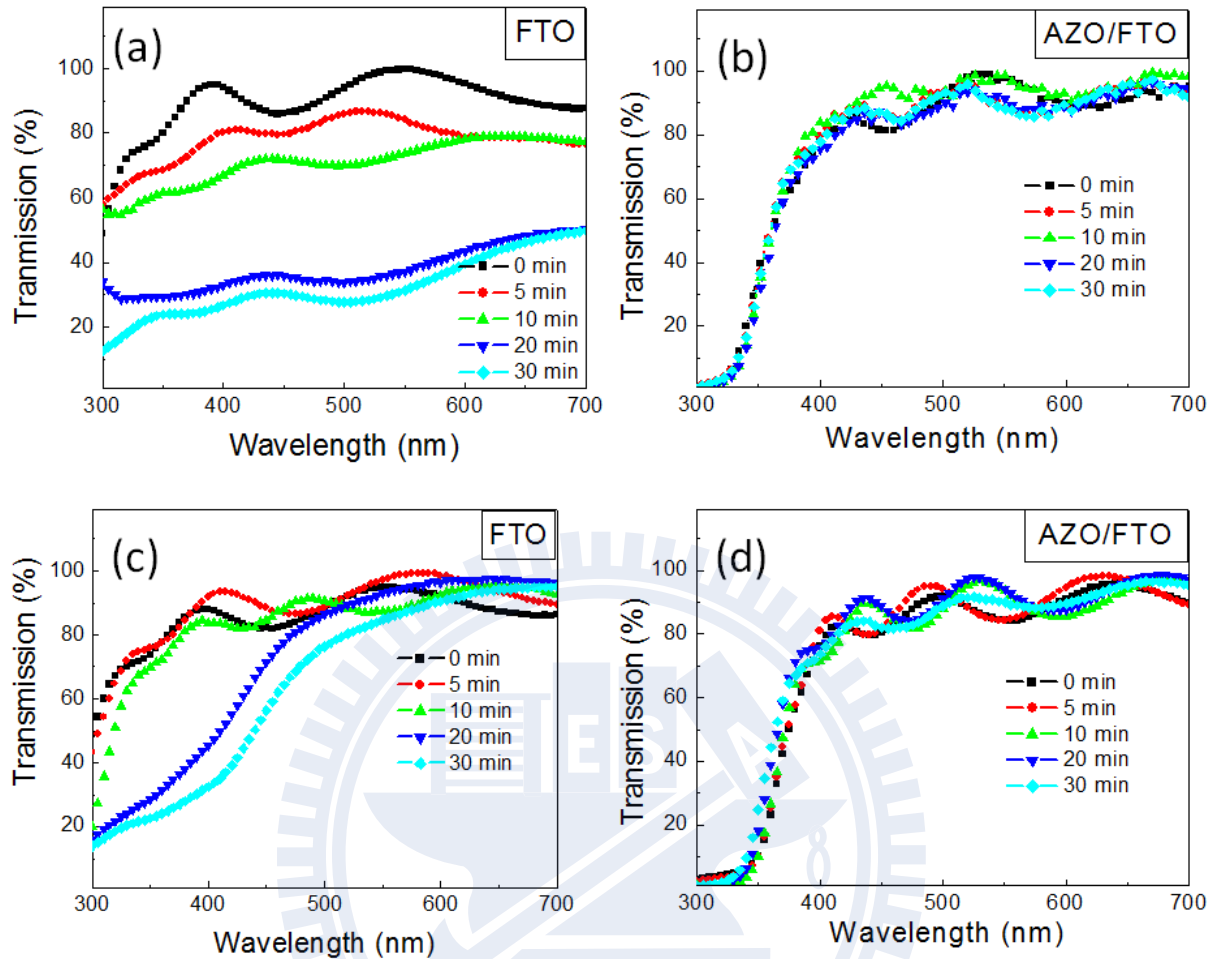


Figure 5.5 The effect of (a and b) H_2 plasma treatment at 0, 5, 10, 20 and 30 min, and (c and d) post annealing treatment at $400^\circ C$ on the optical transmission for the FTO and AZO/FTO films.

However, the transmittance of the deposited AZO/FTO samples in Figure 5.5(b) did not show any dependence on the H^+ ion energy with increasing exposure times. All of the samples show the average transmission of more than 80% in the spectral range of 400-700 nm, although a slight shift in the absorption peaks is observed because of the addition of H-related point defects such as Zn interstitial (Zn_i) and oxygen vacancy (V_o). Theoretically, this is because the H-

incorporated atoms containing H_i and H_o are coordinated at interstitial (lying in a Zn-O bond-centered position) and substitutional O sites, respectively. It is noted that only H_i , with its high mobility and low formation energy, rather than H_o , can easily migrate from the original position to the preferential position and that it is likely to form a O-H bond with the nearest-neighboring O atoms. Thus, there will not be substitution of H atoms at O sites (H_o) in ZnO leading to a dissociation or reformation of Zn-O bonds, unless the formation energy is high enough to overcome the oxygen chemical potential (μ_o).

Furthermore, to examine whether the heat could indeed recover the optoelectronic properties of plasma-treated films, all samples were then placed in an oven at 400 °C for 1 h. During the thermal treatment, the heat flow is expected to be isotropic to expel the diffusion of H atoms either upward or downward in the film interlayer, which is suitable for understanding the reversible thermal mechanism. Figures 5.5(c) and 5.5(d) show the optical transmission after the post annealing process for FTO and AZO/FTO films, respectively. Clearly, there is an increase in the transmission in Figure 5.5(c) back to the original value (as-deposited FTO). As a result, the 5- and 10-min plasma treated samples show nearly a complete recovery, which is not the case for samples treated for 20 and 30 min. Although a particular H_o is stable enough to occupy the O sites, the annealing treatment at 400 °C is high enough to break a multicenter bond of Sn-H and to release the unbound Sn. The thermal treatment suggests that at short H-plasma treatment durations (5 and 10 min), the H^+ ions are able to escape from the film, while the Sn is reoxidized to form the SnO_2 phase as a result of the appropriated annealing conditions. However, longer treatment times (20 and 30 min) might affect other physical properties by permanently changing the surface morphology of the FTO films. Thus, the severely damaged film containing a large amount of suboxide SnO will not result in the recovery of optical transmission.

5.4 Diffusion mechanism of hydrogen-incorporated atoms

Figure 5.6 displays the concentration profiles of several elements including Sn, O, F, and H as a function of the depth for both a single FTO and double AZO/FTO film deposited on the Corning glass substrate. The normalized intensity shows the variations in concentration with respect to the Cs^+ ion etching depth (nm), for the plasma-treated samples (S2) and the post-annealed samples (S3). One region in the single FTO film (225 nm) is clearly identified in Figure 5.6(a-b), while the AZO-coated FTO film contains two main regions (440 nm) with a constituent interfacial region, as shown in Figure 5.6(c-d). It should be noted that neither Zn nor Al signals were shown in this profile because only H-effected elements with high intensity are assigned to interpret the relative changes in chemical compositions. In Figure 5.6(a), the severe damage due to H-ion incorporation (S2) may cause a lower intensity of Sn and O signals at the near-surface region (<75 nm in depth) than in the in-depth region, because of the presence of metallic Sn or SnO, which mainly causes the surface roughness mentioned earlier. Then, after the annealing process (S3), Sn and O signal intensities change significantly to nearly a constant value, demonstrating the reoxidization and recovery of the film. Meanwhile, the amount of both H and F ions was noticeably reduced because of the effect of thermal-enhanced diffusion, especially at the surface and the bottom of the film.

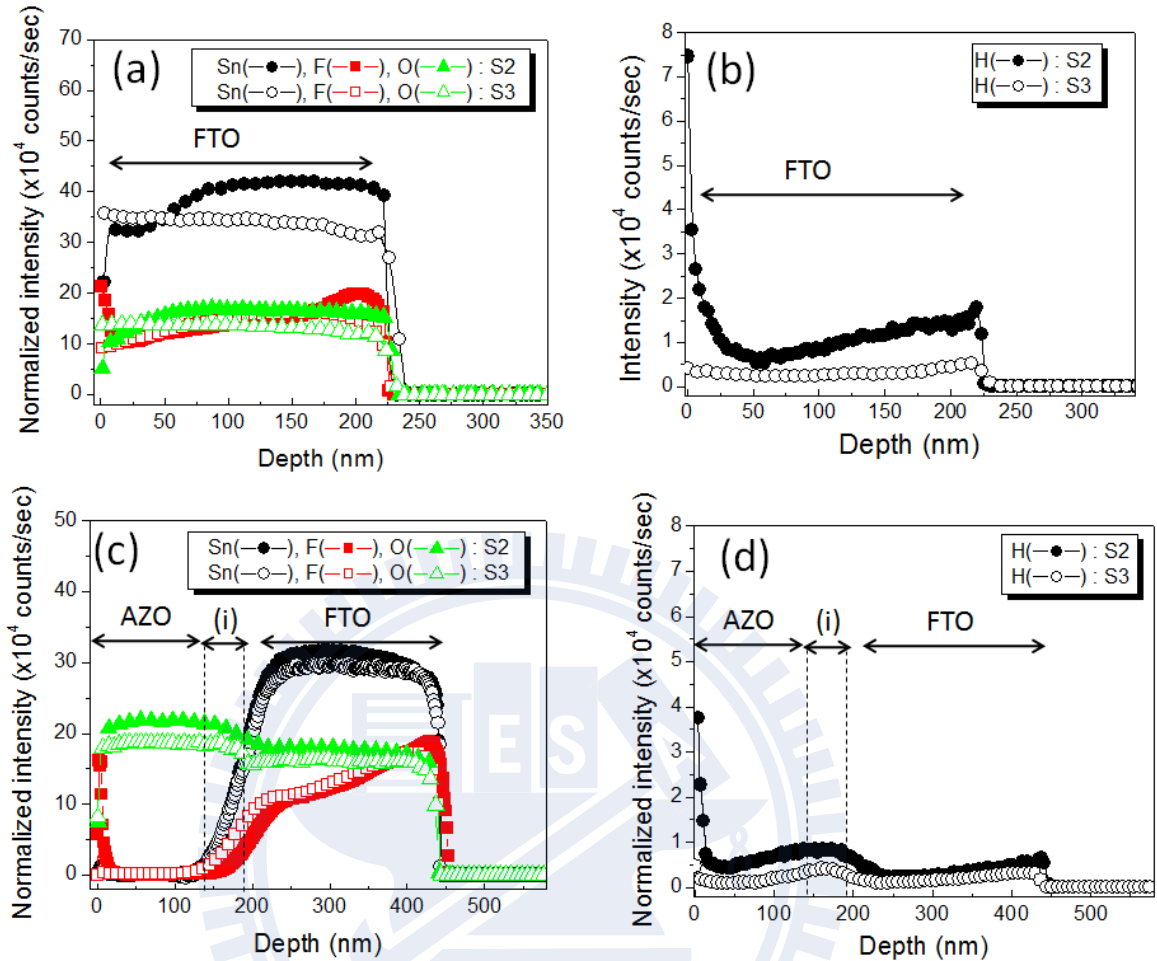


Figure 5.6 SIMS depth profiles of (a and b) FTO and (c and d) AZO/FTO films for secondary ion count of Sn, F, O, and H normalized relative to FTO. The plasma-treated samples and the post-annealed samples are represented by S2 and S3, respectively.

In Figure 5.6(c), a clear separation between AZO and FTO layers is identified as the interfacial region “(i)” where the Sn and F signal intensities increase drastically, indicating the beginning of the main components in FTO films and the appearance of their maximum intensities at stoichiometric point corresponding to the O signal intensity. Similar to the single

FTO film in Figure 5.6(b), Figure 5.6(d) shows the accumulation of H^+ ions at the surface and in the interfacial region, where it is assumed to have a lower surface energy compared with the mid-layer regions [127]. After the subsequent annealing process (S3), only slight changes in Sn and O intensities are observed. Because the AZO coated layer can prevent the dissociation of FTO film from H-ion incorporation, the variation in the intensity of all matrix elements shows only small changes between the S1-S2 (decomposition) and the S2-S3 (reoxidization or recovery).

To probe the detailed electronic structure of FTO and AZO/FTO films, we used XPS to investigate the oxidation states at the surface. The chemical bonding composition of the F dopant and the Sn element was examined by following the sequential process: as-deposited, H-plasma and post-annealing treated films are defined as S1, S2 and S3, respectively. For S1 in both film types, the primary spectra in Figure 5.7(a) and 5.7(b) do not show any F 1s peaks because of the very low level of F doping concentration in SnO_2 . If the FTO film preparation contained a proper level of F doping concentration, fluorine atoms would be expected to occupy the O site in SnO_2 to act as a donor in the generation of free electron carriers, rather than excess F atom at interstitial sites (F_i). Therefore, no signals corresponding to fluorine or its ionic form can be detected at this stage. Interestingly, after undergoing the H-plasma process (S2) for 30 min, the binding energy (BE) of the F 1s peak for the single layer FTO and double layer AZO/FTO films appears at 684.8 eV, which is composed of two deconvoluted peaks at 684.7 and 687.5 eV, assigned to F_1 and F_2 , respectively. As a result, it can be assumed that the replacement of oxygen with fluorine may have changed the doping behavior because of the incorporation of H atoms. This is because the interstitial hydrogen has a low formation energy and high mobility that can react with ion-absorbed oxygen (O^{2-}) in SnO_2 to form the strong O-H bond. In addition, the

reaction between H and O atoms could potentially have a great impact on the release of the F doping element from the O sites and a reduction of SnO₂ to a suboxide (SnO_x) or metal tin (Sn), leading to a loss in electrical conductivity. Because fluorine (F_i) is known to be one of the most reactive and electronegative elements, a consequential ionic fluoride such as a Sn-F bond could be readily formed on the surface of the film. Thus, a deconvoluted peak F₁ at low binding energy is meant to be the major component, represented by the Sn-F bond complex. In other words, an F₂ shoulder in the F 1s peak located at high binding energy can be observed, where the negligible peak is assigned for C-F bonds, which probably arise from the carbonaceous species in the atmosphere [125] and which are often found in the powder form. The intensity of F₂ is much lower than that of ionic fluoride (F₁) because the carbon-fluorine bond is much weaker and less dense in the FTO film [126] and is thus susceptible to thermal-induced desorption on the crystalline solid surface.

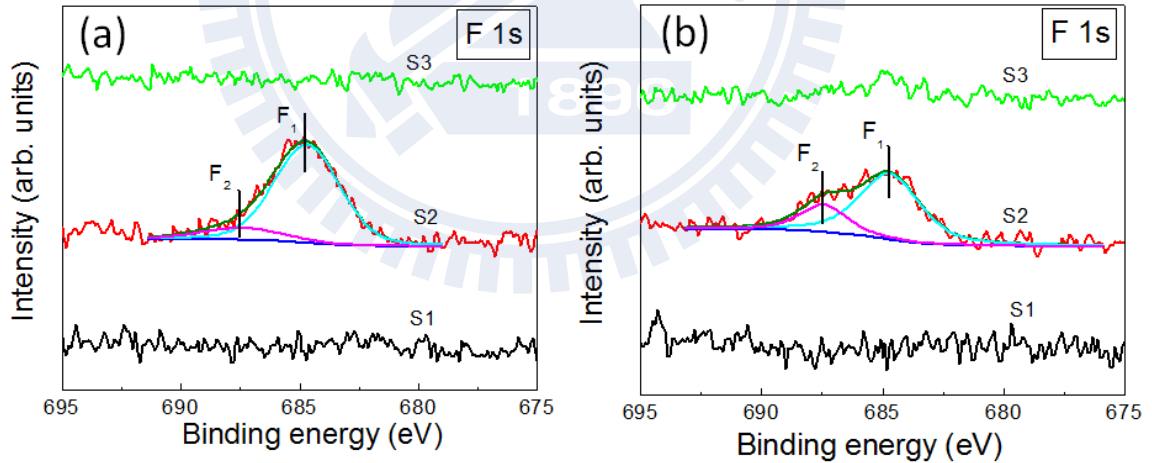


Figure 5.7 X-ray photoelectron spectra of the F 1s peak observed for (a) FTO and (b) AZO/FTO samples with as-deposited condition (S1), 30-min plasma treatment (S2), and post annealing process, subsequently. The deconvoluted peaks F1 and F2 indicate a major component (Sn-F bond) and a minor component (C-F bond), respectively.

Furthermore, we note that the single-layer FTO sample is much more disrupted than the double-layer AZO/FTO film in the presence of increasing H content above a critical value, because the major F_1 peak of the FTO film shows an increase in the formation of Sn-F bonds, while the AZO/FTO film a twofold decrease in the same intensity. The difference between the peak intensities in of the two films suggests that the barrier AZO layer partially prevents severe damage due to H-ion bombardment from occurring on the FTO film. At the final stage (S3), the samples were annealed at 400 °C for 1 hr to examine the desorption behavior of H atom. For the FTO sample, the peak nearly disappears because of thermal perturbation, which takes place in the presence of reoxidized SnO_2 . In contrast, a small amount of the F_1 peak in the AZO/FTO sample can be observed, which may represent the residual Sn-F bonds located at the interfacial layer between AZO and FTO films, particularly at grain boundaries.

In addition, Figure 5.8 provides further insight into the effect of H incorporation for both film types, demonstrating the variation in the $[\text{Sn}]/[\text{O}]$ atomic intensity ratios, derived from the XPS spectra in the inset of Figure 5.8. It shows the binding energy of the Sn $3d_{3/2}$ and Sn $3d_{5/2}$ electrons, a common signature of the Sn oxidation states (Sn^{4+}), corresponding to the equilibrium O-Sn-O species bound to the SnO_2 framework. These results are consistent with Figure 5.7 and indicate that the plasma (S1 to S2) and post annealing (S2 to S3) treatments on the FTO sample introduce decomposition and reoxidization of the Sn-O bonds, respectively. Note that the relative values of $[\text{Sn}]/[\text{O}]$ ratio at each individual stage show a gradual effect to the changes in the F 1s peak for the single FTO sample in Figure 5.7(a).

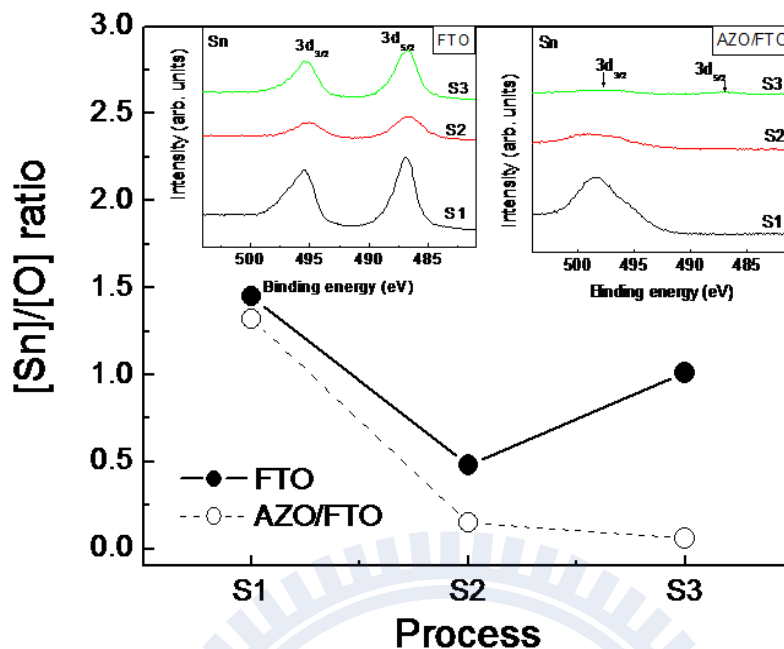
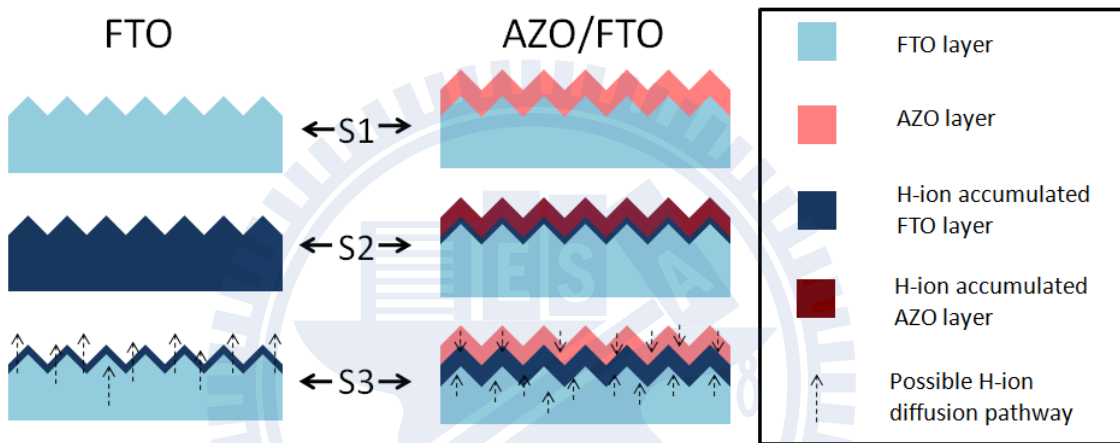


Figure 5.8 The variation of [Sn]/[O] atomic intensity ratios for the FTO and AZO/FTO films corresponding to the surface of as-deposited films (S1), the surface of H-plasma exposed films (S2), and the surface of subsequently annealed films (S3). The insets show the relative Sn (3d_{3/2}) and Sn (3d_{5/2}) core level spectra.

However, surprisingly, the AZO/FTO samples show a different result that the [Sn]/[O] ratio (Sn-O bonds) at S3 that is lower than that of S2, indicating a lack of recovery at the surface state of SnO₂ in the AZO/FTO sample. Indeed, despite possible variations in the chemical composition of the FTO film protected by the AZO overlayer upon H-plasma treatment (30 min) at S2, the result at S3 are extraordinary, and explained by Scheme 5.1 in the following manner: (1) the accumulation of H atoms at the AZO layer could be partially released beneath the FTO layer because of the heat-enhanced H-atom migration; therefore, the fraction of secondary H⁺ ions diffusion might play an important role on breaking chemical bonds at the crystal boundaries

of the surface of the FTO film. (2) The AZO-coated film also acts as the barrier layer to block some H^+ ions from diffusing outward from the plasma-treated FTO film, enhancing the dissociation of Sn-O bonds at the interface between AZO and FTO layers. Therefore, an improvement in film recovery might be achieved more effectively by using a post-oxygen plasma treatment, because of a decrease in the hydrogen concentration at the surface or interface of the film.

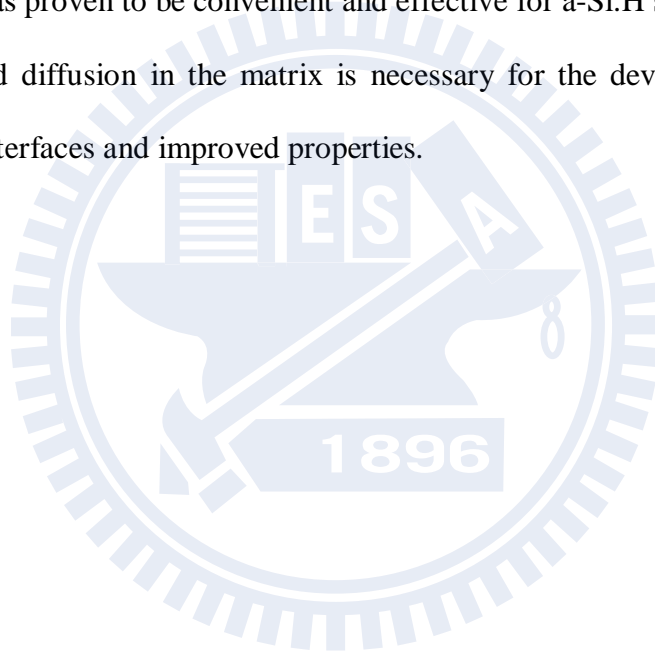


Scheme 5.1 Illustration showing the cross-sectional structure of FTO and AZO/FTO films and the possible H-ion diffusion mechanism under different conditions.

5.5 Summary

In summary, two types of films—a single layer FTO film and a double layer AZO/FTO film—were investigated for use as the transparent conducting oxide layer in hydrogenated amorphous silicon (a-Si:H) solar cells. The FTO was deposited by the spray pyrolysis method on a glass substrate, and then, the AZO thin film was deposited by radio-frequency magnetron sputtering method. The results show that the surface of bare FTO films can become deteriorated

because of the reduction of SnO_2 to metallic Sn and sub-oxide of SnO by H-incorporated ions and radicals under exposure to the H-plasma treatment. In contrast, the AZO overlayer was found to conserve the structural, electrical, and optical properties of the FTO film. In particular, TEM images reveal that following a 30 min treatment, H^+ ions and radicals from the plasma do not appear to significantly change the lattice structure at the interface, indicating an effective passivation of the oxygen vacancies ($V_o^{\bullet\bullet}$) in the upper-most FTO layer by the AZO protecting layer. Furthermore, the post-heat treatment (400 °C) results in the recovery of degraded FTO films. This strategy was proven to be convenient and effective for a-Si:H solar cells, while the H-ions incorporation and diffusion in the matrix is necessary for the development of multilayer films with designed interfaces and improved properties.



Chapter 6

Nitrogen Plasma-Assisted Co-doped P-type (In, N):SnO₂ Ultra-Fine Thin Films and N-ZnO/p-SnO₂ Core-Shell Heterojunction Diodes Fabricated by an Ultrasonic Spray Pyrolysis Method

6.1 Introduction

Transparent conducting oxides (TCOs) have yet to be widely used in electronic, optoelectronic and photovoltaic applications, including solar cells, flat panel displays, light emitting diodes (LED) and electrochromic (EC) materials [37, 101, 128, 129]. In particular, the TCOs provide various outstanding properties, such as thermal stability, high transparency and oxidation resistance, that are beneficial for developing device performance and the fabrication process. More specifically, light emitters and optical detectors [130, 131] require a structure that is composed of a junction between an n-type (electron) and a p-type (hole) conductor. The interface at the p-n junction could be a functional window that emits light when excited with sufficient photon energy. Unfortunately, it has been difficult to achieve active device fabrication using TCOs, due to the lack of a p-type conductivity component. Because most of the wide band gap oxides show unintentional n-type conductivity, researchers have tried to promote p-type properties by using different doping methods that incorporate doping elements (In, Li, Al, N and Ga) into n-type semiconductors based on II-VI and III-V compounds (ZnO, SnO₂, GaN, AlN and InN) [83, 132-137].

In this work, tin oxide (SnO_2) was selected as a promising host TCO because of its large band gap (3.6 eV), high exciton binding energy (130 meV) and high carrier mobility (250 cm^2). The SnO_2 crystal exhibits n-type properties in which the shallow donors are mainly generated by intrinsic defects (e.g., oxygen vacancies (V_o), tin interstitials (Sn_i) and the inadvertent incorporation of other impurities). Therefore, some difficulty is expected in overcoming an n-to-p transition and achieving low resistivity p-type conduction for SnO_2 because of its asymmetric doping limitations (self-compensation and deep acceptor level) [138, 139]. However, because of the variable valence bands of Sn, SnO_2 structural, electronic and optical properties can be more readily changed with the incorporation of additional defects. The material could also be suitable for possible acceptor dopants with proper doping concentrations and conditions. Although some groups have proposed different techniques for a mono-acceptor-doped SnO_2 to obtain p-type conductivity, the incorporation of a doping element into the host matrix still shows inferior properties, due to phase segregation (non-stoichiometry), relaxation and high resistivity [140, 141].

Because of the transient conductivity in mono-doped p-type SnO_2 , one possible method to improve the electrical properties is the incorporation of a group-V element. Sun et al. [38] investigated various properties of N-doped SnO_2 using first-principle calculations. On the basis of both theoretical analysis and experimental results, they found that a substituent N atom in the O site (N_o) has the lowest formation energy in O-rich conditions, which can preferentially enhance the p-type conductivity of SnO_2 . In particular, N_o is defined as the primary defect that compensates for the annihilation of oxygen vacancies; thus, N_o also affects the electrical and optical properties. Recently, Himmerlich et al. [142] examined the effect of nitrogen-plasma annealing on the properties of indium-tin-oxynitride (ITON). They studied how the optical

transmittance (T%) and resistivity (ρ) of films could be increased; due to the unbound nitrogen, the formation of metal-nitrogen (N-In and N-Sn bonds) and oxynitride bonds compensated for the oxygen vacancies. These reports are beneficial in terms of understanding the mechanism of additionally incorporated atoms. These atoms will be alternatively used to modify the intrinsic properties of host composite materials.

Presumably, simultaneous co-doping using dual acceptors can be expected to enhance the solubility of the dopant and give rise to shallow acceptor levels in the band gap. This investigation (based on plasma treatment) mainly improved the surface characteristics of the film. Selective co-doping elements were considered to introduce defect passivation, resulting in the increase of both carrier concentration and mobility for p-type conductivity, as compared with results from other reports [83, 141]. Moreover, none of these studies have been involved in co-doping methods in which p-type dopants were produced by a thermal diffusion process and assisted-plasma treatment. The scarcity of research regarding co-doping becomes more apparent in using different techniques to improve co-doping yield. Because reliable fabrication of a crystalline p-type-based SnO₂ film by a convenient and cost-effective route is in high demand, this study proposes a novel methodology that delivers (N, In)-co-doped SnO₂ through ultrasonic spray pyrolysis in combination with post nitrogen-plasma treatment to create an In-doped SnO₂ film. It is believed that both In and N are the best candidates for producing p-type SnO₂; the p-type conductivity mainly results from the In dopant because of its low ionization energy of substituent In_{Sn} atoms with modest strain effect [138]. In-doped SnO₂ is highly reactive to both reducing and oxidizing gases; therefore, a consequence of chemical surface treatment with nitrogen gas through the generation of an N_O acceptor is that the conductivity of the p-type host material is significantly enhanced.

Apart from the typical properties of thin films, a high aspect ratio of 1D nanostructure could be even more beneficial when chemical surface reactivity, quantum confinement, charge-carrier collection and transport are considered. Furthermore, 1D nanostructure is strongly desirable for the formation of p-type (N, In) co-doped SnO₂ by the surface effects of gaseous plasma treatment. Therefore, inspired by prototypical architectures, a rational synthetic method for 1D core-shell nanowires or nanorods is proposed. This investigation confirms that an ultrafine crystallite thin film (p-type SnO₂) with controllable size and texture can be formed on a rodlike template (n-type ZnO); this thin film behaves the same way as a conventional thin film. In terms of a p-n heterojunction, the core-shell nanostructure represents another technological challenge for a variety of applications in nanoscience, such as electronics, sensors, chemical reactors and drug release.

6.2 Fabrication and physical properties of In-doped SnO₂ films

The XRD spectra in Figure 6.1 show the structural evolution of In:SnO₂ films as a function of the films' composition. After annealing at 600°C (without In doping), peaks are observed at 2θ angles of 26.61, 33.88, 38.05 and 51.78°, which correspond to the diffraction of the (110), (101), (200) and (211) planes of the SnO₂ crystal, respectively. At 7%, the intensity of all diffraction peaks tends to decrease and shift toward the lower angles, as compared to samples with a lower doping concentrations. This decrease in intensity can be attributed to the fact that the larger In atoms (167 pm) exhibit a distinct preference for incorporation into Sn sites to substitute for the Sn atoms (140 pm) in SnO₂. In incorporation can lead to an increase in the lattice constant for the In:SnO₂ samples. For an over-doped sample (15% and 30%), the excess

In ions may cause a highly disordered structure and dissociation of Sn-O bonds, resulting in the loss of crystallinity in the SnO₂ film and the formation of In₂O₃ secondary phases (Figure 6.1). In this condition, the phase transformation of Sn-doped In₂O₃ may be induced; this structure is similar to that of ITO with Sn as a dominant donor in the In₂O₃ structure. When In is incorporated into SnO₂, the resulting disordered structure of the crystalline lattice agrees well with the electrical properties subsequently described by the Hall mobility.

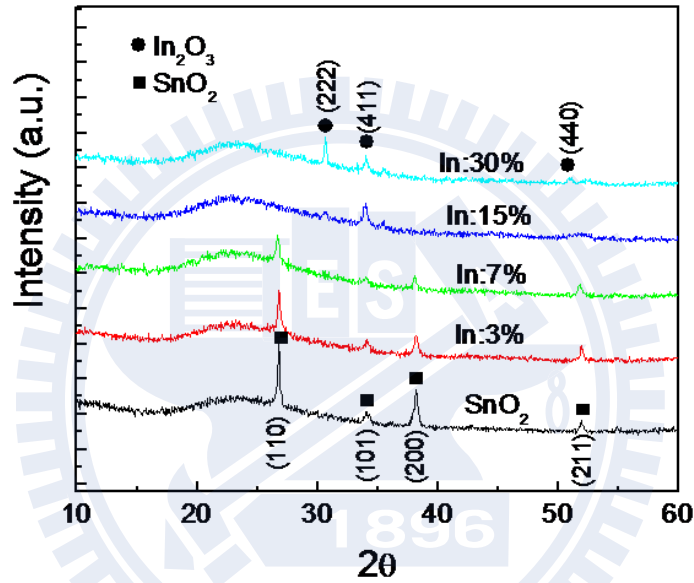


Figure 6.1 XRD peaks of In-doped SnO₂ films prepared by ultrasonic spray pyrolysis method with In concentrations: 0, 3, 7, 15 and 30 at%.

Figure 6.2 shows the optical transmission properties of the films doped with various In concentrations and annealed at 600°C. As in a conventional SnO₂-based film, the spectrum of the non-doped film shows high transmission in the visible region because it is a wide band gap semiconductor (~3.6 eV), whereas the absorption edge lies in the ultraviolet region (< 350 nm). After doping with In (3% to 30%), the transmission of the In:SnO₂ films significantly changes. Doping with In at concentrations ranging from 3% to 7% results in a slight decrease of the

overall transmittance of the thin films because the decrease was more profound for samples with impurity-induced light scattering. The introduction of a doping element into the film may create an impurity energy state, which is located at an energy level close to the top of the valence band, which is defined as the acceptor level. The electrons can readily be excited out of the valence band and jump into this level. Next, the holes are generated, thereby contributing to a lower electron carrier concentration. Consequently, the absorption edge shifts toward longer wavelengths. This result is in keeping with the electrical characterization described later in Figure 6.3. However, the doped films at 15% and 30% exhibit higher transmittances at a wavelength of 550 nm (> 95%) than the films with lower doping concentrations. In accordance with an increase in free carrier concentration (conduction) due to a large amount of intrinsic defects of In_2O_3 , the absorption edges of the spectra apparently shift back to shorter wavelengths. Higher states in the conduction band are occupied; this occupation accounts for the increase in the optical energy gap (referred to as the Burstein-Moss effect) [143, 144].

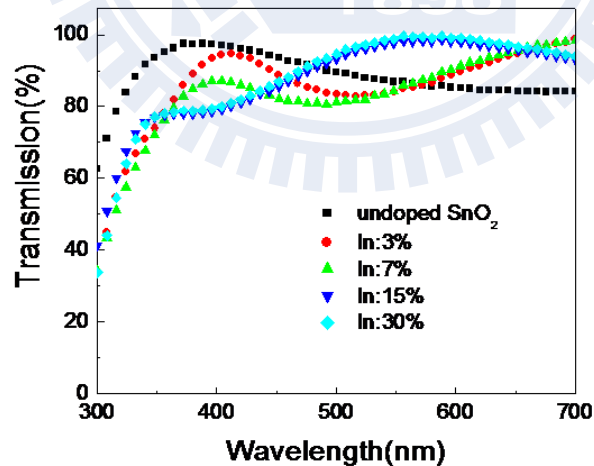


Figure 6.2 UV-vis absorption spectra of the In-doped SnO_2 film deposited on corning glass substrate with various doping concentrations. The optical transmission demonstrates the spectral continuity in range of 300-700 nm.

6.3 Effect of partial substitution of nitrogen on In-doped SnO₂ film surface

Figure 6.3 illustrates the dark current of both as-deposited and post-annealed In:SnO₂ samples with different plasma exposure times (0-40 min) of nitrogen atmosphere (gas) plasma. Before the annealing process, the SnO₂ in Figure 3a displayed n-type conductivity with a current of 0.8-1.7 mA; this n-type conductivity was due to two types of intrinsic defects: oxygen vacancies (V_o) and tin interstitials (Sn_i). For the In doping concentrations of 3% and 7% (Figures 6.3b and 6.3c), these intrinsic defects were corrected by elemental In, and the current was much reduced, as compared to undoped SnO₂ films. During the spraying process, both In and Sn precursors were deposited on the substrate at 400°C. Partial In was doped into SnO₂ and tended to substitute for the Sn, as well as generate holes to compensate for In_{Sn}^- (depending on the doping amount). According to defect chemistry, the principle charge to compensate for defects in In_{Sn}^- is assumed to be holes, if only a small amount of In was doped ($\leq 7\%$). As more excess In is doped, more hole carriers will be generated to neutralize the charge, and the principle charge to compensate for defects in In_{Sn}^- is V_O^{2+} . In this case, a p-type material can be formed, but the hole current will be smaller. With increasing doping concentrations (15% and 30%, Figures 6.3d and 6.3e), SnO₂ phase formation will be strongly influenced by the amount of In present during the spray deposition process, inducing more disorder on the crystallization of SnO₂. Even though Sn is a major component of the sample, In₂O₃ can be formed instead of SnO₂ because the formation enthalpy of In₂O₃ ($\Delta H_{In_2O_3}^f = -9.47$) is less than that of SnO₂ ($\Delta H_{SnO_2}^f = -6.01$) [145], as evidenced by the XRD of Figure 1. In this condition, In atoms not only occupy Sn sites to introduce In_{Sn}^- , but In₂O₃ can also be formed in combination with the incorporation of Sn into

the In_2O_3 matrix. Although some holes can still be generated, either SnO_2 or In_2O_3 intrinsically shows a dominant phase with n-type conductivity. Therefore, the electron current will be higher compared to 3% and 7% In-doped SnO_2 sample. This phenomenon is more apparent for a precursor solution containing 30% In. As indicated in the XRD, the In_2O_3 phase forms to become a major phase composed of Sn-containing In_2O_3 (n-type ITO), enabling the films to present a higher current than those containing other concentrations.

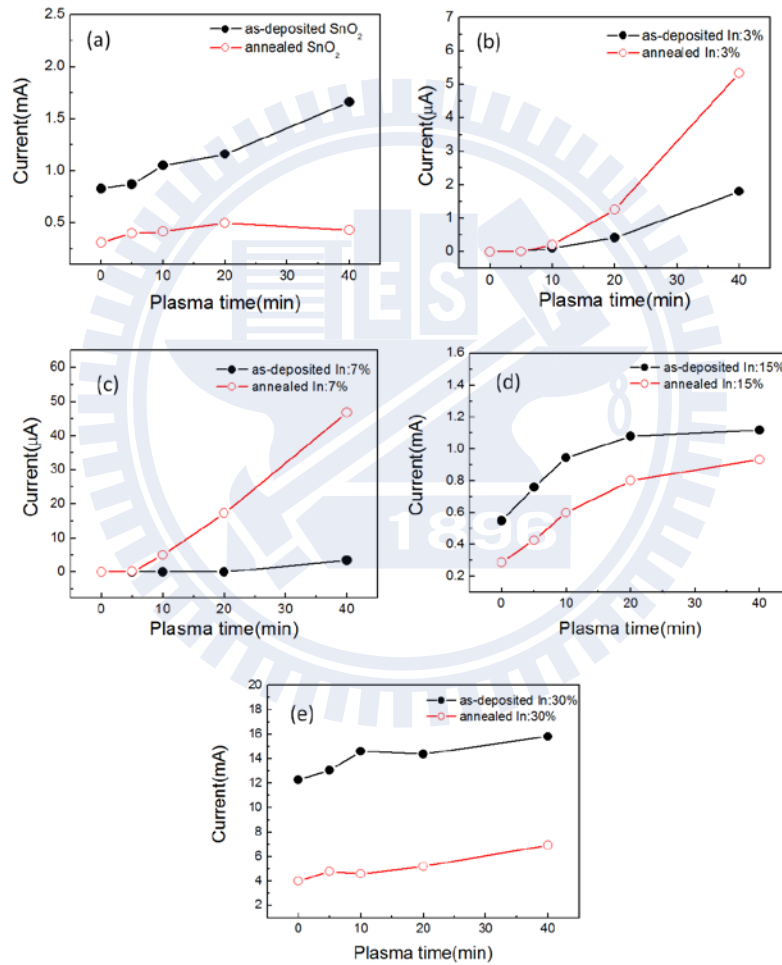


Figure 6.3 The In doping concentrations (0, 3, 7, 15 and 30 at%) during the film fabrication are shown in (a), (b), (c), (d) and (e), respectively, and the annealing temperature is constant at 600°C. Comparing dark current of as-deposited and annealed SnO_2 films undergoing the post plasma treatment (0-40 min).

To enhance p-type formation, all as-deposited samples were subjected to thermal annealing at 600°C for 1 hour, followed by nitrogen-plasma treatment. As shown in Figure 6.3, it was noted that only the hole currents of the 3% and 7% In samples were much improved after the annealing process compared to the un-annealed samples. In contrast, the samples with other doping concentrations show the opposite effect. For an undoped SnO₂ sample, a deterioration in conductivity was observed after thermal annealing (Figure 6.3a). This behavior is attributed to the reduction of intrinsic V_O defects in the annealing atmosphere, which leads to a decrease in the electrical current. Although the In atoms in the 3% and 7% samples were uniformly dispersed in the SnO₂ matrix in either the interstitial or substituent sites during the process of spray deposition, the substitution of In for Sn could actually be enhanced by thermal annealing. Therefore, the hole current can be increased, but the change is not obvious.

In a manner similar to that of the undoped SnO₂ samples, doping at high concentrations (15% and 30%) initially creates a large number of point defects, such as oxygen vacancies and unbound In³⁺ at interstitial sites of SnO₂ or In₂O₃. These point defects cause higher electron concentration and current compared to the samples with lower doping concentrations (3% and 7%). The subsequent annealing treatment mainly causes an absence of oxygen vacancies, resulting in the dispersion of unbound In³⁺ (undoped In) atoms to accumulate at the grain boundaries. Hence, much lower electron concentrations will be obtained, due to the possible trapping of more electrons.

It was noted that the nitrogen plasma effectively improved the current in all cases of undoped SnO₂ and In-doped SnO₂ samples by defect passivation. In this case, defect passivation works by implanting nitrogen atoms onto the surface defects of the film that were generated

during spray coating. As a result, the dark current can be increased by extending the typical plasma treatment duration of 5-40 min. However, the enhanced current will vary with doping concentration and annealing treatment. For In-doped 0%, 3%, 7%, 15% and 30% annealed samples, the current can be increased up to 1.39, 410.10, 525.05, 3.25 and 1.75 times, respectively, for 40-min treatment periods over the samples without nitrogen treatment. For the 3% and 7%-In containing samples, the current may be enhanced by nearly three orders of magnitude because the atomic N from nitrogen plasma can occupy the O site to form a large number of N_O substituents. This phenomenon will also generate many holes, which will increase the carrier concentration of a p-type semiconductor.

The Hall measurement characteristics are summarized in Table 6.1 to demonstrate the effect of elemental In doping in SnO_2 under co-incorporated nitrogen plasma (40 min). Evidently, the sheet resistance can be observed here to increase from 708.2 to 3.286×10^4 and 2.1×10^3 Ω/sq when elemental In was doped into SnO_2 at concentrations of 3% and 7%, respectively. The carrier concentration shifts toward positive values at $+3.31 \times 10^{17}$ and $+4.75 \times 10^{17}$ cm^{-3} , which are attributed to the replacement of Sn^{4+} by adding In^{3+} ions to generate p-type properties at a low In concentration ($\leq 7\%$). In this co-doping method, the N-plasma treatment ensures that (1) the enhancement in conductivity occurs due to defect passivation on the In: SnO_2 film surface compared to the untreated sample, and (2) the atomic N substitution into the O site in SnO_2 can reinforce the mechanism of In-doped SnO_2 to improve the p-type properties. Indeed, the 7% In: SnO_2 sample co-doped with N shows an excellent p-type film with large values for hole mobility (78.30 cm^2/Vs) and carrier concentrations ($+4.75 \times 10^{17}$ cm^{-3}).

Table 6.1 The results of Hall effect measurements of the annealed In:SnO₂ samples corresponding to 0-30% In doping concentration with a selective N-plasma treatment at 40 min.

Doping conc. (at%)	Sheet resistance (Ω/sq)	Mobility (cm^2/Vs)	Carrier conc. (cm^{-3})	Coeff (m^2/C)	Type
0	708.22	10.40	-1.06×10^{19}	-0.74	n
3	3.34×10^4	17.17	$+3.31 \times 10^{17}$	+23.61	p
7	2.10×10^3	78.30	$+4.75 \times 10^{17}$	+16.48	p
15	467.21	7.64	-3.60×10^{19}	-0.22	n
30	95.85	4.25	-1.12×10^{20}	-0.07	n

However, after further increases of the indium concentration to 15% and 30%, the resistance is dramatically decreased to 467.2 and 95.85 Ω/sq , respectively; the carrier concentration also reverts back to a negative charge, which indicates an electron-dominated transport effect. Importantly, the incorporation of In³⁺ in Sn⁴⁺ sites starts to become saturated, and the additional In ions can be possibly placed on interstitial sites to form a secondary crystalline phase (n-type In₂O₃) in SnO₂. As demonstrated earlier in Figure 6.1, this phenomenon may generate non-homogeneous distribution throughout the (N, In)-codoped SnO₂ film. A decrease in mobility compared to the 3% and 7% samples is caused by the increased disorder of the crystalline lattice, which corresponds to phonon and ionized impurity scattering [135]. Furthermore, Sn-doped In₂O₃ (ITO) may be produced at high In doping concentrations; at these concentrations, it is known as an n-type degenerate semiconductor with Sn atoms incorporated at In sites. The sample doping at 30% demonstrates a higher electron concentration ($-1.123 \times 10^{20} \text{ cm}^{-3}$) compared to one at 15% ($-3.601 \times 10^{19} \text{ cm}^{-3}$). One possibility is that the generation of In₂O₃ and Sn-doped In₂O₃ introduces the existence of a high content of oxygen vacancies, due to its

intrinsic defects during the deposition process. These intrinsic defects mainly improve the conductivity of the material.

Figure 6.4a shows XPS spectra of the N 1s with different plasma treatment conditions (0, 10 and 40 min). There was no N signal detected in the as-deposited In:SnO₂ film, while the N 1s peak, which was centered at 399.4 eV, was seen for the sample exposed to N plasma at 10 min. The exposure to N plasma corresponds to the formation of Sn-N-O or Sn-O-N oxynitride component [142, 143]. At longer plasma duration times (40 min), an additional peak appeared at 404.7 eV. This peak may originate from two possibilities: N-O bonds at the surface or unbound N atoms at interstitial sites [83, 142]. In Figure 6.4b, the depth profiles of the 7% In sample with 40-min plasma treatment were obtained using Auger electron spectroscopy (AES). Because of chemisorption and diffusion of the atomic N, the appearance of the N peak was observed at the near-surface region, and it gradually decayed from 67% to the detection limit at a 50-second etching time (depth in the range of 10-20 nm), whereas the atomic intensity of the Sn signal inversely increased from 20% to 75%. Importantly, the fluctuation of the O signal exists within the N-rich region (with an etching time of less than 25 seconds) and is subsequently decreased to its original atomic concentration as In-Sn-O compounds. For the In elemental composition, a low concentration profile was clearly detected throughout the depth of the film from 0-100 nm, which indicates that a small amount of In has been uniformly doped into the entire SnO₂ film. The atomic percent was unchanged regardless of the content of the nitrogen. Although In plays a key role in the p-type doping mechanism on Sn sites, the plots show that there is no close association between In and the variations of the other elements (Sn, N and O).

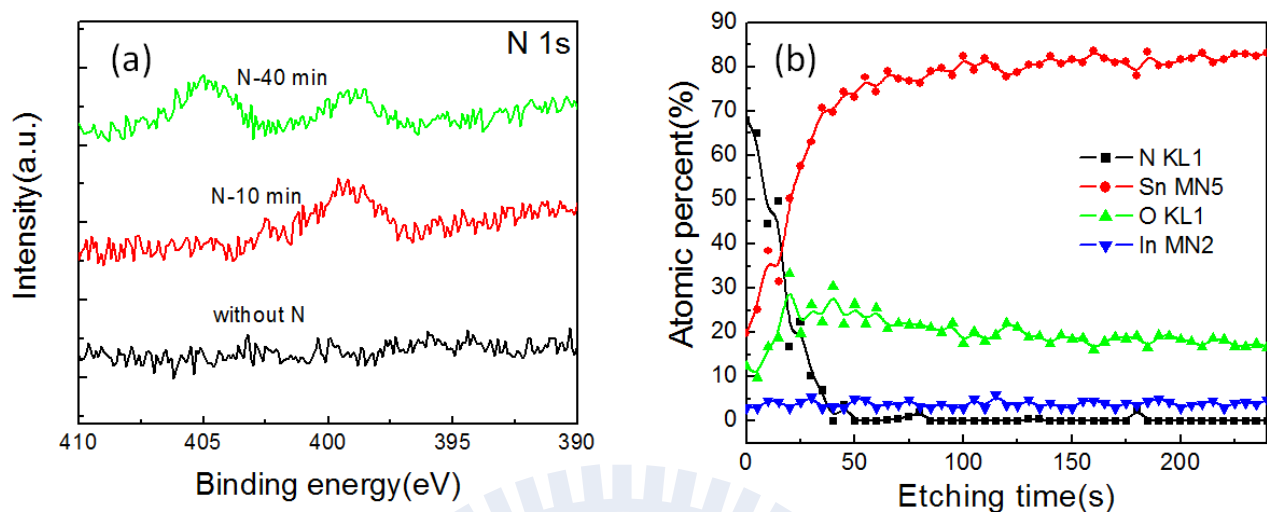


Figure 6.4 (a) XPS spectra of the N 1s peak observed for (N,In) co-doped SnO_2 samples treated in N plasma for 0, 10 and 40 min. (b) AES depth profiles of the sample in (a) at 40 min, and the etching rate of Ar^+ for 1 sec is equal to 3 Å in penetration depth.

A large bombardment of atomic N (generated by N_2 -plasma) strongly impacts the structure of SnO_2 films, due to the change in surface chemistry. N atoms can primarily substitute in O sites in SnO_2 at a low N concentration. However, if the incorporated N level is too high (at 40 min), the substituent sites (N_O) can be saturated with N atoms. Then, the excess N atoms will more readily fit in the interstitial sites (N_i) of the In: SnO_2 lattice, which is defined as unbound N_i atoms surrounded by Sn, In and O atoms [142]. Nevertheless, no peaks were observed at ~396 eV in the XPS spectra of the as-deposited film and N-doped film in Figure 6.4a, confirming that no bonds have been formed between Sn-N and In-N. Instead, the Sn-O bonds in SnO_2 can be disrupted when N is introduced to the surface because the variable valence bands of Sn are known to be an important factor in conducting surface oxidation or reduction [144]. The

segregation of Sn and O provides a possible route to the formation of dangling N-O bonds exposed to the surface because dissociated O atoms tend to form a weak bond with the nearest N_i atom at an oxygen-rich surface.

6.4 N-ZnO/p-SnO₂ Core-Shell Heterojunction Diodes

Due to the N-diffusion depth limit, this study intended to manipulate the ultrafine thickness of the p-type In:SnO₂ shells (~10 nm in thickness) deposited on n-type ZnO nanorods by optimizing the coating time (~3 min) and deposition temperature (400°C). Figures 6.5a and 6.5b show low-magnification SEM images of the vertically aligned core/shell arrays in top and side view, respectively. The length of the p-n core/shell was estimated to be about 220 nm. The high-magnification SEM image depicted in the inset of Figure 6.5a demonstrates a uniformly rough surface for the coating layers, which is different from the as-synthesized ZnO nanorods. The high resolution transmission electron microscopy (HR-TEM) image in Figure 6.5c clearly shows the crystalline In:SnO₂ nanoparticles to be well-distributed as a continuous film on the nanorod surface, indicating that the interfacial region exhibits an excellent crystallographic adhesion between the n- and p-layer. In addition, the selected areas for the highly magnified images and fast Fourier transform (FFT) diffraction pattern referred by JCPDFWIN clearly reveal the lattice spacing (d) at approximately 0.513, 0.338 and 0.266 nm. These spacings correspond to the (0001) planes of the wurzite ZnO core and to the (110) and (101) planes of the tetragonal SnO₂ shell, respectively.

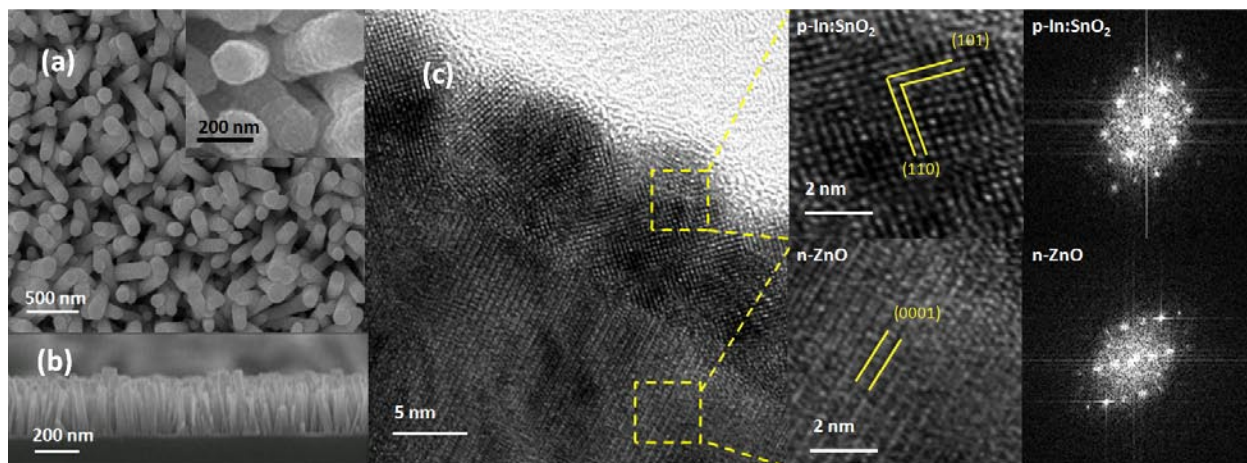
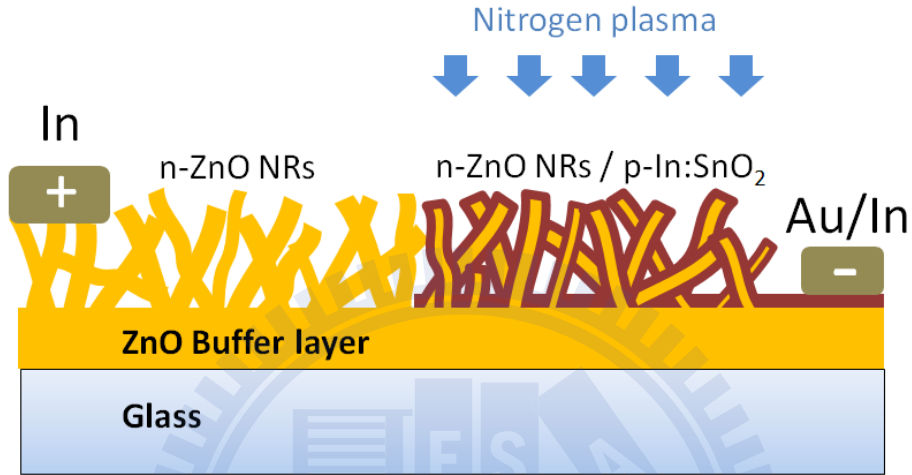


Figure 6.5 (a) Top view and (b) cross section SEM images of In:SnO₂-coated ZnO nanorod arrays. The inset shows a high magnification of top view image. (c) TEM images illustrate a pn heterojunction core-shell consisted of p-layer In:SnO₂ and n-layer ZnO with their lattice images and FFT patterns as identified by yellow.

To examine the electron-hole injection at the depletion region between the n- and p-layer, typical I-V measurements (Figure 6.6a) were conducted to confirm the electrical characteristics of (N,In)-codoped SnO₂. It was noted that the layer portion of the In:SnO₂-coated ZnO nanorods were only exposed to N plasma for 40 min, as illustrated in Scheme 6.1. The diffusion depth of the N atom can be approximately tuned with the treated In:SnO₂ layer thickness. The I-V characteristics of the ZnO/(N,In)-codoped SnO₂ core/shell demonstrate a symmetric curve with a rectified diode behavior, which means that the deposited films show a low level of interfacial surface recombination with very little leakage current in forward or reverse bias. However, both the individual p-type (N, In)-codoped SnO₂ film and the n-type ZnO nanorod are linear. This is a remarkable difference from the p-n heterojunction diode obtained by making ohmic contact with

In and Au/In electrodes. In all cases, the current could increase by prolonging the plasma duration time (> 40 min).



Scheme 6.1 Illustration of the corresponding current-voltage (I - V) measurement set-up. The deposition and post plasma process applied to fabricate the p - $\text{In}:\text{SnO}_2/\text{n}$ - ZnO core-shell heterojunction using ZnO nanorods as a template.

Figure 6.6b shows the energy band diagram of the p - $\text{In}:\text{SnO}_2/\text{n}$ - ZnO heterojunction at the equilibrium state. For the doping mechanism of the p -layer, the Fermi level (E_F) tends to shift toward the valence band (VB), according to the acceptor character or the presence of uncoordinated surface atoms. The E_F in the p -layer will align at the same energy level as in the n -layer; hence, band bending can be formed at the interfacial layer (defined as a depletion layer). Under external forward bias (J_F), the electrons from the bulk of the n -layer are repelled by the negative surface charge in order to overcome a built-in potential $V(x)$ at the interface before reaching the p -layer, and the electrons will behave in the opposite way under reverse bias (J_R).

Moreover, Drake and Sun et al. [38, 132] reported that some instances of a dominating formation of substituent N_o and In_{Sn} acceptors can occur, due to lower formation energy and annealing effects, respectively, compared to other interstitial atoms. In this case, the coordinate of these two acceptors introduces the impurity level located at the empty state slightly above the E_F , which can lead to the reduction of the energy gap ($\Delta E_{g2} = E_{g2}^* - E_{g2}$) by shifting the VB upward and can significantly promote p-type properties. However, if the doping concentration (N bombardment) is too high, interstitial N_i and N_{Sn} may be developed to compensate for the donor level close to the conduction band (CB), and N-O bonds and unbound N atoms may be formed (this possibility is consistent with the XPS result mentioned earlier).

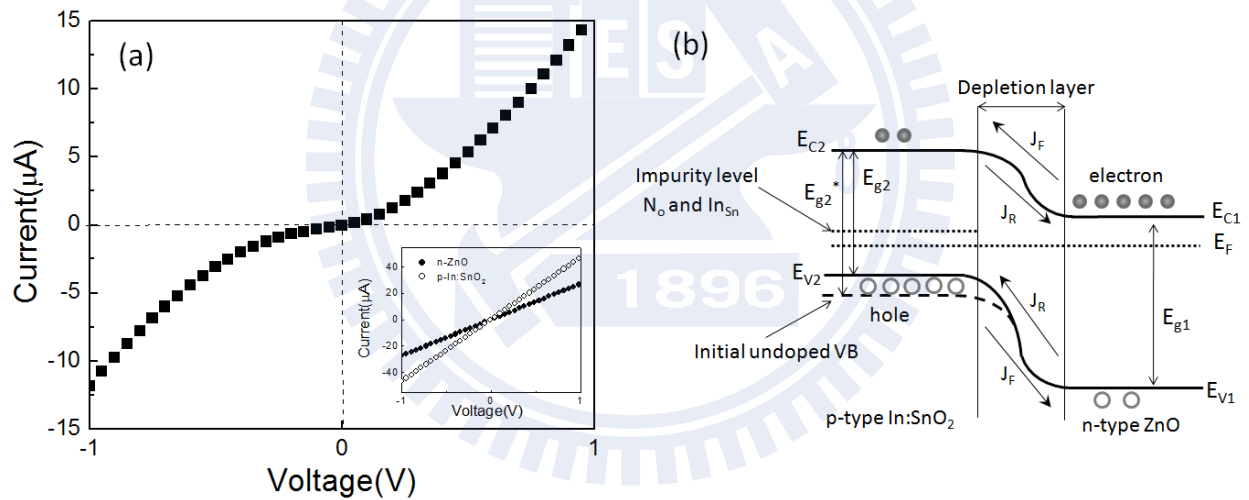


Figure 6.6 (a) I-V characteristics of the pn heterojunction diode in dark using an applied voltage in range of $\pm 1eV$. The inset gives the I-V characteristics of individual p-type $In:SnO_2$ and n-type ZnO films. (b) The energy band diagram at equilibrium.

6.5 Summary

It has been demonstrated that p-type In-doped SnO₂ films with 3% and 7% In doping concentrations can be fabricated by using a simple spray pyrolysis method followed by thermal annealing (600°C) and post-N-plasma treatment. However, excess doping concentrations (15% and 30%) can lead to the formation of a secondary compound, such as n-type In₂O₃. The formation of a secondary compound led to an electron-compensated donor, which dramatically reduced the sheet resistance to 467.2 and 95.85 Ω/sq for the 15% and 30% concentrations, respectively. Both XPS and Auger's depth profile analysis interpreted the mechanism of 7% In-doped SnO₂ under nitrogen plasma treatment by investigating the change in chemical bonding components. When the p-type (N,In)-codoped SnO₂ layer was deposited on the n-type ZnO nanorod arrays, the I-V measurement demonstrated a symmetrical curve with rectified diode behavior, which is responsible for high electron-hole injections at depleting regions between the n- and p-layer. The further optimization of specific conditions and parameters may need to be considered and will be crucial to design novel 1D hybrid materials suited for the various applications of TCO-based devices.

Chapter 7

Enhanced UV Photoresponse in Nitrogen Plasma ZnO Nanotubes

7.1 Introduction

One-dimensional (1D) zinc oxide (ZnO) is a promising semiconductor material in nanoscale electronics, optoelectronics and light-emitting device applications [55, 98, 146-158] because of its wide band gap ($E_g = 3.34$ eV), high electron-hole binding energy (60 meV) and the ease of cheap wet-chemical synthesis. The diversity of novel ZnO nanostructures, such as nanobelts (NBs) [146], nanowires (NWs) [147-150] and nanotubes (NTs) [159-161], has attracted attention due to the ways that its dimensionality corresponds to physical and chemical properties.

Up to now, wet-chemical approaches have been widely used to synthesize ZnO nanostructures. However, several defects may be generated on the surface of ZnO nanorods grown with an aqueous solution process. Recently, Sun *et al.* reported that the existence of hydroxyl groups (OH) and physisorbed water molecules on the surface of ZnO nanorods that can generate oxygen vacancies and defects, which affect the PL characterization and apparent photocurrent. Yuan *et al.* proposed that the gaseous dopant N_2O on ZnO NWs could compensate the intrinsic donor defects and achieve controlled electron-transport properties. A recent study by Le *et al.* demonstrated that nitrogen (N) incorporation into ZnO nanorods (NRs) under plasma exposure can efficiently induce the relative chemical bonding (increased O-Zn), but that it may result in the occurrence of lattice disorder.

Recently, ZnO nanotubes have been fabricated by many methods, such as a hydrothermal process, a template-assisted method and a thermal oxidation process [159-161]. Based on the high surface-to-volume ratio of ZnO NTs, it was believed that ZnO NTs have the possibility of improving charge collection and charge carrier transportation, thus enhancing performance and activity. Furthermore, the direct flow of electrons along a large interfacial surface area may contribute to a higher photocurrent generation.

Therefore, in this investigation, ZnO nanotubes (NTs) were produced by a low-cost chemical method, followed by the application of a nitrogen plasma. In order to better understand the photoresponse of NTs, ZnO nanowires (NWs) were also prepared for comparison. This letter discusses, for the first time, the photoresponse and photoluminescence behavior of nitrogen plasma-treated, chemically grown ZnO NTs. The nitrogen-treated ZnO NTs show a very good photoconductivity under long wavelength UV irradiation, as well as durability with extended exposure time, which can benefit ZnO-based solar cell devices.

7.2 Chemical growth of ZnO nanorods (NRs) and nanowires (NWs)

Figures 7.1a and 7.1b show scanning electron microscopy (SEM) images of ZnO NWs and NTs subjected to the nitrogen plasma treatment. Each NW, or NT, is 2–5 μm in length and has a uniform width over its entire length. After thermal annealing at 300 °C and longer plasma treatments, both ZnO nanostructures still show a uniform surface morphology. The high-resolution TEM image of the ZnO NWs in Figure 7.1c shows that the synthesized ZnO nanowires grow along the preferential [0002] *c*-axis direction with a diameter of around 25 nm.

For the ZnO NTs, figure 7.1d displays tubular structures with wall thicknesses of about 5–10 nm and inner diameters of about 10–15 nm. Furthermore, it was found that the diameters of both the ZnO NTs and NWs are very close in size, which can be attributed to the disappearance of the *c*-axis plane of the ZnO nanowires to form nanotubes [55, 151].

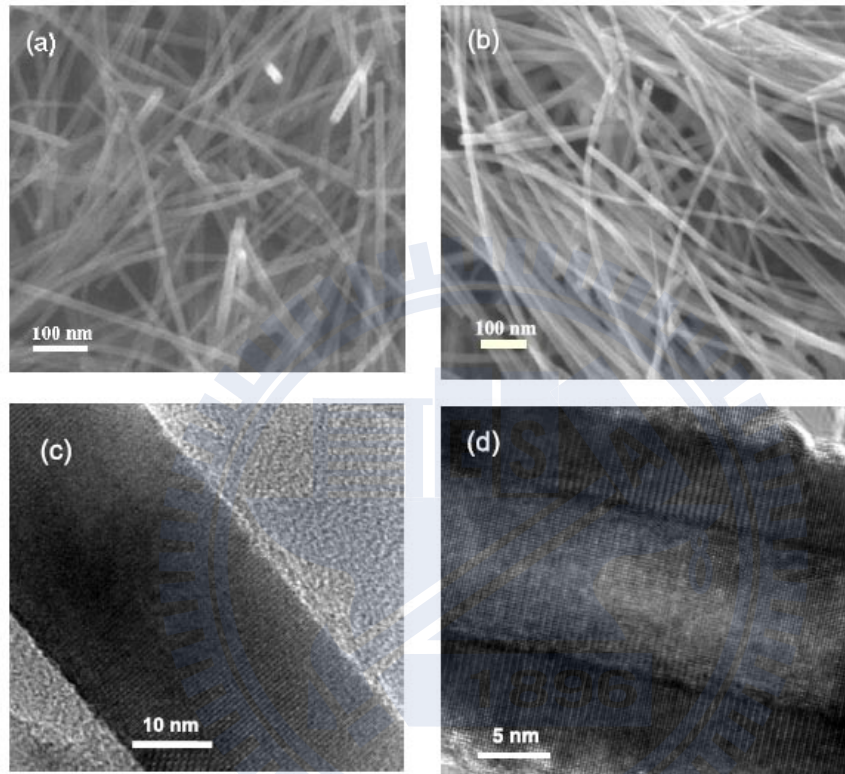


Figure 7.1 FESEM images: of (a) ZnO NWs and (b) NTs; HRTEM images (c) NWs and (d) NTs on glass substrates subjected to post annealing at 300°C and nitrogen plasma treatment.

7.3 Effect of N-plasma treatment on ZnO nanostructures

Figure 7.2 shows the room-temperature photoluminescence (PL) spectra of both ZnO NWs and NTs treated with different exposure times (0, 60 and 720 s) in a nitrogen plasma. Two distinct emission bands were observed: UV emission related to free exciton recombination at around 384 nm, and broadband deep-level emission related to native defects, such as oxygen

vacancies and zinc interstitials. After nitrogen plasma treatment, no damage was observed for both the NWs and NTs, and the emission intensity of the deep-level band was reduced, which is consistent with the report of Le *et al.*, who found that a N_2 plasma treatment can passivate the surface defects of ZnO nanorods. However, it was observed that the effect on the ZnO NWs was not as remarkable as the effect on the ZnO NTs, indicating the ZnO NTs show a greater relative reduction in surface defects than the NWs after the N_2 plasma treatment. Furthermore, it was noted that a long plasma treatment at 720 s caused enhanced UV and decreased deep level bands in terms of peak intensity, indicating that a surface reaction between the N ion and V_o^+ occurs on the ZnO. It is assumed that with a long plasma treatment, the N_i ions diffuse further into the core layer of the NTs and induce more nitrogen interstitials (N_i) to fill the V_o^+ defects of the NTs. Therefore, enhanced UV can be obtained.

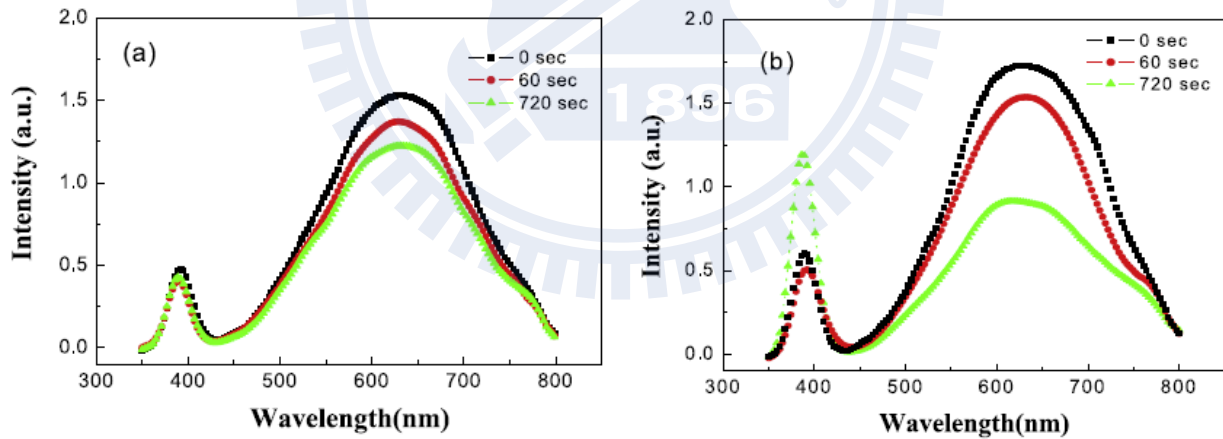


Figure 7.2 Photoluminescence spectra measured at room temperature for a nitrogen plasma treatment of 0, 60 and 720 s for (a) ZnO NWs and (b) NTs.

Figure 7.3a shows the current as a function of applied voltage with and without N_2 treatment for 900 s. The dark currents of untreated and N_2 plasma-treated NWs and NTs show

linear I –V characteristics, which indicate an ohmic nature in both cases. It was found that without N₂ treatment, both ZnO NWs and NTs generate a slight current (1.81×10^{-9} and 9.53×10^{-9} A, respectively). In contrast, a rapid rise in the dark current was observed for the ZnO NTs treated with N₂ plasma compared to those without treatment and to N₂-treated ZnO NWs. The current in the NTs is increased by a factor of 20 over that in the NWs after N₂ plasma treatment, which might be correlated with the larger surface area and thinner walls (~10 nm) in ZnO NTs. Normally, ZnO can be doped to be an n-type material due to the existence of oxygen defects, which contribute to the apparent photocurrent via filling or removal of the oxygen defect sites in the ZnO nanowires. Ahn *et al.* studied the photocurrent of a single ZnO nanowire synthesized by the sol–gel route and found that, in vacuum, the dark current was larger than in air; this can be attributed to the release of the available charge carriers by the desorption of physisorbed water molecules [57]; this might also be applicable to this work. The dark current of the ZnO NTs can be further enhanced after N₂ plasma treatment compared to ZnO NWs, because NTs have a relatively high surface to volume ratio and more electrons captured on the surface can be released.

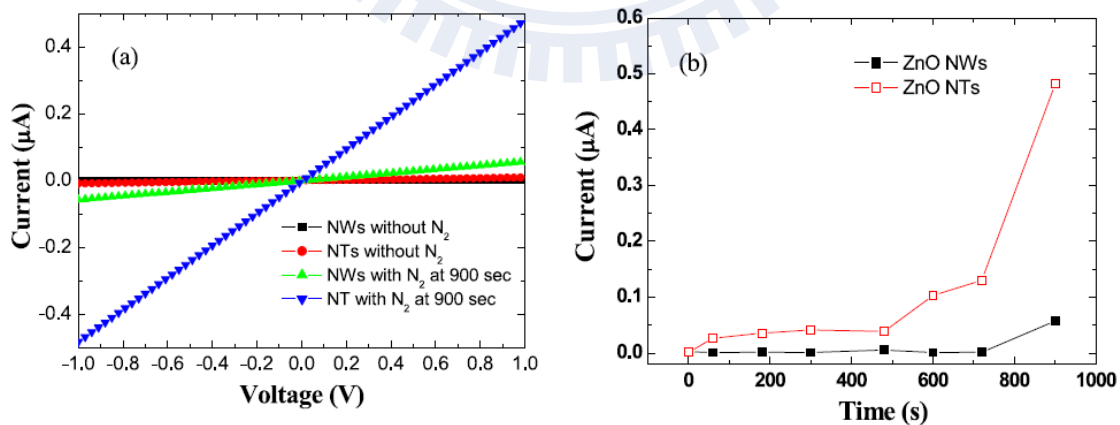


Figure 7.3 (a) Current as a function of applied voltage for both ZnO NWs and NTs, with and without a 900 s nitrogen treatment. (b) Dark current dependence versus N₂-exposure time.

Figure 7.3b illustrates the dark current of both ZnO NWs and NTs with different N₂ plasma exposure times. It was found that the dark current of the NTs shows a slight change after implant durations of 30–480 s. Beyond that, the enhancement in dark current is more remarkable for NTs after a long duration N₂ plasma treatment. The current can be increased up to 4.82×10^{-7} A at 900 s, which is much larger than that in ZnO NWs. It is believed that the surface defects in the solution-synthesized ZnO nanostructures normally have positively charged sites on their surfaces; these capture the electrons of ZnO electrostatically, reducing the available carriers in the air. According to our experiment, the N₂ plasma treatment can detach the surface defects, releasing the captured electrons and resulting in an increase of the conductance, especially under ion bombardment for a longer duration (>600 s) at an ICP power of 100 W, where there is the possibility of accumulating more energy to release further charge carriers by the detachment of physisorbed defects, such as water molecules inside the ZnO nanotubes. Therefore, an enhanced dark current can be obtained for the NTs after a long duration N₂ plasma treatment.

7.4 Photoresponse characteristics

Figure 7.4a shows the I-T plots and the photocurrent onsets generated by the excitation of UV irradiation in air at room temperature with a bias voltage of 1 V. After a longer N₂ treatment (900 s) for ZnO NWs and NTs, the ON–OFF cycles were exponential in generating a photocurrent with a reproducible response. It was noted that the N₂ plasma treatment for the NTs not only induced an increase in the dark current, but also enhanced the absolute magnitude of the photocurrent. The photoresponse enhancement for the NTs shows a remarkable increase by one order of magnitude over that of the NWs. It was assumed that the generation of an oxygen defect normally releases two electrons according to $O_0^{\times} \rightarrow 1/2O_2 + V_0^{2+} + 2e^-$, which contributes to

the intrinsic n-type nature of the ZnO nanostructure. This implies that oxygen defect vacancy (V_o^+) sites in the depletion layer are produced and become so unstable that they tend to be stabilized by combining with ambient negative charges, such as OH^- from physisorbed water molecules in the surrounding atmosphere (air), to form $V_o^+ - OH^-$ bonds, which result in a decrease in free electrons. Therefore, under UV excitation, $V_o^+ - OH^-$ pairs are broken, and electrons can be released from the detached hydroxyl OH^- groups on the surface of the ZnO nanostructures; this results in an apparent enhancement in photoresponse due to the larger surface/volume ratio of ZnO nanotubes without position dependent measurements of the UV illuminated lamp.

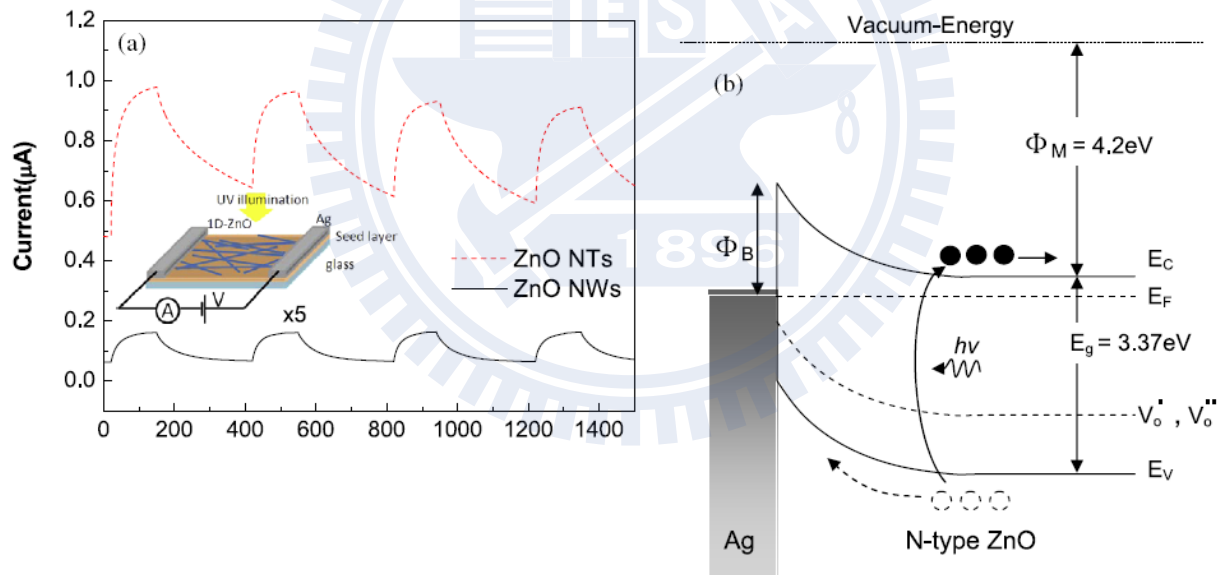


Figure 7.4 (a) Time traces of the current with the chopped light for samples measured after a 900 s N_2 plasma exposure under an applied voltage of +1 eV (electron conduction). The inset shows the schematic diagram of the corresponding measurement method. (b) Energy-band diagram for 300 °C annealed and N_2 plasma-treated ZnO under UV illumination.

On the contrary, the slow decay in the NTs at light off suggests a better stability and a more gradual electron–hole recombination than that found in NWs, which might be related to the defect sites, which capture or release the bypassing electrons and slow the reduction of the mobility of the photoexcited carriers in the ZnO NTs.

Figure 7.4b shows a schematic diagram to illustrate the electronic band behavior for ZnO NTs. A sufficient photon energy can generate electron–hole pairs, then excited electrons in the conduction band and unpaired holes neutralize oxygen ions at the surface [155, 156, 162, 163]. Due to the higher surface-to-volume ratio of the lower-dimensional NTs, the abundance of incident photons at the N₂-treated surface can readily break down the V_o⁺–OH[−] bonds, and the electrons transferred can subsequently overcome the large band gap. Evidently, the conductivity is governed by the carrier concentration, which is associated with the surface morphology of the ZnO NTs. The large direct band gap of the NTs (3.208 eV) demonstrates the enhanced carrier concentration, which leads to a decrease in the band gap and the Schottky barrier (Φ_B) at the grain boundaries.

7.5 Summary

In summary, a chemically based approach was used to develop ZnO nanotube (NT) and nanowire (NW) structures. The PL results show that a longer nitrogen plasma exposure can significantly improve the UV emission of ZnO nanotubes. Furthermore, the current–voltage characteristics show that the photocurrent (4.82×10^{-7} A) of NTs can be remarkably enhanced compared to that (0.571×10^{-7} A) of ZnO NWs after exposure to N₂ plasma for 900 s. This treatment also enhances the photoresponse behavior of the plasma-treated NTs (by a factor of 20 over that of NWs). Such a promising NT structure using a nitrogen plasma treatment may offer a

method of producing high optical quality ZnO nanostructures and could potentially be useful in the designs of 1D ZnO-based solar cells and optoelectronic devices.



Chapter 8

Selective Oxygen-Plasma-Etching Technique for the Formation of ZnO-FTO Heterostructure Nanotubes and Their Rectified Photocatalytic Properties

8.1 Introduction

Low-dimensional, nanostructured materials have attracted much attention for advanced electronic, optoelectronic, and photocatalytic applications because of their high sensitivity level and surface-volume characteristics. Of particular interest are coaxial nanotubes, in which core-shell hybrids are composed of oxide semiconductors, for use as three-dimensional (3D) transparent conductive (TCO) electrodes in photoelectrochemical cells.

In dye-sensitized solar cells (DSSCs), typically a TCO electrode has been used as the back contact for the nanostructured TiO_2 film. In particular, heterostructured, onedimensional (1D) electrodes have received great attention because of their chemically oxidative and hybrid properties, which were proposed to improve the conversion efficiency as an alternative approach to DSSCs [99, 164-166]. Recently, Wang et al. demonstrated that the photoelectric conversion efficiency of the DSSCs made from an indium-tin oxide (ITO) nanowire array embedded with the TiO_2 photoelectrode was higher than that of a pristine TiO_2 film or arrays of ITO/ TiO_2 core-shell nanowires [99]. Liao and co-workers reported hybrid CdS/P3HT photovoltaic devices using FTO-coated ZnO nanorod (NR) arrays as 3D electrodes. The FTO-coated ZnO NR length and thickness of the FTO layer were interpreted to enhance the photovoltaic performance [164].

Generally, the unique properties of ZnO are utilized not only in various aligned nanostructures for charge-carrier transportation and light emission but also as a free-standing NR, which is suited for uniformly nanosized templates and can be functionalized via interfacial solid-state diffusion with a surrounding shell layer. As a shell layer, the transparent conducting FTO is thought to be an ideal candidate electrode for solar cells. In addition, it was well-known that a high aspect ratio of 1D FTO nanostructures can provide far greater surface area than thin films, offering the additional challenge of obtaining effective charge-carrier collection and transport. Therefore, if the ZnO-embedded FTO could put forward the idea of extension into nanotubes with a completely hollow core, the large interfacial area between FTO and ZnO will play a critical role in improving the conduction path through nanoscale effects [61]. However, there have not been any reports involving the fabrication of a ZnO/FTO hollow nanotube and related optoelectronic properties. Therefore, when ZnO as the active light-absorbing component is combined with oriented FTO nanotube arrays, this composite nanostructure possesses excellent charge-transport characteristics, which will be a benefit for photovoltaic devices.

To the present, there have been a number of reports on template-assisted oxide nanotube formation by various synthesis methods. Selective etching is one important technique to produce controllable structures, including wet-chemical etching [62, 92, 167-169] and hydrothermal treatment [91, 170-173]. Zeng et al. developed wet-etched Zn-ZnO core-shell nanoparticles (NPs), where H^+ ions incorporated from a weak acid solution diffused along lattice defects and grain boundaries in the ZnO shell layer to eliminate Zn core materials via a redox-precipitation process at the interface [92]. Fan et al. developed $ZnAl_2O_4$ nanotube structures using hydrothermal calcination. The formation mechanism includes the occurrence of defects and voids along the core-shell interface, and the Kirkendall effect with surface diffusion produces

hollow interiors [91]. Yao et al. proposed a two-step etching process on ZnO NRs, which entails both chemical and plasma etching at low temperature [173]. A wet acid solution provides a rough isotropic etch of hexagonal edges, and then argon plasma is employed to fabricate controllable nanotips for enhanced field-emission devices. However, the wet-etching process leads to a morphology with a high degree of disorder, causing a lower photocatalytic efficiency due to photocorrosion. Therefore, it is very important to develop a dry-etching synthesis process for the metal oxide semiconductor in solar cell applications. To date, there has been little research on dry-etching mechanisms, in which a controllable etching rate could improve the optical properties of the materials. The use of oxygen plasma to eliminate the inner core of metal oxide compounds has only been studied in a few cases, but this novel method could introduce the benefits of hollow nanoscale materials.

In this paper, we propose a fabrication method to synthesize ZnO-FTO composite nanotubes using water-based spray pyrolysis for depositing FTO NPs on arrayed ZnO NRs and oxygen plasma for the etching process. During the process, various ions and radicals generated by the oxygen plasma, including O^+ , O^{2+} , and O^* , can readily diffuse into oxygen vacancies [174-176] to create negative charges on the ZnO NR surface. This results in an accelerated etching rate, producing a large number of voids in ZnO and forming a hollow ZnO-FTO heterostructure. The mechanism of etching evolution of the ZnO-FTO nanotubes via oxygen plasma was also investigated in this study. In addition, the corresponding enhanced photoresponse of the heterostructures will also be discussed.

8.2 Microstructure of FTO-coated ZnO nanorod arrays

Figure 8.1a is a high-magnification scanning electron microscopy (SEM) image showing the ZnO NR array structures, with NR lengths ranging from a few tens to hundreds of micrometers and diameters between 50 and 100 nm. After FTO coating, the ZnO NRs become larger in diameter because of the additional rough FTO layer covering the entire ZnO NR, as shown in Figure 8.1b.

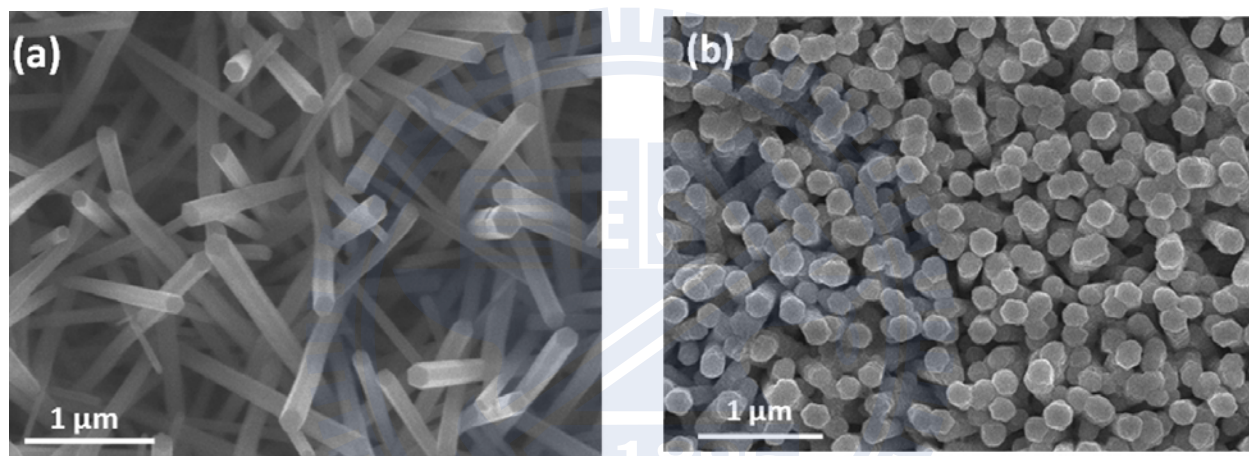


Figure 8.1 Field-emission SEM images of (a) as-deposited ZnO NRs grown on a Corning glass substrate using a hydrothermal method and (b) FTO coating on ZnO NRs obtained by spray pyrolysis deposition. The FTO deposition time was 2 min at 380°C.

8.3 Oxygen-plasma-etching mechanism on ZnO nanorod templates

Figure 8.2 shows high-resolution transmission electron microscopy (HRTEM) images of a core-shell ZnO-FTO heterostructure (a) before and (b) after exposure to oxygen plasma for 20 min at room temperature. The low-magnification image in the inset of Figure 8.2a illustrates that the FTO monolayer has uniformly covered the ZnO NRs to form a ZnO-FTO core-shell structure. The HRTEM images magnified from the red rectangle in the inset of Figure 8.2a

further demonstrate that the FTO layer on the ZnO NRs is composed of FTO NPs, with a wall thickness of about 15 nm. On the other hand, for ZnO-FTO composites treated with dry oxygen plasma, the ZnO NR core was removed to form a 1D tubelike FTO nanostructure, as shown in the inset of Figure 8.2b. This occurs because the wurtzite ZnO NR template can be more rapidly etched along the [0001] direction compared with the tetragonal rutile FTO. The HRTEM image in Figure 2b reveals that the ZnO-FTO composite nanotube contains ZnO-{0001} and FTO-{100} planes, with the lattice spacing of certain atomic planes at about 0.475 and 0.295 nm, respectively. Consequently, it can be assumed that some residual ultrafine ZnO nanocrystals have been embedded into the surface of the FTO shell layer after the etching process through an interfacial solid-state reaction between ZnO and FTO [62, 91, 172].

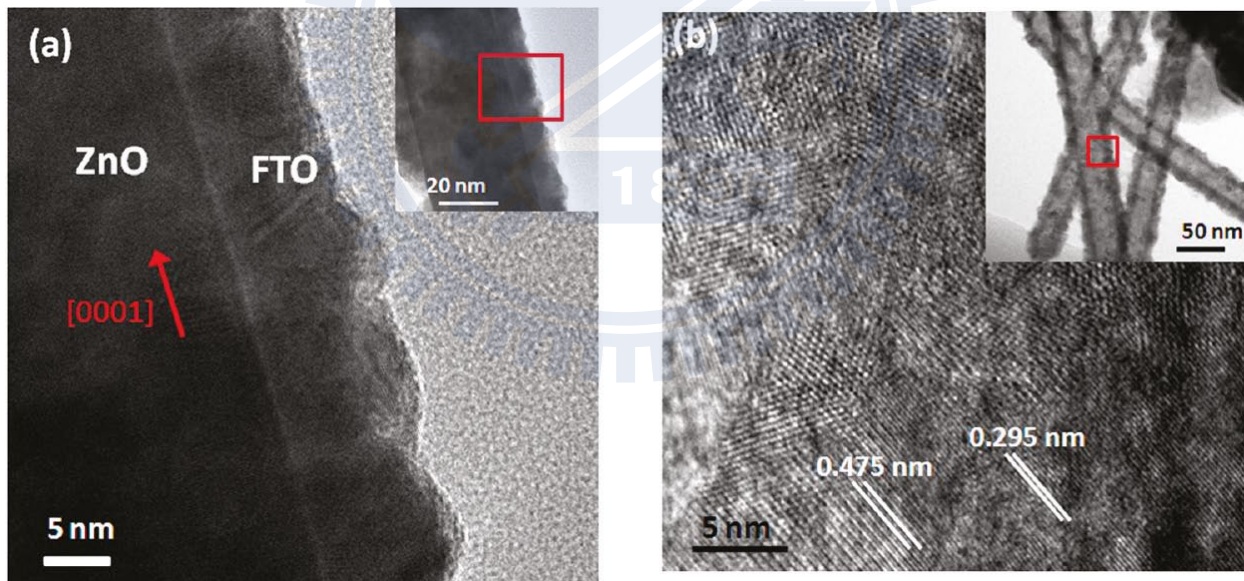


Figure 8.2 HRTEM images of core-shell ZnO-FTO heterostructures (a) before and (b) after exposure to oxygen plasma for 20 min at room temperature. The insets of parts a and b show the magnified interface, indicated by the red rectangle.

The cross-sectional images, analyzed by transmission electron microscopy (TEM)-energy-dispersive spectrometry (EDS) line scans across the tube diameter (side view, Figure 8.3a,b; top view, Figure 8.3c,d), show hollowlike regions, which clearly indicate a ZnO-FTO heterogeneous nanotube. The EDS elemental line scans on the ZnO-FTO samples indicate that, after dry etching, the heterogeneous structure is mostly composed of Sn, with residual ZnO isotropically distributed either alongside or in the interior of the FTO tube wall. In particular, the relative composition ratios of the elements Sn, Zn, and O were estimated as about 4.5:1:3.5 (side view) and 7:1:6 (top view), respectively. As a result, the relative ratio of Sn to Zn in Figure 8.3d is apparently larger than that in Figure 8.3b, further confirming that the ZnO region in the core has been etched successfully.

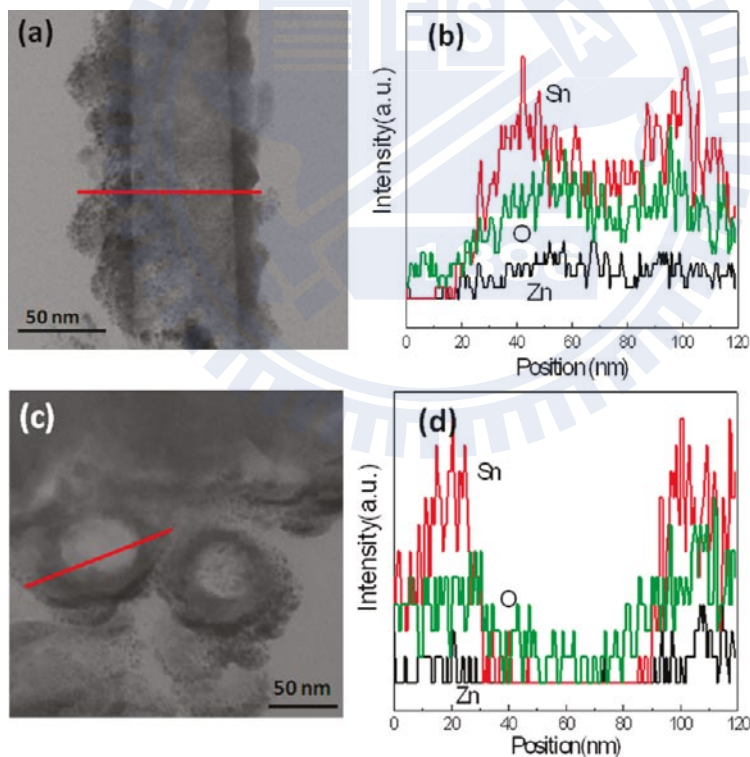


Figure 8.3 Cross-sectional HRTEM and EDS line scans of an ZnO-FTO nanotube fabricated by dry oxygen-plasma etching at 20 min: (a and b) side view; (c and d) top view.

The relative removal of the inner core using the oxygen plasma treatment under RF power (350 W, at room temperature) with etching time was also observed. The TEM images in Figure 8.4a-c show the structural evolution of the inner ZnO core corresponding to different treatment durations (0, 2, and 20 min, respectively). The TEM image in Figure 8.4a shows an interfacial gap after spray coating of the FTO onto the ZnO NRs between the FTO layer and ZnO, caused by the lattice mismatch between the two. Oxygen plasma etching for 2 min can lead to a polycrystalline ZnO sheath with formation and enlargement of the voids along the ZnO-FTO interface, as indicated in Figure 8.4b, suggesting that the voids were possibly initiated from the mismatch sites between the FTO layer and ZnO. With increased reaction time (20 min), it can be seen in Figure 8.4c that the inner ZnO core was almost consumed and the hollow formation took place along the [0001] plane to form a nanotubelike structure.

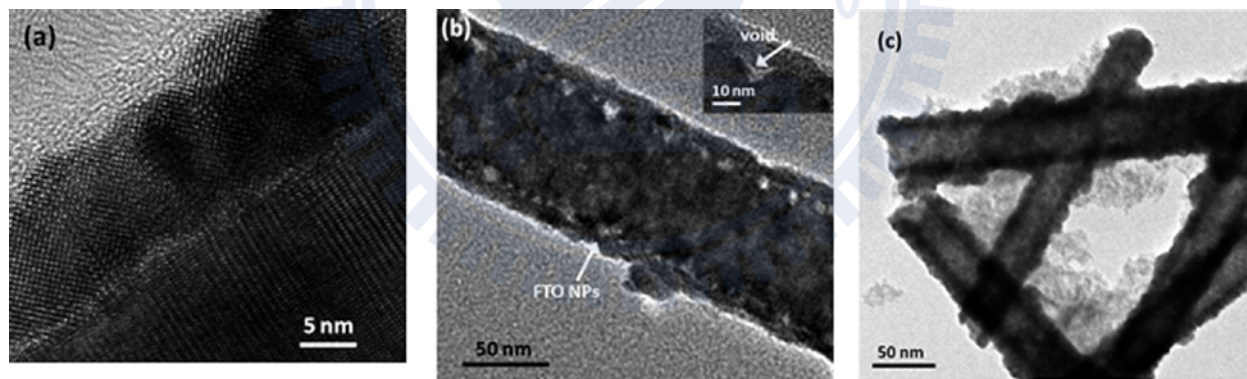


Figure 8.4 Formation of voids in the FTO-coated ZnO obtained before and after etching of ZnO NRs as a function of time: (a) 0min; (b) 2min; (c) 20min. The inset of part b is a high-resolution image of the void.

The XRD pattern in Figure 8.5 shows the characteristic peaks of a ZnO-FTO core-shell structure as a function of the etching time. As-grown ZnO NRs mainly display oriented peaks in the descending order of (100), (002), (101), and (110), and as-deposited ZnO-FTO shows the

additional FTO peaks to the ZnO peaks. After treatment with the oxygen plasma for 2 min, the relative peak intensity of ZnO was reduced, although the (100) peak can still be observed. A long oxygen-plasma treatment time of 20 min resulted in a further reduction in the ZnO peak intensity so that it became negligible. Thus, the XRD peaks of the ZnO-FTO tubelike heterostructures display differences from the as-deposited ZnO-FTO. This indicates that the ions and radicals from the oxygen plasma indeed impart an impact energy to the ZnO NRs to induce different degrees of etching, which cause a morphological transformation. The impact energy from the oxygen plasma is high enough to induce transformation and dissociation of ZnO, suggesting that more excess vacancies could be generated and accumulated at the interfaces. This suggestion is confirmed by PL, which will be discussed later.

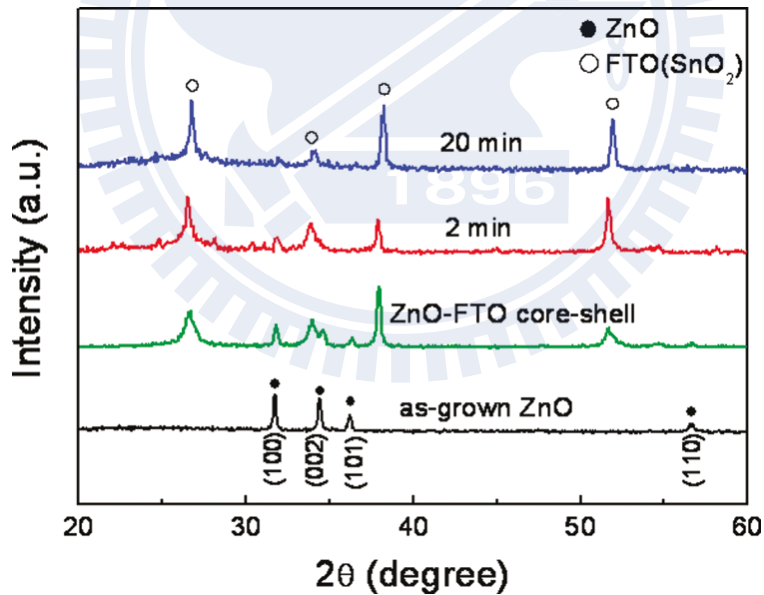


Figure 8.5 XRD patterns of as-grown ZnO and ZnO-FTO heterostructures on glass treated for the times noted under oxygen plasma. The patterns are vertically offset for clarity.

Figure 8.6 shows room-temperature PL spectra using 365-nm UV excitation for ZnO and ZnO-FTO treated with oxygen plasma for 0, 2, 10, and 20 min. Two main bands were obtained: the strong peak in the UV emission spectrum at 380 nm corresponds to the near band edge (I_{NBE}) generated by the recombination of free electrons and a broad-band visible deep-level emission (I_{DLE}) centered at ~ 600 nm induced by impurities and defects such as oxygen vacancies (V_{O}^+) and zinc interstitials (Zn_i) [148, 177, 178]. It was found that with, a plasma treatment duration of 2 min, well-aligned ZnO NRs with well-defined hexagonal planes remained unchanged. However, under a longer plasma duration, such as 10 min, the pristine ZnO NR displayed a relatively enhanced defect density, which caused a decreased I_{NBE} and an increased I_{DLE} , as expected (Figure 8.6a). These results are probably related to deterioration of the ZnO NRs, as seen in the inset of Figure 8.6a.

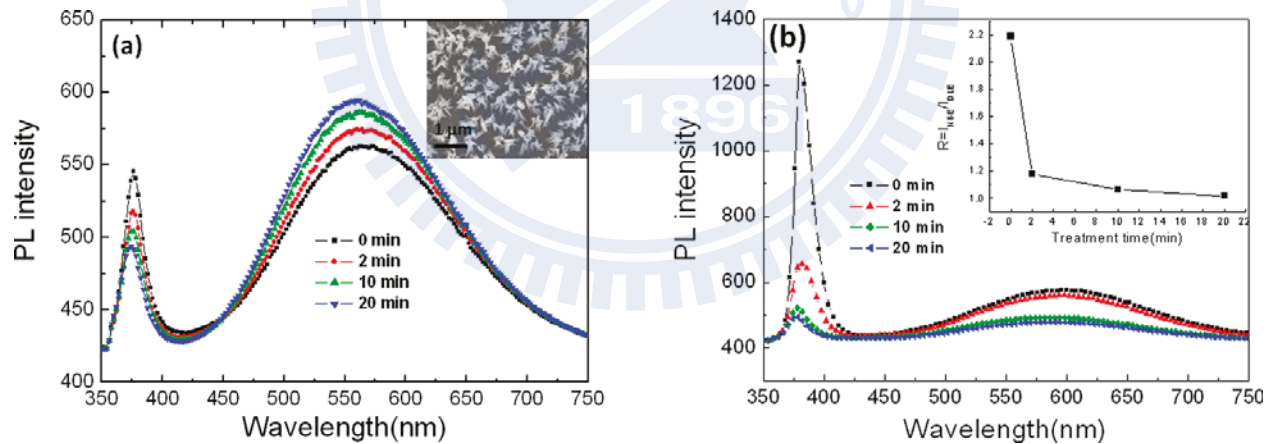


Figure 8.6 PL of (a) as-grown ZnO and (b) FTO-coated ZnO samples showing variation of the spectrum intensity corresponding with the plasma exposure time. The insets of parts a and b demonstrate the morphology of the ZnO NRs after 20 min of etching and the relative intensity (R) of part b, respectively.

On the other hand, after FTO coating, it was observed that I_{NBE} from ZnO was enhanced compared to the pristine ZnO because of defect passivation. However, with a plasma etching

time of 2 min, Figure 8.6b shows a significant reduction in I_{NBE} but only a slight reduction in I_{DLE} . After plasma treatment (>2 min), it was found that both peaks were reduced to a negligible height, indicating that ZnO could be etched after FTO coating using a longer oxygen-plasma treatment. This reveals that the FTO shell can not only passivate the surface defects on the ZnO NRs to enhance I_{NBE} but also trigger the ZnO etching of the ZnO-FTO nanocomposite to produce the ZnO-FTO nanotube heterostructure. All of the evidence confirms that the FTO layer plays a key role as a gas nanocatalytic absorber [10, 179-181] to enhance the etching activity on the ZnO template. It was assumed that the phase transformation of ZnO solid to Zn vapor was initiated by the sprayed FTO NPs and the oxygen-plasma treatment at the ZnO-FTO interface. Later, it was found that, with a prolonged oxygen-plasma treatment (>2 min), ZnO in the interior was continuously etched, along with void formation and phase transformation of ZnO solid into Zn vapor, which induced the defect diffusion outward from the core layer and promoted the formation of a tubelike structure.

To further understand the possible oxygen-plasma-etching mechanism, XPS was performed on the samples. Parts a and b of Figure 8.7 show the XPS spectra of the O1s peak in the as-synthesized FTO-coated ZnO samples without and with a preheat treatment, respectively. It shows a correspondence to the binding energy of the occurrence of two deconvoluted components: formation of the hydroxyl (OH) functional group at 532.89 eV may be generated during hydrothermal growth or wet-solution-based synthesis and the O^{2-} ions bonded in the lattice (Zn-O and Sn-O) as identified at 531.32 eV. However, the hydroxyl peak is negligible compared to the O^{2-} peak.

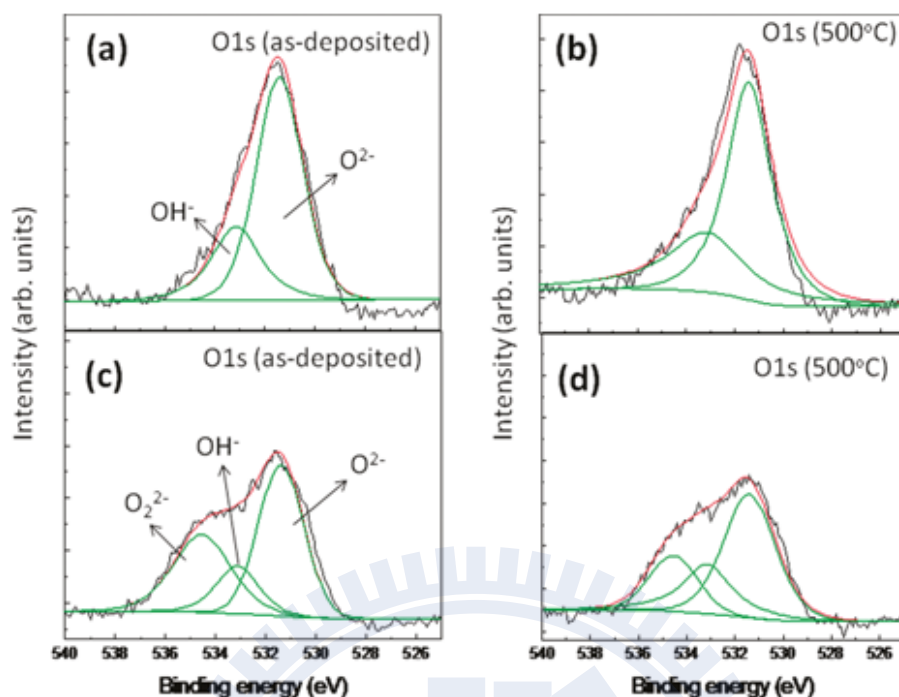


Figure 8.7 XPS spectra of the O 1s peak in FTO-coating ZnO samples: (a and b) before and (c and d) after plasma etching (350-W RF power for 20 min), preparing the samples with and without preheat annealing at 500°C, as indicated in each figure.

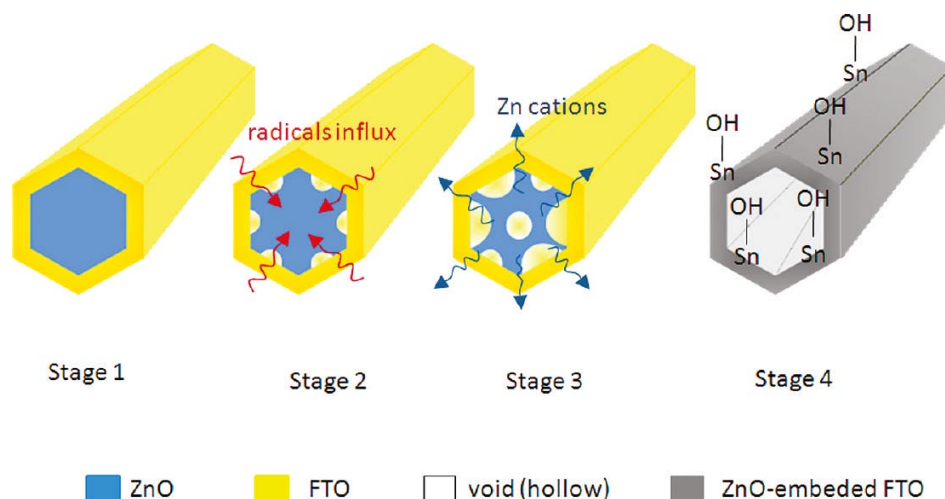
After exposure of the samples to a 350-W oxygen plasma for 20 min (Figure 8.7c), it is apparent that the plasma treatment caused a decrease in the number of the O^{2-}/OH^- concentration ratio, as compared to samples that did not undergo the plasma process (Figure 8.7a). More specifically, it is implied that the OH^- ion, produced by the oxygen plasma, is initially physisorbed onto the FTO surface. The hydroxylated FTO substrate is then constructed in the form of Sn-OH at the outermost surface via oxidation and nucleophilic attack of H_2O molecules in the atmosphere. For the reaction under ambient conditions, the active species in the oxygen plasma (OH^-) also induces the accumulation of hydroxyl radicals ($\bullet OH$) at the FTO surface because of a primary photocatalytic effect, for which the radicals in the gas phase could be generated and diffused toward FTO, interfacial ZnO-FTO, and the ZnO layer, respectively. Thus,

the dissociation of Zn-O bonds can be caused by the impact of •OH radicals from the physical bombardment of oxygen molecules and the shift of the cationic zinc species away from the core center. Meanwhile, oxygen plasma could also introduce defects (oxygen vacancies) into the FTO surface. If FTO has defects, the oxygen-plasma incorporation might result in a reduction of the O^{2-} concentration from Sn^{4+} -O (FTO). Thus, the existence of Sn^{2+} -O bonds (tin monoxide, SnO) could be observed [182, 183] and confirmed as the contribution of O-Sn-OH, meaning that the native oxide layer was eliminated from the depletion region at the surface, as demonstrated in Scheme 8.1. Furthermore, the binding energy of 534.55 eV was assigned to the generation of molecular oxide and tin bonding (O_2^{2-}), which is known to be the most stable plasma species generated by the excited molecular oxygen in the plasma. Nagasawa et al. [183] reported that an increased density of this absorbed oxygen species on the surface is correlated to the existence of O_2^{2-} ions at Sn^{2+} sites, which is responsible for a reduction of O^{2-} (or the generation of Sn^{2+} -O), as mentioned above.

In addition, the sample with a preheat treatment at 500°C before the plasma process was also tested in the same way as nonpreheated samples for comparison. As a result, there is no big difference between parts a and b of Figure 8.7, confirming that 500°C is not hot enough for sufficient thermal agitation to deteriorate the ZnO bond strength and to produce the hollow interiors. On the other hand, the reduction of the O^{2-} intensity (Zn-O bonds) in Figure 8.7d as compared to Figure 8.7b is again dominated by plasma treatment, showing behavior similar to that of nonpreheated samples. Moreover, the relative intensity ratios of O^{2-}/OH^- (2.63) and O_2^{2-}/OH^- (1.28) in Figure 8.7d are slightly lower than those in Figure 8.7c (3.16 and 1.62, respectively) because of an increase of the OH^- density. This suggests that, although preheating

can induce the activation energy of the oxygen-plasma effect to accelerate the surface diffusion of oxygen vacancies and cause somewhat of a change to the relative intensity, as compared to plasma treatment, it represents a minor effect on the etching mechanism.

Considering that the radical species can be produced via the reaction $O_2 + e^- \xrightarrow{\text{ionization}} O_2^+ + 2e^- \xrightarrow{\text{radical formation}} 2O + e^-$ during the plasma process, high energy or heat can be generated at the surface because of ion collisions. Thus, the influx of $\bullet O^{2-}$ or $\bullet OH$ radicals can disintegrate the ZnO core to form Zn-rich regions, and the chemical reaction could even be enhanced with the released oxygen ions (O^- and O^{2-}) from the FTO layer when the oxygen molecules are absorbed on its surface, as illustrated in Scheme 8.1. As a result, a nonequilibrium pressure-induced stress (σ) across the interface is caused by Zn generation. Furthermore, because the melting point of Zn metal is low (about 420°C), a higher Zn concentration can form and gasify inside the core, in which the stress was developed during the continuous reaction. The subsequent relaxation of the stress, accompanied by a decrease of energy in the core, could occur, so that the surface diffusion of metal cations (Zn) flowed outward to reach an equilibrium state and, therefore, excessive voids (hollow area) were left inside the core, whereas unconsumed ZnO NPs may be embedded near the FTO shell [91, 184].



Scheme 8.1 Top-View Cross-Sectional Schematic Diagram of an FTO-Coated ZnO Core-Shell Nanostructure, Illustrating the Oxygen-Plasma Enhanced Etching Evolution of the ZnO-FTO Nanotube^a (^a The direction of outward diffusion is indicated by the arrow in stage 3).

8.4 Photoresponse of ZnO-FTO composite nanotubes

To further illustrate the correlation between the optical and electrical properties and the etching mechanism, the sequential reduction of I_{NBE} corresponding to the PL spectra in Figure 8.6b was again examined in terms of photoresponse as a function of time (Figure 8.8). It is known that the spectral response in ZnO NRs indeed has a cutoff wavelength of ~ 375 nm, whereas FTO cannot be induced to fluoresce by the long-wavelength UV light source, as was expected from its wide band gap ($E_g = 3.6$ eV). Thus, under UV illumination ($\lambda = 365$ nm) in ambient air, the ZnO-FTO samples that were plasma-etched for 20 min exhibited nonunity photoresponse exponentials. This confirms that the discontinuous surface of the etched ZnO core may influence the photon-trapping electron-transfer effects.

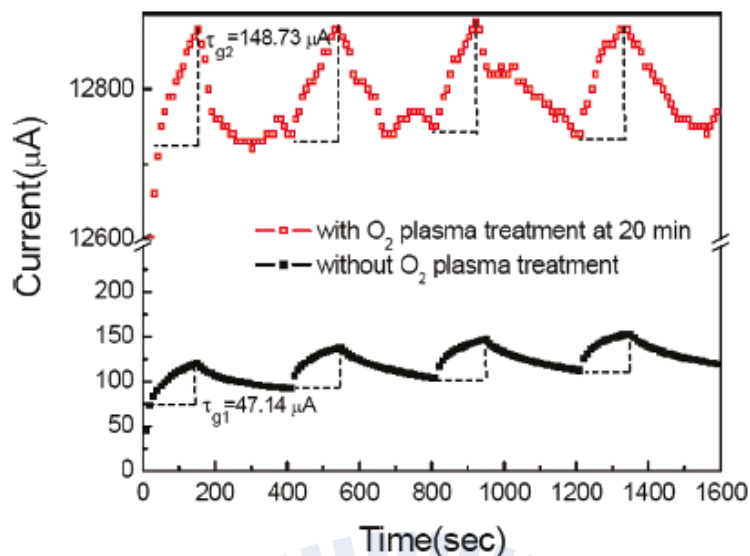


Figure 8.8 Under UV illumination ($\lambda=365\text{nm}$), with an applied voltage of +5 eV (electron conduction), τ_{g1} and τ_{g2} are shown indicating the response times of time-dependent photocurrent with (20 min) and without oxygen-plasma treatment, respectively.

Despite the above discussion, the present results demonstrate that the ZnO-FTO etched for 20 min displayed an enhancement in sensitivity of about 3 times of magnitude ($\tau_{g2} > \tau_{g1}$) and a remarkably increased dark current, from 4.539×10^{-5} to 1.234×10^{-2} A, compared to the unetched sample. On the basis of this result, it was concluded that (1) the accumulation of ZnO NPs embedded in the FTO layer still allows for excellent photon-absorbing properties and serves as a rectifying interfacial ZnO-FTO heterojunction, which can improve the separation of the electron-hole pairs and photosensitivity through discharge of the absorbed oxygen ions [$\text{h}^+ + \text{O}_2^-(\text{ad}) \rightarrow \text{O}_2(\text{g})$], (2) the oxygen plasma can introduce a high OH^- concentration, resulting in not only an increased carrier concentration but also the negative charge of two extra electrons released from the dangling Sn^{2+} -O bonds, which can act as a donor in the Sn^{4+} matrix, creating surface charges in the host lattice of ZnO and FTO [185], and (3) eventually the elimination of the resistive ZnO core after etching may regulate charge transport in the FTO conductive layer. Therefore, we

believe that this novel structural characteristic, with an enlarged interfacial area, will offer the major advantage of using 3D ZnO-FTO tubelike electrodes for nanoarchitectural optoelectronic devices.

8.5 Summary

In summary, we fabricated ZnO-FTO heterostructure nanotube arrays using presynthesized ZnO NR arrays as templates and deposited FTO NPs. After undergoing a dry-oxygen plasma treatment, the formation of voids in the ZnO core was initially observed alongside the ZnO-FTO interface at 2 min, and an increased etching time created a hollow along the [0001] plane in the ZnO inner core. The XPS study indicates that degradation of the O^{2-} peak intensity (531.32 eV) can be induced by the reactive $\bullet O^{2-}$ and $\bullet OH$ radicals and O-ion bombardment, which corresponds to dissociation of the Zn-O bonds and the outward diffusion of Zn cations, resulting in the occurrence of the hollow interior. In addition, the time dependence of the photocurrent (I-T) under UV illumination ($\lambda=365$ nm) shows a rectified photoresponse characteristic for the 20-min etched sample, and the dark current of this sample increases from 4.539×10^{-5} to 1.234×10^{-2} A (~ 3 orders of magnitude) compared to that of the unetched sample. This study demonstrates that a new architectural design with a large surface area can be further developed into a highly conductive 3D electrode with rectified photocatalytic activity for photovoltaic solar cells.

Chapter 9

Conclusion

9.1 Investigation of TCO thin film electrode for photovoltaic devices

In this thesis, firstly, FTO film electrodes were fabricated by ultrasonic spray pyrolysis deposition on glass substrate at 400°C, using O₂/N₂ deposition concentrations at 0, 20, 50, 80 and 100%. The structural, electrical and optical properties of the FTO texture films were studied as an effect of surface morphology (grain growth); a significant reduction in grain size was found to depend strongly on the increased oxygen concentration resulting in higher resistivity (ρ) and transmittance (T%). For the photovoltaic performance, the FTO film-based DSSCs with 0% O₂ showed higher conversion efficiency (4.22%) compared with 100% O₂ (3.12%). In contrast, the polymer solar cells, based on PEDOT:PSS layer spin-casted on the FTO electrode, improved the interfacial contacts between grain boundaries. The results showed the opposite trend that the efficiency of 100% O₂ sample was much more enhanced (3.13%) than that of 0% O₂ (1.85%).

Furthermore, as the components of hydrogenated amorphous silicon (a-Si:H) solar cells, two types of films (single FTO film and double AZO/FTO film) were investigated for use as a new TCO electrode layer. As expected, the surface of bare FTO films can be deteriorated due to a reduction of SnO₂ to metallic Sn and sub-oxide of SnO by H-incorporated ions and radicals under an exposure of the H-plasma treatment. On the other hand, the AZO overlayer was found to conserve the structural, electrical, and optical properties of the FTO beneath film. In particular, the TEM images reveals that H ions and radicals from the plasma, at a long treatment

of 30 min, could not significantly change lattice structure at the interface, indicating an effective AZO protecting layer. Finally, the post-heat treatment (400°C) would make recovery of the degraded FTO films.

9.2 Plasma treated metal oxide thin films and nanostructures

In this part, we demonstrate that “nitrogen plasma-assisted co-doped p-type (In, N):SnO₂” can be fabricated by using a simple spray pyrolysis method with 3% and 7% In doping concentrations, followed by thermal annealing (600°C) and post-N-plasma treatment. On the other hand, excess doping concentrations (15% and 30%) can lead to the formation of a secondary compound, such as n-type In₂O₃, resulting in a dramatic reduction of the sheet resistance compared to as-deposited SnO₂ film. In addition, when the p-type (N,In)-codoped SnO₂ layer was deposited on the n-type ZnO nanorod arrays, the I-V measurement demonstrated a symmetrical curve with rectified diode behavior at depleting regions between the n- and p-layer.

Secondly, a chemically based approach combining plasma treatment was used to develop ZnO nanotube (NT) and nanowire (NW) structures. The PL results show that a longer nitrogen plasma exposure can significantly improve the UV emission of ZnO nanotubes. The current–voltage characteristics (I-V) show that the photocurrent (4.82×10^{-7} A) of NTs can be remarkably enhanced compared to that (0.571×10^{-7} A) of ZnO NWs after exposure to N₂ plasma for 900 s. This treatment also enhances the photoresponse behavior of the plasma-treated NTs (by a factor of 20 over that of NWs).

Finally, such ZnO nanostructures are expected to deteriorate after undergoing a dry-oxygen plasma treatment with some certain parameters and conditions. Herein, we fabricated ZnO-FTO heterostructure nanotube arrays using presynthesized ZnO NR arrays as templates and deposited FTO outer layer. Increasing plasma treatment time (up to 20 min) can enhance the etching mechanism, so that the formation of hollow structure was observed along the [0001] plane in the ZnO inner core. The XPS analysis reveals that the reactive $\bullet\text{O}^{2-}$ and $\bullet\text{OH}$ radicals and O-ion bombardment strongly induce a dissociation of the Zn-O bonds and the outward diffusion of Zn cations. Finally, the time dependence of the photocurrent (I-T) under UV illumination ($\lambda=365$ nm) shows a rectified photoresponse characteristic for the 20-min etched sample, and the dark current of this sample increases ~ 3 orders of magnitude compared to that of the unetched sample.

Overall, these investigations can demonstrate that nano-architectural structures with a large surface area of metal oxide-based materials can be further developed into a highly conductive 3D electrode for photovoltaic solar cells by using simple fabrication methods.

References

- [1] C. A. Hoel, T. O. Mason, J. F. Gaillard, K. R. Poeppelmeier, *Chemistry of Materials* **2010**, *22*, 3569.
- [2] T. O. Mason, G. B. Gonzalez, D. R. Kammler, N. Mansourian-Hadavi, B. J. Ingram, *Thin Solid Films* **2002**, *411*, 106.
- [3] H. Kim, G. Kushto, R. Auyeung, A. Piqué, *Applied Physics A: Materials Science & Processing* **2008**, *93*, 521.
- [4] W. Wang, S. Wu, K. Reinhardt, Y. Lu, S. Chen, *Nano Letters* **2010**, *10*, 2012.
- [5] S. D. Rupesh, G. Shun-Yu, H. Wei-Der, L. Jin-Han, M. Yuan-Ron, S. P. Pramod, L. Yung, *Applied Physics Letters* **2011**, *98*, 133117.
- [6] J. Huh, J. Park, G. T. Kim, J. Y. Park, *Nanotechnology* **2011**, *22*, 085502.
- [7] T. Lim, S. Lee, M. Meyyappan, S. Ju, *ACS Nano* **2011**, *5*, 3917.
- [8] M. Kevin, W. L. Ong, G. H. Lee, G. W. Ho, *Nanotechnology* **2011**, *22*, 235701.
- [9] T. Ikuno, T. Yasuda, S. I. Honda, K. Oura, M. Katayama, J. G. Lee, H. Mori, *Journal of Applied Physics* **2005**, *98*, 114305.
- [10] S. W. Choi, J. Y. Park, S. S. Kim, *Nanotechnology* **2009**, *20*, 465603.
- [11] K. Shankar, J. I. Basham, N. K. Allam, O. K. Varghese, G. K. Mor, X. Feng, M. Paulose, J. A. Seabold, K. S. Choi, C. A. Grimes, *The Journal of Physical Chemistry C* **2009**, *113*, 6327.
- [12] K. Yang, G. W. She, H. Wang, X. M. Ou, X. H. Zhang, C. S. Lee, S. T. Lee, *The Journal of Physical Chemistry C* **2009**, *113*, 20169.
- [13] M. W. Ahn, K. S. Park, J. H. Heo, J. G. Park, D. W. Kim, K. J. Choi, J. H. Lee, S. H. Hong, *Applied Physics Letters* **2008**, *93*, 263103.
- [14] W. Cun, Z. Jincal, W. Xinming, M. Bixian, S. Guoying, P. Pingán, F. Jiamo, *Applied Catalysis B: Environmental* **2002**, *39*, 269.
- [15] Q. Zhao, X. Y. Xu, X. F. Song, X. Z. Zhang, D. P. Yu, C. P. Li, L. Guo, *Applied Physics Letters* **2006**, *88*, 033102.
- [16] M. Law, L. E. Greene, J. C. Johnson, R. Saykally, P. Yang, *Nature Materials* **2005**, *4*, 455.

- [17] T. Zhai, X. Fang, M. Liao, X. Xu, H. Zeng, B. Yoshio, D. Golberg, *Sensors* **2009**, *9*, 6504.
- [18] Y. Sun, D. J. Riley, M. N. R. Ashfold, *The Journal of Physical Chemistry B* **2006**, *110*, 15186.
- [19] L. E. Greene, M. Law, J. Goldberger, F. Kim, J. C. Johnson, Y. Zhang, R. J. Saykally, P. Yang, *Angewandte Chemie International Edition* **2003**, *42*, 3031.
- [20] C. J. Park, D.-K. Choi, J. Yoo, G.-C. Yi, C. J. Lee, *Applied Physics Letters* **2007**, *90*, 083107.
- [21] C. E. Secu, M. Sima, *Optical Materials* **2009**, *31*, 876.
- [22] J. Q. Hu, Y. Bando, *Applied Physics Letters* **2003**, *82*, 1401.
- [23] N. Chantarat, Y. W. Chen, S. Y. Chen, C. C. Lin, *Nanotechnology* **2009**, *20*, 395201.
- [24] M. Roozbehi, P. Sangpour, A. Khademi, A. Z. Moshfegh, *Applied Surface Science* **2011**, *257*, 3291.
- [25] G. Adamopoulos, A. Bashir, S. Thomas, W. P. Gillin, S. Georgakopoulos, M. Shkunov, M. A. Baklar, N. Stingelin, R. C. Maher, L. F. Cohen, D. D. C. Bradley, T. D. Anthopoulos, *Advanced Materials* **2010**, *22*, 4764.
- [26] U. Ozgur, I. A. Ya, C. Liu, A. Teke, M. A. Reshchikov, S. Dogan, V. Avrutin, S. J. Cho, H. Morkoc, *Journal of Applied Physics* **2005**, *98*, 041301.
- [27] A. Seko, A. Togo, F. Oba, I. Tanaka, *Physical Review Letters* **2008**, *100*, 045702.
- [28] L. V. Thong, N. D. Hoa, D. T. T. Le, D. T. Viet, P. D. Tam, A. T. Le, N. V. Hieu, *Sensors and Actuators B: Chemical* **2010**, *146*, 361.
- [29] S. S. Pan, C. Ye, X. M. Teng, L. Li, G. H. Li, *Applied Physics Letters* **2006**, *89*, 251911.
- [30] Y. H. Liao, N. F. Scherer, K. Rhodes, *Journal of Physical Chemistry B* **2001**, *105*, 3282.
- [31] K. H. Choi, J. A. Jeong, J. W. Kang, D. G. Kim, J. K. Kim, S. I. Na, D. Y. Kim, S. S. Kim, H. K. Kim, *Solar Energy Materials and Solar Cells* **2009**, *93*, 1248.
- [32] E. Joanni, R. Savu, M. de Sousa Góes, P. R. Bueno, J. N. de Freitas, A. F. Nogueira, E. Longo, J. A. Varela, *Scripta Materialia* **2007**, *57*, 277.
- [33] Y. E. Chang, D. Y. Youn, G. Ankonina, D. J. Yang, H. G. Kim, A. Rothschild, I. D. Kim, *Chemical Communications* **2009**, 4019-4021.
- [34] B. Liu, H. C. Zeng, *The Journal of Physical Chemistry B* **2004**, *108*, 5867.
- [35] A. Walsh, J. L. F. Da Silva, S. H. Wei, *Physical Review B* **2008**, *78*, 075211.

- [36] J. H. Hwang, D. D. Edwards, D. R. Kammler, T. O. Mason, *Solid State Ionics* **2000**, *129*, 135.
- [37] J. B. Varley, A. Janotti, C. G. Van de Walle, *Physical Review B* **2010**, *81*, 245216.
- [38] X. Sun, R. Long, X. Cheng, X. Zhao, Y. Dai, B. Huang, *The Journal of Physical Chemistry C* **2008**, *112*, 9861.
- [39] E. Nogales, J. A. García, B. Méndez, J. Piqueras, K. Lorenz, E. Alves, *Journal of Physics D: Applied Physics* **2008**, *41*, 065406.
- [40] Z. Fan, X. Wen, S. Yang, J. G. Lu, *Applied Physics Letters* **2005**, *87*, 013113.
- [41] W. Li, A. I. Frenkel, J. C. Woicik, C. Ni, S. I. Shah, *Physical Review B* **2005**, *72*, 155315.
- [42] D. O. Scanlon, A. Walsh, B. J. Morgan, M. Nolan, J. Fearon, G. W. Watson, *The Journal of Physical Chemistry C* **2007**, *111*, 7971.
- [43] R. S. Yu, S. C. Liang, C. J. Lu, D. C. Tasi, F. S. Shieu, *Applied Physics Letters* **2007**, *90*, 191117.
- [44] H. Ohta, M. Orita, M. Hirano, H. Hosono, *Journal of Applied Physics* **2001**, *89*, 5720.
- [45] S. H. Lee, T. S. Lee, K. S. Lee, B. Cheong, Y. D. Kim, W. M. Kim, *Journal of Physics D: Applied Physics* **2008**, *41*, 095303.
- [46] Q. Li, J. K. Shang, *Environmental Science & Technology* **2010**, *44*, 3493.
- [47] A. Walsh, J. L. F. Da Silva, S.-H. Wei, ouml, C. rber, A. Klein, L. F. J. Piper, A. DeMasi, K. E. Smith, G. Panaccione, P. Torelli, D. J. Payne, A. Bourlange, R. G. Egdell, *Physical Review Letters* **2008**, *100*, 167402.
- [48] J. H. Werner, H. H. Guttler, *Journal of Applied Physics* **1991**, *69*, 1522.
- [49] S. Lee, J. H. Noh, S. T. Bae, I. S. Cho, J. Y. Kim, H. Shin, J. K. Lee, H. S. Jung, K. S. Hong, *The Journal of Physical Chemistry C* **2009**, *113*, 7443.
- [50] J. Kim, J. Kim, M. Lee, *Nanotechnology* **2010**, *21*, 345203.
- [51] T. Aoki, Y. Hatanaka, D. C. Look, *Applied Physics Letters* **2000**, *76*, 3257.
- [52] R. L. Hoffman, J. F. Wager, M. K. Jayaraj, J. Tate, *Journal of Applied Physics* **2001**, *90*, 5763.
- [53] A. N. Banerjee, S. Nandy, C. K. Ghosh, K. K. Chattopadhyay, *Thin Solid Films* **2007**, *515*, 7324.
- [54] X. W. Sun, J. X. Wang, *Nano Letters* **2008**, *8*, 1884.

- [55] C. Soci, A. Zhang, B. Xiang, S. A. Dayeh, D. P. R. Aplin, J. Park, X. Y. Bao, Y. H. Lo, D. Wang, *Nano Letters* **2007**, *7*, 1003.
- [56] S. Song, W. K. Hong, S. S. Kwon, T. Lee, *Applied Physics Letters* **2008**, *92*, 263109.
- [57] S. E. Ahn, H. J. Ji, K. Kim, G. T. Kim, C. H. Bae, S. M. Park, Y. K. Kim, J. S. Ha, *Applied Physics Letters* **2007**, *90*, 153106.
- [58] R. Ghosh, M. Dutta, D. Basak, *Applied Physics Letters* **2007**, *91*, 073108.
- [59] R. Fan, Y. Wu, D. Li, M. Yue, A. Majumdar, P. Yang, *Journal of the American Chemical Society* **2003**, *125*, 5254.
- [60] H. G. Moon, Y. S. Shim, D. Su, H. H. Park, S. J. Yoon, H. W. Jang, *The Journal of Physical Chemistry C* **2011**, *115*, 9993.
- [61] L. Zheng, Y. Zheng, C. Chen, Y. Zhan, X. Lin, Q. Zheng, K. Wei, J. Zhu, *Inorganic Chemistry* **2009**, *48*, 1819.
- [62] Q. Kuang, Z. Y. Jiang, Z. X. Xie, S. C. Lin, Z. W. Lin, S. Y. Xie, R. B. Huang, L. S. Zheng, *Journal of the American Chemical Society* **2005**, *127*, 11777.
- [63] M. S. Gudiksen, L. J. Lauhon, J. Wang, D. C. Smith, C. M. Lieber, *Nature* **2002**, *415*, 617.
- [64] R. Solanki, J. Huo, J. L. Freeouf, B. Miner, *Applied Physics Letters* **2002**, *81*, 3864.
- [65] S. Han, C. Li, Z. Liu, B. Lei, D. Zhang, W. Jin, X. Liu, T. Tang, C. Zhou, *Nano Letters* **2004**, *4*, 1241.
- [66] L. J. Lauhon, M. S. Gudiksen, D. Wang, C. M. Lieber, *Nature* **2002**, *420*, 57.
- [67] L. Manna, E. C. Scher, L. S. Li, A. P. Alivisatos, *Journal of the American Chemical Society* **2002**, *124*, 7136.
- [68] Y. J. Hsu, S. Y. Lu, *Chemical Communications* **2004**, 2102-2103.
- [69] Z. Wang, X. Liu, J. Gong, H. Huang, S. Gu, S. Yang, *Crystal Growth & Design* **2008**, *8*, 3911.
- [70] J. Zhan, Y. Bando, J. Hu, T. Sekiguchi, D. Golberg, *Advanced Materials* **2005**, *17*, 225.
- [71] B. K. Teo, C. P. Li, X. H. Sun, N. B. Wong, S. T. Lee, *Inorganic Chemistry* **2003**, *42*, 6723.
- [72] R. D. Sun, A. Nakajima, A. Fujishima, T. Watanabe, K. Hashimoto, *The Journal of Physical Chemistry B* **2001**, *105*, 1984.

- [73] B. Angadi, H. C. Park, H. W. Choi, J. W. Choi, W. K. Choi, *Journal of Physics D: Applied Physics* **2007**, *40*, 1422.
- [74] B. J. Coppa, C. C. Fulton, S. M. Kiesel, R. F. Davis, C. Pandarinath, J. E. Burnette, R. J. Nemanich, D. J. Smith, *Journal of Applied Physics* **2005**, *97*, 103517.
- [75] T. Nagata, O. Bierwagen, M. E. White, M. Y. Tsai, J. S. Speck, *Journal of Applied Physics* **2010**, *107*, 033707.
- [76] Y. Nagasawa, T. Choso, T. Karasuda, S. Shimomura, F. Ouyang, K. Tabata, Y. Yamaguchi, *Surface Science* **1999**, *226*, 433-435.
- [77] S. Luo, P. K. Chu, Z. Di, M. Zhang, W. Liu, C. Lin, J. Fan, X. Wu, *Applied Physics Letters* **2006**, *88*, 013109.
- [78] Kili, ccedil, Ccedil, etin, A. Zunger, *Physical Review Letters* **2002**, *88*, 095501.
- [79] P. Meduri, C. Pendyala, V. Kumar, G. U. Sumanasekera, M. K. Sunkara, *Nano Letters* **2009**, *9*, 612.
- [80] J. A. Czaban, D. A. Thompson, R. R. LaPierre, *Nano Letters* **2008**, *9*, 148.
- [81] V. Kumar, J. H. Kim, J. B. Jasinski, E. L. Clark, M. K. Sunkara, *Crystal Growth & Design* **2011**, *11*, 2913-2919.
- [82] L. Taekyung, L. Sumi, S. Misook, J. Sanghyun, *Electrochemical and Solid-State Letters* **2011**, *14*, H218-H221.
- [83] S. S. Pan, G. H. Li, L. B. Wang, Y. D. Shen, Y. Wang, T. Mei, X. Hu, *Applied Physics Letters* **2009**, *95*, 222112.
- [84] I. n. Robel, V. Subramanian, M. Kuno, P. V. Kamat, *Journal of the American Chemical Society* **2006**, *128*, 2385.
- [85] E. Hao, B. Yang, J. Zhang, X. Zhang, J. Sun, J. Shen, *Journal of Materials Chemistry* **1998**, *8*, 1327.
- [86] Z. Yang, C.-Y. Chen, C.-W. Liu, H.-T. Chang, *Chemical Communications*, *46*, 5485.
- [87] A. Zaban, O. I. Micić, B. A. Gregg, A. J. Nozik, *Langmuir* **1998**, *14*, 3153-3156.
- [88] K. S. Leschkies, R. Divakar, J. Basu, E. Enache-Pommer, J. E. Boercker, C. B. Carter, U. R. Kortshagen, D. J. Norris, E. S. Aydil, *Nano Letters* **2007**, *7*, 1793.
- [89] C. Xiang, S.-C. Kung, D. K. Taggart, F. Yang, M. A. Thompson, A. G. Güñell, Y. Yang, R. M. Penner, *ACS Nano* **2008**, *2*, 1939.

- [90] D.-G. Choi, H. K. Yu, S. G. Jang, S.-M. Yang, *Journal of the American Chemical Society* **2004**, *126*, 7019.
- [91] H. J. Fan, M. Knez, R. Scholz, D. Hesse, K. Nielsch, M. Zacharias, U. GÄsele, *Nano Letters* **2007**, *7*, 993.
- [92] H. Zeng, W. Cai, P. Liu, X. Xu, H. Zhou, C. Klingshirn, H. Kalt, *ACS Nano* **2008**, *2*, 1661.
- [93] J. Wallinga, W. M. Arnoldbik, A. M. Vredenberg, R. E. I. Schropp, W. F. van der Weg, *The Journal of Physical Chemistry B* **1998**, *102*, 6219.
- [94] T. Hayashi, K. Kawabata, K. Yamada, S. Miyazaki, M. Hirose, *Japanese Journal of Applied Physics* **1991**, *30*, 675.
- [95] A. B. F. Martinson, J. W. Elam, J. Liu, M. J. Pellin, T. J. Marks, J. T. Hupp, *Nano Letters* **2008**, *8*, 2862.
- [96] M. GrÄtzel, *Inorganic Chemistry* **2005**, *44*, 6841.
- [97] M. S. Sander, M. J. Côté, W. Gu, B. M. Kile, C. P. Tripp, *Advanced Materials* **2004**, *16*, 2052.
- [98] S. H. Kang, S. H. Choi, M. S. Kang, J. Y. Kim, H. S. Kim, T. Hyeon, Y. E. Sung, *Advanced Materials* **2008**, *20*, 54.
- [99] H. W. Wang, C. F. Ting, M. K. Hung, C. H. Chiou, Y. L. Liu, Z. Liu, K. R. Ratinac, S. P. Ringer, *Nanotechnology* **2009**, *20*, 055601.
- [100] Z. Yang, T. Xu, Y. Ito, U. Welp, W. K. Kwok, *The Journal of Physical Chemistry C* **2009**, *113*, 20521.
- [101] J. H. Noh, S. Lee, J. Y. Kim, J. K. Lee, H. S. Han, C. M. Cho, I. S. Cho, H. S. Jung, K. S. Hong, *The Journal of Physical Chemistry C* **2008**, *113*, 1083.
- [102] T. Kawashima, T. Ezure, K. Okada, H. Matsui, K. Goto, N. Tanabe, *Journal of Photochemistry and Photobiology A: Chemistry* **2004**, *164*, 199.
- [103] Q. Zhang, G. Cao, *Nano Today* **2011**, *6*, 91-109.
- [104] C. H. Ku, J. J. Wu, *Nanotechnology* **2007**, *18*, 505706.
- [105] I. Volintiru, M. Creatore, B. J. Kniknie, C. I. M. A. Spee, M. C. M. Van De Sanden, *Journal of Applied Physics* **2007**, *102*, 043709.
- [106] S. Lee, J. H. Noh, H. S. Han, D. K. Yim, D. H. Kim, J.-K. Lee, J. Y. Kim, H. S. Jung, K. S. Hong, *The Journal of Physical Chemistry C* **2009**, *113*, 6878.

- [107] J. H. Lee, C. Y. Chou, Z. X. Bi, C. F. Tsai, H. Wang, *Nanotechnology* **2009**, *20*, 395704.
- [108] C. Y. Kim, D. H. Riu, *Thin Solid Films* **2011**, *519*, 3081.
- [109] R. Y. Korotkov, P. Ricou, A. J. E. Farran, *Thin Solid Films* **2006**, *502*, 79.
- [110] J. Kane, H. P. Schweizer, *Journal of the Electrochemical Society* **1976**, *123*, 270.
- [111] T. N. Blanton, M. Lelental, *Materials Research Bulletin* **1994**, *29*, 537.
- [112] K. Y. Rajpure, M. N. Kusumade, M. N. Neumann-Spallart, C. H. Bhosale, *Materials Chemistry and Physics* **2000**, *64*, 184.
- [113] J. W. Bae, S. W. Lee, G. Y. Yeom, *Journal of the Electrochemical Society* **2007**, *154*, D34.
- [114] K. Omura, P. Veluchamy, M. Tsuji, T. Nishio, M. Murozono, *Journal of the Electrochemical Society* **1999**, *146*, 2113.
- [115] M. Dashtdar, M. T. Tavassoly, *J. Opt. Soc. Am. A* **2008**, *25*, 2509.
- [116] H. Fouckhardt, I. Steingoetter, M. Brinkmann, M. Hagemann, H. Zarschizky, L. Zschiedrich, *Advances in OptoElectronics* **2007**, *2007*, 1.
- [117] H. Stiebig, F. Siebke, W. Beyer, C. Beneking, B. Rech, H. Wagner, *Solar Energy Materials and Solar Cells* **1997**, *48*, 351.
- [118] S. Major, M. C. Bhatnagar, S. Kumar, K. L. Chopra, *Journal of Vacuum Science & Technology A: Vacuum, Surfaces, and Films* **1988**, *6*, 2415.
- [119] K. Xiong, J. Robertson, S. J. Clark, *Journal of Applied Physics* **2007**, *102*, 083710.
- [120] K. Ahn, Y. S. Jeong, H. U. Lee, S. Y. Jeong, H. S. Ahn, H. S. Kim, S. G. Yoon, C. R. Cho, *Thin Solid Films* **2010**, *518*, 4066.
- [121] C. H. Lee, K. S. Lim, J. Song, *Japanese Journal of Applied Physics* **1997**, *36*, 4418.
- [122] C. G. Van de Walle, *Physical Review Letters* **2000**, *85*, 1012.
- [123] J. Bang, K. J. Chang, *Applied Physics Letters* **2008**, *92*, 132109.
- [124] H. Kim, C. M. Gilmore, A. Pique', J. S. Horwitz, H. Mattoussi, H. Murata, Z. H. Kafafi, D. B. Chrisey, *Journal of Applied Physics* **1999**, *86*, 6451.
- [125] A. I. Martínez, L. Huerta, J. M. O. R. d. León, D. Acosta, O. Malik, M. Aguilar, *Journal of Physics D: Applied Physics* **2006**, *39*, 5091.
- [126] J. Suffner, P. Ágoston, J. Kling, H. Hahn, *Journal of Nanoparticle Research* **2010**, *12*, 2579.
- [127] J. C. Liu, A. D. Marwick, F. K. LeGoues, *Physical Review B* **1991**, *44*, 1861.

- [128] H. W. Wang, C. F. Ting, M. K. Hung, C. H. Chiou, Y. L. Liu, Z. Y. Liu, K. R. Ratinac, S. P. Ringer, *Nanotechnology* **2009**, *20*, 055601.
- [129] Q. Kuang, C. S. Lao, Z. Li, Y. Z. Liu, Z. X. Xie, L. S. Zheng, Z. L. Wang, *The Journal of Physical Chemistry C* **2008**, *112*, 11539.
- [130] H. Ohta, M. Orita, M. Hirano, H. Hosono, *Journal of Applied Physics* **2001**, *89*, 5720.
- [131] M. T. Chen, M. P. Lu, Y. J. Wu, J. Song, C. Y. Lee, M. Y. Lu, Y. C. Chang, L. J. Chou, Z. L. Wang, L. J. Chen, *Nano Letters* **2010**, *10*, 4387.
- [132] C. Drake, S. Seal, *Applied Physics Letters* **2007**, *90*, 233117.
- [133] R. Kudrawiec, T. Suski, J. Serafinczuk, J. Misiewicz, D. Muto, Y. Nanishi, *Applied Physics Letters* **2008**, *93*, 131917.
- [134] J. L. Liu, F. X. Xiu, L. J. Mandalapu, Z. Yang, *Proc. SPIE* **2006**, *6122*, 61220H.
- [135] T. Yamamoto, H. Katayama-Yoshida, *Physica B: Condensed Matter* **1999**, *273-274*, 113.
- [136] R. E. Jones, K. M. Yu, S. X. Li, W. Walukiewicz, J. W. Ager, E. E. Haller, H. Lu, W. J. Schaff, *Physical Review Letters* **2006**, *96*, 125505.
- [137] Y. Q. Bie, Z. M. Liao, P. W. Wang, Y. B. Zhou, X. B. Han, Y. Ye, Q. Zhao, X. S. Wu, L. Dai, J. Xu, L. W. Sang, J. J. Deng, K. Laurent, Y. Leprince-Wang, D. P. Yu, *Advanced Materials* **2010**, *22*, 4284.
- [138] A. K. Singh, A. Janotti, M. Scheffler, C. G. Van de Walle, *Physical Review Letters* **2008**, *101*, 055502.
- [139] G. Qin, D. Li, Z. Feng, S. Liu, *Thin Solid Films* **2009**, *517*, 3345.
- [140] B. M. Mohammad-Mehdi, S. S. Mehrdad, *Semiconductor Science and Technology* **2004**, *19*, 764.
- [141] C. H. Lee, B. A. Nam, W. K. Choi, J. K. Lee, D. J. Choi, Y. J. Oh, *Materials Letters* **2011**, *65*, 722.
- [142] M. Himmerlich, M. Koufaki, G. Ecke, C. Mauder, V. Cimalla, J. A. Schaefer, A. Kondilis, N. T. Pelekanos, M. Modreanu, S. Krischok, E. Aperathitis, *ACS Applied Materials & Interfaces* **2009**, *1*, 1451.
- [143] E. Aperathitis, M. Bender, V. Cimalla, G. Ecke, M. Modreanu, *Journal of Applied Physics* **2003**, *94*, 1258.
- [144] R. S. Yu, S. C. Liang, C. J. Lu, D. C. Tasi, F. S. Shieu, *Applied Physics Letters* **2007**, *90*, 191117.

- [145] P. Ágoston, C. Körber, A. Klein, M. J. Puska, R. M. Nieminen, K. Albe, *Journal of Applied Physics* **2010**, *108*, 053511.
- [146] C. Lao, Y. Li, C. P. Wong, Z. L. Wang, *Nano Letters* **2007**, *7*, 1323.
- [147] C. L. Hsu, S. J. Chang, Y. R. Lin, P. C. Li, T. S. Lin, S. Y. Tsai, T. H. Lu, I. C. Chen, *Chemical Physics Letters* **2005**, *416*, 75.
- [148] C. S. Hsiao, S. Y. Chen, W. L. Kuo, C. C. Lin, S. Y. Cheang, *Nanotechnology* **2008**, *19*, 405608.
- [149] K. Keem, J. Kang, D. Y. Jeong, B. Min, K. Cho, H. Kim, S. Kim, Y. K. Kim, *Japanese Journal of Applied Physics* **2007**, *46*, 4355.
- [150] G. D. Yuan, W. J. Zhang, J. S. Jie, X. Fan, J. A. Zapien, Y. H. Leung, L. B. Luo, P. F. Wang, C. S. Lee, S. T. Lee, *Nano Letters* **2008**, *8*, 2591.
- [151] S. Song, W. K. Hong, S. S. Kwon, T. Lee, *Applied Physics Letters* **2008**, *92*, 263109.
- [152] R. Ghosh, D. Basak, *Applied Physics Letters* **2007**, *90*, 243106.
- [153] K. Keem, H. Kim, G. T. Kim, J. S. Lee, B. Min, K. Cho, M. Y. Sung, S. Kim, *Applied Physics Letters* **2004**, *84*, 4376.
- [154] R. Ghosh, M. Dutta, D. Basak, *Applied Physics Letters* **2007**, *91*, 073108.
- [155] S. E. Ahn, H. J. Ji, K. Kim, G. T. Kim, C. H. Bae, S. M. Park, Y. K. Kim, J. S. Ha, *Applied Physics Letters* **2007**, *90*, 153106.
- [156] H. Q. Le, S. Tripathy, S. J. Chua, *Applied Physics Letters* **2008**, *92*, 141910.
- [157] C. C. Lin, S. Y. Chen, S. Y. Cheng, H. Y. Lee, *Applied Physics Letters* **2004**, *84*, 5040.
- [158] S. Mridha, D. Basak, *Journal of Physics D: Applied Physics* **2007**, *40*, 6902.
- [159] X. Shen, P. B. Allen, J. T. Muckerman, J. W. Davenport, J.-C. Zheng, *Nano Letters* **2007**, *7*, 2267.
- [160] C. Bae, H. Yoo, S. Kim, K. Lee, J. Kim, M. M. Sung, H. Shin, *Chemistry of Materials* **2008**, *20*, 756.
- [161] K. Raidongia, C. N. R. Rao, *The Journal of Physical Chemistry C* **2008**, *112*, 13366.
- [162] Y. Shi, D. Fu, D. H. Marsh, G. A. Rance, A. N. Khlobystov, L. J. Li, *The Journal of Physical Chemistry C* **2008**, *112*, 13004.
- [163] P. Brown, K. Takechi, P. V. Kamat, *The Journal of Physical Chemistry C* **2008**, *112*, 4776.

- [164] H. C. Liao, C. C. Lin, Y. W. Chen, T. C. Liu, S. Y. Chen, *Journal of Materials Chemistry* **2010**, *20*, 5429.
- [165] E. Joanni, R. Savu, M. de Sousa Góes, P. R. Bueno, J. N. de Freitas, A. F. Nogueira, E. Longo, J. A. Varela, *Scripta Materialia* **2007**, *57*, 277.
- [166] B. D. Yuhas, P. Yang, *Journal of the American Chemical Society* **2009**, *131*, 3756.
- [167] H. C. Zeng, *Journal of Materials Chemistry* **2006**, *16*, 649.
- [168] K. An, S. G. Kwon, M. Park, H. B. Na, S.-I. Baik, J. H. Yu, D. Kim, J. S. Son, Y. W. Kim, I. C. Song, W. K. Moon, H. M. Park, T. Hyeon, *Nano Letters* **2008**, *8*, 4252.
- [169] B. Liu, H. C. Zeng, *The Journal of Physical Chemistry B* **2004**, *108*, 5867.
- [170] B. Liu, H. C. Zeng, *Journal of the American Chemical Society* **2004**, *126*, 16744.
- [171] H. Zeng, Z. Li, W. Cai, B. Cao, P. Liu, S. Yang, *The Journal of Physical Chemistry B* **2007**, *111*, 14311.
- [172] Y. Yang, D. S. Kim, R. Scholz, M. Knez, S. M. Lee, U. Gnanse, M. Zacharias, *Chemistry of Materials* **2008**, *20*, 3487.
- [173] I. C. Yao, P. Lin, T. Y. Tseng, *Nanotechnology* **2009**, *20*, 125202.
- [174] Y. Chen, D. M. Bagnall, H. J. Koh, K. T. Park, K. Hiraga, Z. Zhu, T. Yao, *Journal of Applied Physics* **1998**, *84*, 3912.
- [175] C. A. Wolden, *Plasma Chemistry and Plasma Processing* **2005**, *25*, 169.
- [176] M. Liu, H. K. Kim, *Applied Physics Letters* **2004**, *84*, 173.
- [177] H. M. Cheng, K. F. Lin, H. C. Hsu, W. F. Hsieh, *Applied Physics Letters* **2006**, *88*, 261909.
- [178] Y. H. Yang, X. Y. Chen, Y. Feng, G. W. Yang, *Nano Letters* **2007**, *7*, 3879.
- [179] X. Y. Xue, Y. J. Chen, Y. G. Liu, S. L. Shi, Y. G. Wang, T. H. Wang, *Applied Physics Letters* **2006**, *88*, 201907.
- [180] Y. Zhang, A. Kolmakov, S. Chretien, H. Metiu, M. Moskovits, *Nano Letters* **2004**, *4*, 403.
- [181] K.-W. Kim, P.-S. Cho, S.-J. Kim, J.-H. Lee, C.-Y. Kang, J.-S. Kim, S.-J. Yoon, *Sensors and Actuators B: Chemical* **2007**, *123*, 318.
- [182] T. Nagata, O. Bierwagen, M. E. White, M. Y. Tsai, J. S. Speck, *Journal of Applied Physics* **2010**, *107*, 033707.

- [183] Y. Nagasawa, T. Choso, T. Karasuda, S. Shimomura, F. Ouyang, K. Tabata, Y. Yamaguchi, *Surface Science* **1999**, 226, 433.
- [184] V. P. Zhdanov, B. Kasemo, *Nano Letters* **2009**, 9, 2172.
- [185] B. Angadi, H. C. Park, H. W. Choi, J. W. Choi, W. K. Choi , *Journal of Physics D: Applied Physics* **2007**, 40, 1422.



Curriculum vitae

Name: Naratip Chantararat

26.09.1982 Born in Lampang (Thailand)

2000-2004 Undergraduate study in the department of physics at Chulalongkorn University (Thailand)

2004-2006 Graduate study in the department of materials science and nanotechnology at Linköping University (Sweden)

2007-2011 PhD study in the department of materials science and engineering at National Chiao Tung University (Taiwan)

Publication list

Journals

1. N Chantarat, Yu-Wei Chen, San-Yuan Chen and Chin-Ching Lin, “Enhanced UV photoresponse in nitrogen plasma ZnO nanotubes”, *Nanotechnology*, 2009, 20, 395201. (Impact Factor: 3.137)
2. N. Chantarat, Yu-Wei Chen, Chin-Ching Lin, Mei-Ching Chiang, and San-Yuan Chen, “Selective Oxygen-Plasma-Etching Technique for the Formation of ZnO-FTO Heterostructure Nanotubes and Their Rectified Photocatalytic Properties”, *Inorganic Chemistry*, 2010, 49, 11077-11083. (Impact Factor: 4.657)
3. Hung-Chou Liao, **Naratip Chantarat**, Cheng-Hsiung Peng, San-Yuan Chen, “Effect of Annealing and Aspect Ratio of In-situ Growing CdS Nanocrystals on Interfacial Properties and Photovoltaic Performance of P3HT/ CdS Nanocomposites”, accepted by *the Journal of The Electrochemical Society*, 2011 (Impact Factor: 2.4)

Manuscripts

1. N. Chantarat, C. C. Lin, M. C. Chiang, and S. Y. Chen, “Nitrogen Plasma-Assisted Co-doped P-type (In, N):SnO₂ Ultra-Fine Thin Films and N-ZnO/p-In:SnO₂ Core-Shell Heterojunction Diodes Fabricated by an Ultrasonic Spray Pyrolysis Method”, *submitted to The Journal of Physical Chemistry C*.

2. **N. Chantarat**, C. C. Lin, M. C. Chiang, S. H. Hsu, and S. Y. Chen, “The Role of a Double-Layered, Transparent Conducting Oxide Thin Film in Improving the Hydrogen Plasma Durability of Amorphous-Silicon Based Tandem Solar Cells”, *submitted to The Journal of Physical Chemistry C*.

Conference

Naratip Chantarat, Y. W. Chen, C. C. Lin, M. C. Chiang, S. Y. Chen, “Fabrication of FTO Nanotube by Using Oxygen Plasma Etching Technique on FTO-Coated ZnO Template”, *Poster presentation in MRS Spring Meeting*, San Francisco, California, U.S.A, April 25th - April 29th, 2011.